POLYPUBLIE

Towards an Optical Platform of Integrated Suspended Microresonators Made of Multiple Inkjet-Printed Polymers for Gas Sensing Applications

Marc-Antoine Bianki

Document en libre accès dans PolyPublie
Open Access document in PolyPublie

Date	2025
Type	Mémoire ou thèse / Dissertation or Thesis Thèse de doctorat/Ph.D. thesis
URL de PolyPublie PolyPublie URL	https://publications.polymtl.ca/62743/
Conditions d'utilisation Terms of use	© Tous droits réservés / All rights reserved
Référence Citation	Bianki, M.-A. (2025). Towards an Optical Platform of Integrated Suspended Microresonators Made of Multiple Inkjet-Printed Polymers for Gas Sensing Applications [Thèse de doctorat, Polytechnique Montréal]. PolyPublie. https://publications.polymtl.ca/62743/

Détails de la thèse
Thesis details

Directeurs de recherche Advisors	Yves-Alain Peter
Programme Program	Génie physique

Ce fichier a été téléchargé à partir de PolyPublie, le dépôt institutionnel de Polytechnique Montréal
This file has been downloaded from PolyPublie, the institutional repository of Polytechnique Montréal
https://publications.polymtl.ca

POLYTECHNIQUE MONTRÉAL
affiliée à l'Université de Montréal

Towards an optical platform of integrated suspended microresonators made of multiple inkjet-printed polymers for gas sensing applications

MARC-ANTOINE BIANKI
Département de génie physique

Thèse présentée en vue de l'obtention du diplôme de *Philosophiæ Doctor*
Génie physique

Février 2025

© Marc-Antoine Bianki, 2025.

POLYTECHNIQUE MONTRÉAL
affiliée à l'Université de Montréal

Cette thèse intitulée :

Towards an optical platform of integrated suspended microresonators made of multiple inkjet-printed polymers for gas sensing applications

présentée par **Marc-Antoine BIANKI**
en vue de l'obtention du diplôme de *Philosophiæ Doctor*
a été dûment acceptée par le jury d'examen constitué de :

Clara SANTATO, présidente
Yves-Alain PETER, membre et directeur de recherche
Daniel THERRIAULT, membre
Michaël **MÉNARD**, membre externe

DEDICATION

To my beloved wife, Roxanne-Alexandra,
whose love and patience,
made this adventure possible.

À ma femme que j'aime, Roxanne-Alexandra,
qui, par son amour et sa patience,
a rendu cette aventure possible.

ACKNOWLEDGEMENTS

This thesis would not have been possible without the support and guidance of many individuals. First and foremost, I would like to thank my supervisor, Prof. Yves-Alain Peter, for accepting me into his research group and mostly for his invaluable advice and insightful feedback throughout this research journey.

I would like to express my sincere gratitude to our laboratory technician, Yves Drolet, for his inestimable technical support throughout my PhD journey. His passion for sharing his technical knowledge will help me in my professional career. I am equally grateful to the entire Microfabrication Laboratory staff, including Marie-Hélène Bernier, Christophe Clément, André Hoang-Gaona, and Alexandre Perron, for their assistance and guidance with the microfabrication process. Their dedication to maintaining the clean room and supporting students' research is truly honorable. I benefited greatly from our discussions.

This work would not have been possible without the collaboration of the Optical Fiber Laboratory of Prof. Nicolas Godbout for the fabrication of tapered optical fibers. I would like to express my sincere gratitude to Rodrigo Becerra for his invaluable assistance with the fabrication setup and to Mikaël Leduc for his expert advice on various technical questions related to optics. Another crucial piece of equipment for this thesis was the inkjet printer from Microdrop. I am grateful to Ricardo Izquierdo for bringing this apparatus to my attention during my PhD oral exam. I would also like to thank Richard Martel for his trust and generosity in lending me this equipment without hesitation.

I am honored to have collaborated with the past and present members of the Microphotonic Laboratory. I would like to thank Antoine Leblanc-Hotte for welcoming me to the lab and guiding me through the intricacies of graduate research. His mentorship has inspired me to welcome new laboratory members with the same warmth and guidance. I am also grateful to Ahmed S. Bahgat and Thomas Lacasse for our insightful discussions and friendship. I would like to express my sincere gratitude to my interns, Rizki Arif Pradono, Nathan Ferga, and Zoë Newman-Gougeon, for their contributions, enthusiasm, and valuable assistance throughout this research. I appreciate the opportunity to have mentored them, which allowed me to learn as much as they did. I would also like to thank the current group members, Salvador Poveda Hospital, Nicole Tebchrany, Nicolas Malo, Thomas Grenon, Louis-Frédéric Racicot, and Richard Bienvenu BOMBA, for their friendship, collaboration, and stimulating discussions. With them, the laboratory has become dynamic and thriving. I wish them all the best in their own research projects. I am especially grateful to Cédric Lemieux-Leduc and Régis

Guertin, with whom I embarked on this journey at the master's level and continued through the PhD. Thank you for our friendship, countless discussions, and collaborative efforts on our respective projects. Cédric, your master's thesis provided the foundation for my own work. Régis, I am grateful for our close collaboration on the laboratory's larger gas project which includes the gas setup, the measurements in the barn and the Technopreneur adventure.

I would like to express my gratitude to Polytechnique Montréal, particularly the Department of Engineering Physics, for providing me with an exceptional learning environment for the past eleven years. I am grateful to the funding agencies, the *Fonds de recherche du Québec — Nature et Technologies* (FRQNT) and the Natural Sciences and Engineering Research Council of Canada (NSERC), for their generous financial support in the form of a doctoral scholarship. Additionally, I would like to thank CMC Microsystems for their financial support and for providing access to many tools to the Canadian research community.

I would like to express my sincere gratitude to the members of my thesis committee for their time, expertise, and rigorous evaluation of my work. I am honored that they agreed to serve on my committee.

I would like to thank my friends and family for their constant encouragement and support, especially my parents and brother. I am deeply grateful to my loving wife, Roxanne-Alexandra, for her unwavering support and understanding throughout my studies. Your sacrifices made my ambitions a reality. I am thankful that you believed in me and supported my decision to embark on this journey.

RÉSUMÉ

Les travaux présentés dans cette thèse visent à développer une nouvelle méthode de fabrication de microgouttes polymériques suspendues sur puce, en associant l'impression jet d'encre aux procédés de microfabrication. Ces microgouttes sont des microrésonateurs à modes de galerie pouvant être utilisées pour la détection de gaz. L'absorption de gaz induit un changement de leurs indices de réfraction ainsi que leur expansion. S'ensuit un décalage en longueur d'onde des pics de résonances.

Les capteurs de gaz, indispensables dans des secteurs aussi variés que les mines, la pétrochimie, la santé et l'environnement, constituent déjà des outils précieux. Néanmoins, la demande pour des dispositifs plus compacts, sélectifs et précis ne cesse de croître afin de mieux répondre aux enjeux de sécurité, de diagnostic médical, de surveillance environnementale et d'étude des changements climatiques.

L'objectif principal de ces travaux consiste à mesurer la concentration de différents gaz au sein d'un même mélange à l'aide de microgouttes polymériques intégrées sur puce. Pour pallier le manque de sélectivité d'un seul polymère, il est nécessaire d'avoir une matrice de capteurs de différents polymères. Celle-ci est réalisée grâce à l'impression jet d'encre, couplée à des techniques de microfabrication, permettant ainsi de déposer plusieurs polymères sur un même substrat.

Les polymères SU-8, polystyrène (PS) et polyhexaméthylène biguanide (PHMB) ont été imprimés avec succès. Le choix du PS, insoluble dans l'eau, et du PHMB, soluble dans l'eau, a permis de mettre en évidence la versatilité du procédé de fabrication. Les microgouttes obtenues présentent un diamètre d'environ 100 µm et une forme caractéristique due à l'effet de l'anneau de café. Le bord des résonateurs est suspendu par un procédé au plasma et des sous-gravures allant de 12 à 31 µm sont obtenues.

Pour l'acquisition des spectres de transmission optique, un montage expérimental est utilisé comprenant une source laser accordable, une photodiode et une fibre optique effilée. Les microrésonateurs obtenus présentent des facteurs de qualité élevés, atteignant jusqu'à 2,2 millions pour les structures en polystyrène.

Un montage de contrôle environnemental permet de varier la température du dispositif et des gaz en plus de leurs concentrations. Les analytes étudiés sont l'isopropanol (IPA) et les vapeurs d'eau (H_2O) provenant de bulleurs ainsi que le dioxyde de carbone (CO_2) provenant d'un cylindre de gaz comprimé.

Les mesures expérimentales sont complétées par des simulations numériques réalisées à l'aide de COMSOL Multiphysics. Ce logiciel permet de déterminer les modes optiques des résonateurs à mode de galerie et des guides d'onde, ainsi que de simuler l'expansion thermique des résonateurs polymères. L'analyse du couplage est effectuée à l'aide de MATLAB, en utilisant la théorie des modes couplés. De plus, une longueur de couplage effective est proposée en raison de la configuration de couplage vertical.

La première contribution porte sur la sensibilité thermique des microgouttes en SU-8. Étant donné la sensibilité des polymères aux variations de température et de concentration en gaz, une méthode a été développée pour minimiser l'impact thermique sur les performances du capteur. En ajustant le rapport entre la profondeur de la sous-gravure et le rayon du résonateur, il a été possible d'obtenir un capteur insensible à la température, grâce à la compensation entre les effets thermo-optique et d'expansion thermique.

La deuxième contribution traite de l'évaluation des performances de microgouttes en polymère, fabriquées par jet d'encre, en tant que capteurs de gaz. Neuf combinaisons polymère-analyte ont été étudiées et leur sensibilité ainsi que leur limite de détection ont été déterminées et comparées aux données de la littérature. La plus faible limite de détection, de 14 ppmv, a été obtenue pour une microgoutte en PHMB exposée à la vapeur d'eau.

La troisième contribution porte sur l'intégration de microrésonateurs en polymère avec des circuits photoniques intégrés. Les difficultés liées à l'indice de réfraction effectif trop faible des microrésonateurs suspendus et aux problèmes d'alignement inhérents à la technologie d'impression par jet d'encre ont été identifiées. Une étude comparative approfondie des différents matériaux de gaine et des plateformes photoniques disponibles a été réalisée afin de sélectionner les combinaisons les plus performantes ainsi que l'épaisseur minimale de la gaine. De plus, une technique d'automigration a été proposée pour améliorer la précision d'alignement des microrésonateurs sur le circuit photonique.

Cette étude innove en combinant l'impression jet d'encre et les techniques de microfabrication pour réaliser des microrésonateurs en polymère partiellement suspendus. Ces microrésonateurs présentent l'avantage de pouvoir être insensibles aux variations de température tout en offrant une haute sensibilité à différents gaz. Leur intégration verticale avec des circuits photoniques intégrés permet de développer des capteurs de gaz compacts. De plus, les capteurs optiques, ne posant aucun risque d'explosion ou d'incendie, sont sécuritaires. Ceux-ci peuvent être intégrés à travers un réseau et ainsi utiliser un seul système d'interrogation, diminuant les coûts. Enfin, la diversité des polymères permet la mesure sélective des gaz.

La technologie développée a le potentiel d'être utilisée dans diverses applications telles que la détection de gaz dangereux à l'aide d'un réseau de capteurs dans les mines. De plus, la

dimension restreinte et la sélectivité de ces capteurs devraient permettre la détection précoce du cancer par l'analyse de l'haleine. Enfin, un projet de recherche est en cours pour développer des capteurs optiques basés sur des polymères destinés à mesurer les émissions de méthane dans les fermes laitières, un gaz à effet de serre majeur dans le secteur agricole.

Ces travaux de recherche, en développant une plateforme innovante basée sur des micro-résonateurs en polymère, contribuent non seulement à l'émergence du "nez optique" pour la détection de gaz, mais offrent également des perspectives prometteuses pour la mesure d'autres paramètres physiques. De plus, cette plateforme permet d'envisager l'intégration de composants optiques passifs et actifs à base de polymère avec des circuits photoniques intégrés, ouvrant ainsi la voie à de nouvelles applications.

ABSTRACT

This thesis explores the integration of inkjet printing and microfabrication techniques to produce suspended polymer microdroplets on a single optical chip. These microdroplets, functioning as whispering gallery mode (WGM) resonators, are designed for gas sensing applications. Gas absorption by the polymer matrix induces changes in the resonator's refractive index and radius, resulting in detectable shifts in the resonance wavelengths.

Gas sensors play a crucial role in various sectors, including mining, petroleum, healthcare, and environmental monitoring. While significant advancements have been made, a persistent need exists for compact, selective, and precise gas sensors to address critical challenges like safety, disease detection, pollution monitoring, and climate change research.

The primary goal of this research is to measure the concentration of various gases within a mixture using integrated polymer microdroplets. As individual polymers lack selectivity, an array of microdroplets composed of different polymers is required. To achieve this, we explore the integration of inkjet printing, an additive manufacturing technique, with traditional microfabrication methods.

To fabricate the microdroplets, three distinct polymers were utilized: SU-8 (a photosensitive epoxy), polystyrene (PS), and polyhexamethylene biguanide (PHMB). PS, being insoluble in water, and PHMB, a water-soluble disinfectant, were selected to show the versatility of the method. The fabricated microdroplets, approximately 100 µm in diameter, were observed to display the coffee-ring effect. A plasma etching process was employed to suspend these microdroplets, resulting in undercuts ranging from 12 to 31 µm.

An optical transmission setup, consisting of a tunable laser source, a photodiode, and a tapered optical fiber, was employed to measure the transmission spectra of the fabricated microdroplets. High-quality factor resonances, reaching up to 2.2 million for the PS microdroplet, were observed.

The experimental setup provided precise control over both the temperature and concentrations of the injected gas. The analytes used in this study were isopropanol (IPA) and water (H_2O) vapors, delivered from bubblers, and carbon dioxide (CO_2) gas, supplied from a gas cylinder.

The experimental work was complemented by numerical simulations. The optical modes of the WGM resonators and waveguides were obtained using COMSOL Multiphysics. This software was also employed for thermal expansion simulations. Coupling was analyzed us-

ing coupled-mode theory implemented in MATLAB, and an effective coupling length was determined for the proposed vertical coupling configuration.

The first contribution focuses on investigating the temperature dependence of SU-8 microdroplets. As polymers are sensitive to both gas concentration and temperature which affect the resonance wavelength of the optical resonators, temperature fluctuations can compromise the accuracy of gas measurements. By carefully adjusting the ratio between the undercut and the radius of the resonator, temperature insensitivity can be achieved. This phenomenon arises from the compensation between the thermo-optic effect and polymer expansion. The degree of compensation is directly influenced by the undercut-to-radius ratio, allowing fine-tuning to minimize temperature crosstalk and enhance gas sensing performance.

The second contribution demonstrates the feasibility of using inkjet printed polymer microdroplets for gas sensing applications. The gas sensitivity and limit of detection (LOD) were measured for nine different polymer-analyte combinations and compared to literature values. The lowest LOD achieved was 14 ppmv for water vapor detection using a PHMB microdroplet.

The third contribution studies the integration of WGM resonators with photonic integrated circuits (PICs). Challenges related to the low effective refractive index of suspended polymer microdroplets and inherent alignment tolerances of inkjet printing are addressed. A comparative analysis of bottom cladding materials and PIC platforms is presented, along with recommendations for material selection, platform choice, and minimum thickness. Additionally, a self-migration technique is proposed to address alignment issues.

This work innovates by combining inkjet printing and microfabrication to produce partially suspended polymer resonators. These resonators, leveraging polymer expansion, exhibit temperature insensitivity and high gas concentration sensitivity. The integration of these resonators with photonic integrated circuits (PICs) through vertical coupling opens up new possibilities for compact gas sensing systems. Optical sensing offers inherent safety, eliminating fire and explosion risks. The ability to multiplex multiple sensors with a single interrogation setup can significantly reduce costs, while the use of diverse polymers enables selective sensing.

This technology has the potential to significantly impact gas sensing applications, including the development of safe gas sensor networks for mines to detect harmful gases. The compactness and selectivity of these sensors could enable the detection of cancer biomarkers in patient breath. Additionally, ongoing research aims to utilize these sensors for monitoring methane emissions in dairy barns, a significant contributor to greenhouse gas emissions from the agriculture sector.

This thesis contributes to the realization of an optical nose. Beyond gas sensing, this novel platform holds potential for measuring various other quantities and integrating passive and active polymer optical elements onto a single PIC.

TABLE OF CONTENTS

DEDICATION iii

ACKNOWLEDGEMENTS iv

RÉSUMÉ vi

ABSTRACT ix

TABLE OF CONTENTS xii

LIST OF TABLES xvi

LIST OF FIGURES xviii

LIST OF SYMBOLS AND ACRONYMS xxiii

LIST OF APPENDICES xxix

CHAPTER 1 INTRODUCTION 1
1.1 Gas Sensing Applications 2
1.1.1 Sectors 2
1.1.2 Gas Sensor Market 5
1.2 Problem Statement & Motivation 5
1.3 Objectives & Original Contributions 6
1.4 Thesis Structure 7

CHAPTER 2 LITERATURE REVIEW 9
2.1 Gas Sensing Methods 10
2.1.1 Overview 10
2.1.2 Physical-Chemical Methods 11
2.2 Selectivity 13
2.2.1 Polymers 14
2.2.2 Sensing Array 15
2.2.3 Summary 17
2.3 Optical Resonators 17
2.3.1 Overview 17

2.3.2 Whispering Gallery Mode Resonators 18
2.3.3 WGM Resonator Gas Sensors 19
2.4 Additive Fabrication Techniques 21
2.4.1 Overview 21
2.4.2 Inkjet Printing 22
2.5 Optical Vertical Integration 24
2.6 Synthesis 26

CHAPTER 3 THEORY ON WHISPERING GALLERY MODE GAS SENSORS . . 28
3.1 Slab waveguides 29
3.2 Whispering Gallery Mode Resonators 32
3.2.1 Optical Loss 33
3.2.2 Solutions to the Whispering Gallery Mode Resonator 34
3.2.3 Optical Coupling 39
3.3 Detection Principle 45
3.4 Gas Diffusion in a Polymer Matrix 48
3.4.1 Summary 49

CHAPTER 4 ARTICLE 1 - TEMPERATURE SENSITIVITY CONTROL OF AN INKJET-PRINTED OPTICAL RESONATOR ON PILLAR 51
4.1 Authors and Affiliations 51
4.2 Abstract 52
4.3 Introduction 52
4.4 Microfabrication and Optical Characterization 54
4.5 Temperature Sensitivity Measurements 58
4.6 Modeling and Discussion 58
4.7 Conclusion 65

CHAPTER 5 ARTICLE 2 - SUSPENDED WHISPERING GALLERY MODE RESONATORS MADE OF DIFFERENT POLYMERS AND FABRICATED USING DROP-ON-DEMAND INKJET PRINTING FOR GAS SENSING APPLICATIONS 67
5.1 Authors and Affiliations 67
5.2 Abstract 68
5.3 Introduction 68
5.4 Material and Methods 70
5.4.1 Polymer Inks 70
5.4.2 Microfabrication 70

5.4.3 Analytes . . . 71
5.4.4 Gas Measurements . . . 72
5.5 Results and Discussion . . . 73
5.5.1 Device Characterization . . . 73
5.5.2 Gas Sensitivity . . . 75
5.5.3 Comparison and Discussion . . . 79
5.6 Conclusions . . . 82
5.7 Supplementary Information . . . 82
5.7.1 Surface Tension . . . 82
5.7.2 Viscosity . . . 85
5.7.3 Selectivity . . . 86
5.7.4 Response Time . . . 87

CHAPTER 6 ON-CHIP VERTICAL INTEGRATION OF POLYMER RESONATORS FABRICATED BY INKJET PRINTING . . . 90
6.1 Introduction . . . 90
6.1.1 Problematic . . . 90
6.1.2 Possible Solutions . . . 92
6.2 Proposed Designs . . . 97
6.3 Methodology . . . 98
6.4 Simulation Results and Discussion . . . 100
6.4.1 Minimum Thickness of the Bottom Cladding . . . 101
6.4.2 Misalignment Tolerance . . . 102
6.4.3 Alignment . . . 102
6.4.4 Platform Comparison . . . 105
6.5 Conclusion . . . 106

CHAPTER 7 GENERAL DISCUSSION . . . 108
7.1 Achieved Objectives . . . 108
7.2 Limitations . . . 109

CHAPTER 8 CONCLUSION . . . 111
8.1 Summary of Works . . . 112
8.2 Future Research . . . 112
8.3 Conclusion . . . 115

REFERENCES . . . 117

APPENDICES 146

LIST OF TABLES

Table 2.1 Comparison of quality factors for various whispering gallery mode resonator geometries 18

Table 2.2 Comparison of whispering gallery mode resonator gas sensors of different resonator types and sensing materials 20

Table 4.1 Inkjet printing parameters 54

Table 4.2 Sensitivity measurements for six samples with different undercut-to-radius ratio 59

Table 5.1 Polymer ink properties 71

Table 5.2 Inkjet printing parameters used for the three polymer inks 71

Table 5.3 Comparison among optical gas sensors utilizing polymer sensing materials. This study is highlighted in gray alongside three sensor types: whispering gallery mode (WGM) resonator, Fabry-Perot interferometer (FPI), and photonic crystal (PhC), all utilizing SU-8, PS, and PHMB polymers. Details include the wavelength range λ, sensitivity S, limit of detection (LOD), and the reached maximum concentration $C_{\max}$. . 77

Table 5.4 Measured contact angles for the determination of static surface tension of silicon $\langle 100 \rangle$ with a Piranha treatment or an HMDS coating as well as PS and PHMB inks 83

Table 5.5 Total static surface tension (SFT) of different liquids and solids with their dispersion (d) and polar (p) components. Values for water, ethylene glycol and diiodomethane are reported from the literature. Both silicon $\langle 100 \rangle$ solids with a piranha treatment and an HMDS coating were measured with the help of the three liquids. Both inks with PS and PHMB were obtained with the measured solids. The static surface tensions were calculated from the contact angles with the Owens, Wendt, Rabel and Kaelble method. 84

Table 5.6 Selectivity angles for each pair of gases. 86

Table 5.7 Response times in minutes for both upward and downward transitions, representing 70 % and 90 % of the maximum wavelength shift for each combination of polymer-analyte pairs. 88

Table 5.8 Fit results of the sum of two exponential terms for upward and downward transition of each polymer-analyte pair. τ_1 and τ_2 are the fast and slow time constants, R^2 is the coefficient of determination of the fit, and ratio is defined as C_1 divided by C_2. 89
Table 6.1 Refractive indices at a wavelength of 1550 nm for various materials . . 95
Table 6.2 Optimal performance of the proposed designs 101
Table 6.3 Measured contact angles (θ_c) of HMDS and O_2-plasma surface treatments with three liquid phases 104
Table 6.4 Total surface tensions and the dispersive and polar components for the three liquid phases taken from the software database and the two calculated surface treatments 105

LIST OF FIGURES

Figure 2.1 Concept map of gas sensing methods and materials 11

Figure 2.2 Hansen solubility model represented by a three-dimensional space with axes corresponding to dispersion (δ_d), polar (δ_p), and hydrogen-bonding (δ_h) components. The solubility is determined by the ratio between the distance between the solute and solvent in this 3D space (R_a) and the solute's interaction radius (R_0). Acetone, ammonia (NH_3), benzene, 2-butanol, carbon dioxide (CO_2), ethanol (EtOH), hexane, isopropanol (IPA), toluene and water (H_2O) are the gases (solvents) represented by black dots. Polystyrene (PS), polyvinyl alcohol (PVA) and poly(methyl methacrylate) (PMMA) are the polymers (solutes) represented by colored dots. 16

Figure 2.3 a) Schematic diagram showing drop-on-demand inkjet printing in operation with piezoelectric actuation. b) Parameter space of the Reynolds number Re and Weber number We defining the printable region colored in green. 23

Figure 2.4 Illustration of a side and top-down view of optical coupling methods with a suspended polymer wedge resonator on a chip. 26

Figure 3.1 Total internal reflection of a light ray at the interface between two mediums ($n_1 > n_0$). 28

Figure 3.2 A rectangular disk is decomposed in between a 2D whispering gallery mode resonator and a slab waveguide. 29

Figure 3.3 Slab waveguide of height h and an example of an optical mode amplitude $\Psi(x)$ 30

Figure 3.4 a) First five modal solutions U_p of the transcendental equations for the slab waveguide for both polarization TE and TM shown as modal parameter U as a function of waveguide parameter V. b) Corresponding refractive index. 31

Figure 3.5 Theoretical transmission spectrum of a whispering gallery mode resonator. 33

Figure 3.6 Solutions to the transcendental equations of the whispering gallery mode resonator for both polarization (transverse electric (TE) and transverse magnetic (TM)). Each solution is a blue dot. 35

Figure 3.7 Radial amplitudes of the first solutions to a whispering gallery mode resonator with a refractive index ratio of 2. The azimuthal mode number is 10. 36
Figure 3.8 Whispering gallery mode amplitude of a disk with a radius R. The resonance mode has azimuthal number 10, and radial number l. . . . 36
Figure 3.9 Calculated TE and TM mode profiles for a rectangular resonator with a radius of 50 µm and a thickness of 2 µm. The mode numbers (m,pl), effective indices (n_{eff}), and polarization types (TE or TM) are labeled for each mode. 38
Figure 3.10 a) Vertical coupling between a disk resonator and a waveguide b) by the coupled mode theory with a effective length, L_{eff}. c) Horizontal and total separation as a function of the light propagation in z d-f) and their derivatives. 40
Figure 3.11 Evolution of power coupling between waveguides for varying beating lengths. 43
Figure 3.12 Illustration of the coupling between a waveguide and a resonator by the matrix method. The light amplitudes a, b, c, and d are related with the coupling matrix $\Phi(z)$ evaluated for a coupling length equals to the flat zone length L_{eff} and the propagation in the resonator. . . . 43
Figure 3.13 Detection principles of optical resonator sensors comprising a) wavelength shift, b) width variation, c) intensity variation and d) mode split. 46
Figure 3.14 a) Gas diffusion in a semi-infinite thin polymer film and b) the resulting mean concentration with time. 48
Figure 4.1 Temperature sensing mechanism of an all-polymer microdroplet on pillar. a) A peak shift ($\Delta\lambda$) is observed when the resonance condition varies with temperature (ΔT). b) This shift is attributed to thermal expansion (ΔR) and change of the refractive index (Δn). 55
Figure 4.2 a) Fabrication process of a polymer microdroplet on pillar. b) In-flight inkjet-printed droplets ejected from the printhead. c) Top-down view of a microdroplet, revealing the underlying pillar. d) Scanning electron microscope images of the microdroplet on pillar. e) Radial height profile of the microdroplet. 55
Figure 4.3 Optical transmission spectrum of a tapered optical fiber coupled to a microdroplet on pillar with a close-up view of a peak, along with a schematic representation of the experimental setup utilized. 57

Figure 4.4 a) Experimental setup for the temperature sensitivity measurements. b) Spectra at different temperatures showing the peak displacement. c) Tracking of a single peak position while varying the temperature over time. d) Linear regression of the peak displacement versus temperature. 59

Figure 4.5 a) Simulated thermal expansion displacement field, with the displacement exaggerated by a factor of 5 for a temperature variation of 10 °C. b) Simulated optical mode, showcasing the electric field amplitude of the fundamental mode with the previous deformed resonator shape for a temperature variation of 10 °C. c) Displacement analysis of the mode maximum and drop edge along the r and z axes as temperature increases. d) Variation in refractive index change based on the thermo-optic coefficient and the effective refractive index with temperature. . 61

Figure 4.6 a) Study of the effect of both thermo-optic and thermal expansion coefficients on the resonance shift with temperature. b) Temperature sensitivity variation across u/R ratios for different modes of both TE and TM polarization. c) Comparative analysis between experimental results and simulation using measured coefficients. 64

Figure 5.1 Working principle of a WGM-based gas resonator. a) Side-view model of a polymer resonator (purple) onto a silicon pillar. b) Sectional view of the resonator and the optical mode with representation of the changes in the refractive index (Δn) and in the resonator's radius (ΔR). c) Optical transmission spectrum illustrating the displacement of the resonance peak when exposed to a gas. 69

Figure 5.2 Microfabrication of a suspended microdroplet resonator a) Overview of the fabrication steps: Deposition of a polymer ink by inkjet printing on a cleaned silicon substrate (step 1). Solvent evaporation (steps 2) and optional UV curing (steps 3). Plasma etching of the substrate to underetch the microdroplet (step 4). b) An SU-8 microdroplet ejected from the inkjet nozzle. c) Scanning electron microscope micrograph of a final SU-8 resonator (highlighted in purple) on a pillar. 72

Figure 5.3 Gas measurement methodology. a) Measurement setup incorporating the optical circuit (tunable laser source TLS, polarization controller PC and photodetector PD), the gas circuit (gas cylinders, mass flow controllers (MFCs) and bubbler), temperature controllers (copper heater H, thermoelectric controller TEC) and the gas box (device and tapered optical fiber TOF). b) Measurement example demonstrating the tracking of a resonance peak around 1554 nm as concentration varies with time. c) Example of sensitivity regression for a humidity measurement. Both examples are from the suspended SU-8 microdroplet exposed to varying humidity concentration. 74

Figure 5.4 Geometric characterization of the resonators from the three polymers. a) Optical microscope micrographs indicating the resonator radius r_r and the pillar radius r_p. b) Radial profilometry of the polymer microdroplets from the center to the edge before the underetch step. 75

Figure 5.5 Examples of spectra obtained for the suspended microdroplets of the three distinct polymers, namely SU-8, PS and PHMB, along with the free spectral range (FSR) and the corresponding peak's highest Q-factor. 76

Figure 5.6 Resonance peak wavelength shifts versus analyte concentrations for every analyte-polymer pairs. Each graph is for a different analyte and contains three sets of measurements, one for each polymer. The dashed lines indicate the linear regressions used to obtain the sensitivities. . . 76

Figure 5.7 Optical contact angle measurements with instrument OCA-20 from Data Physics 83

Figure 5.8 Viscosity measurement of PS and PHMB inks with linear regressions. The slope of the shear stress by the shear rate is the dynamic viscosity. The rotational viscometry measurements were made with the rheometer MCR 501 of Anton Paar with a double-gap spindle DG 26.7 at 25 °C. 85

Figure 5.9 Transient response curves for each polymer-analyte combination, displaying both upward and downward transitions. The response times at 70 % and 90 % of the overall wavelength shifts are indicated by dashed and dash-dotted vertical lines respectively, matching the color code of the corresponding analyte. 88

Figure 6.1 Refractive index distribution of polymers at 632 nm 91

Figure 6.2 TE0 optical resonance modes of polymeric droplet resonators fabricated from a) SU-8, b) PS, and c) PHMB, with calculated effective refractive indices (n_{eff}). The color scale represents the electric field amplitude, and the white arrows indicate the radial and axial components. . . . 92

Figure 6.3 a) Effective refractive index and quality factor of an SU-8 resonator as a function of its distance from a glass substrate. b) Visualization of optical mode leakage from the SU-8 resonator into the glass substrate for a separation of 0.5 µm. 93

Figure 6.4 a) Effective refractive index of a suspended polymer resonator similar in shape to the SU-8 resonator as a function of the polymer's refractive index. b) Difference between the effective refractive index and the polymer refractive index for a spherical cap resonator plotted against the contact angle for three different polymer refractive indices. Both graphs were obtained by numerical calculation. 94

Figure 6.5 A general process flow illustrating the microfabrication of an integrated microdrop resonator over a photonic integrated circuit. This versatile process accommodates a wide range of materials and microfabrication techniques. 99

Figure 6.6 Top-down and cross-section views of the simulation geometry of a suspended polymer resonator coupled to a slab waveguide. 100

Figure 6.7 Alignment tests with surface modification. a) Schematic of the test chip and the self-migration of the SU-8 droplets. b) Optical micrographs of the test chip without microdroplet (1), and with microdroplets where an offset is used (2-4). 106

Figure B.1 Numerical calculation results of the effective refractive indices of rib waveguides as a function of their widths and thicknesses for different core materials (SiO_2 and SU-8) and the maximum peak heights of the transmission spectra of these waveguides coupled to a SU-8 microdrop resonator. 150

Figure B.2 Numerical calculation results of the effective refractive indices of ridge waveguides as a function of their widths and thicknesses for different core materials (SiN, SiO_2 and SU-8) and the maximum peak heights of the transmission spectra of these waveguides coupled to a SU-8 microdrop resonator. 151

LIST OF SYMBOLS AND ACRONYMS

List of acronyms

2PP	Two-photon polymerization
CFC	Chlorofluorocarbon
CH_4	Methane
CIJ	Continuous inkjet
CMP	Chemical-mechanical polishing
CMT	Coupled mode theory
CMUT	Capacitive micromachined ultrasonic transducer
CO_2	Carbon dioxide
DI	Dionized
DLW	Direct laser writing
DOD	Drop-on-demand
DPN	Dip pen nanolithography
EHD	Electrohydrodynamic
FDM	Fused deposition modeling
FPI	Fabry-Perot interferometer
FSR	Free spectral range
FWHM	Full width at half-maximum
H_2O	Water
HF	Hydrogen fluoride
HMDS	Hexamethyldisilazane
ICP	Inductively coupled plasma
IoT	Internet of Things
IPA	Isopropanol
IR	Infrared
LOD	Limit of detection
LOQ	Limit of quantification
LSER	Linear solvation–energy relationships
MFC	Massflow controller
MOF	Metal-organic framework
MOS	Metal oxide semiconductor
MSE	Mean squared error

MTMS	Methyltrimethoxysilane
PAHCl	Polyallylamine hydrochloride
PANI	Polyaniline
PC	Polarization controller
PCA	Principal component analysis
PD	Photodetector
PDMS	Polydimethylsiloxane
PECVD	Plasma-enhanced chemical vapor deposition
PEDOT	Poly(3,4-ethylenedioxythiophene)
PEG	Polyethylene glycol
PEVA	Poly(ethylene-vinyl acetate)
PGMEA	Propylene glycol methyl ether acetate
PhC	Photonic crystal
PHMB	Polyhexamethylene biguanide
PIC	Photonic integrated circuit
PID	Proportional–integral–derivative
PMMA	Polymethylmethacrylate
PPy	Popypyrrole
PS	Polystyrene
PTFE	Polytetrafluoroethylene
PTh	Polythiophene
Q-factor	Quality factor
QCM	Quartz crystal microbalance
RIE	Reaction ion etching
RTD	Resistance temperature detector
SAW	Surface acoustic wave
SEM	Scanning electron microscopy
SF_6	Sulfur hexafluoride
SLA	Stereolithography
SLM	Selective laser melting
SNR	Signal-to-noise ratio
SOG	Spin-on-glass
SU-8	Epoxy-based photoresist
TE	Transverse electric
TEC	Thermoelectric controller
TEOS	Tetraethoxysilane

TLS	Tunable laser source
TM	Transverse magnetic
TMOS	Tetramethoxysilane
TOF	Tapered optical fiber
TRL	Technology readiness level
UV	Ultraviolet
VOC	Volatile organic compound
WGM	Whispering gallery mode

List of symbols

a_i	Mode amplitudes
B	Power ratio inside the resonator (dB)
Bo	Bond number
C	Concentration (ppm)
C_0	Initial concentration (ppm)
C_{air}	Concentration of analyte in air (ppm)
C_{max}	Maximum concentration (ppm)
$\overline{C}$	Mean concentration (ppm)
c_0	Speed of light in vacuum (m/s)
D	Diffusion coefficient (µm^2/s)
d	Characteristic length or thickness (µm)
E	Energy of vaporization (J) or electric field (V/m)
$\overrightarrow{e_i}$	Vector waveguide modes
$f(R)$	Function of the substrate's surface roughness R
H	Magnetic field (A/m)
$H_m^{(1)}$	Hankel functions of the first kind
$\overline{\mathbf{H}}$	Total coupling matrix (W/m)
h	Waveguide thickness (µm)
h_c	Critical waveguide thickness (µm)
$\overrightarrow{h_i}$	Vector waveguide modes
J	Gas flux (ppm/µm^{2}s)
J_m	Bessel functions of the first kind
K_{p-a}	Partition coefficient
$\mathbf{K}$	Coupling matrix (W/m)

k	Integer
k_0	Wavenumber (nm^{-1})
L_b	Beating length (µm)
L_C	Coupling length (µm)
L_{eff}	Effective coupling length (µm)
$L_{\max}$	Effective beating length (µm)
l	Radial mode number
m	Modal number
n	Optical refractive index
n_0	Core refractive index
n_1	Cladding refractive index
n_b	Bottom cladding refractive index
n_{eff}	Effective refractive index
n_p	Polymer refractive index
Oh	Ohnesorge number
OPL	Optical path length (µm)
P	Pressure (Pa) or porosity (%)
$\mathbf{P}$	Power matrix (W)
p	Mode number
Q	Quality factor
Q_{c}	Coupling quality factor
Q_{int}	Intrinsic quality factor
Q_{rad}	Radiation quality factor
Q_{sa}	Surface absorption quality factor
Q_{ss}	Surface scattering quality factor
Q_{tot}	Total quality factor
Q_{va}	Volume absorption quality factor
Q_{vs}	Volume scattering quality factor
R	Radius of the resonator (µm) or ideal gas constant ($J\,mol^{-1}\,K^{-1}$)
R^2	Coefficients of determination
R_0	Interaction radius ($MPa^{0.5}$)
R_a	Distance between the solute and solvent ($MPa^{0.5}$)
$R_{n,m}$	Selectivity angle (°)
Re	Reynolds number
RED	Ratio of R_a by R_0
r	Radial coordinate (µm) or pore radius (nm)

r_p	Pillar radius (µm)
r_r	Resonator radius (µm)
S	Sensitivity to temperature (nm/°C) or gas concentration (nm/ppm)
$\vec{S_n}$	Selectivity vector (nm/ppm)
s	Structure vertical separation (µm)
$s_h(z)$	Modal horizontal separation (µm)
$s_T(z)$	Modal total separation (µm)
T	Transmission (dB)
$T_{\max}$	Highest transmission peak (dB)
t	Time (s)
t_b	Bottom cladding thickness (µm)
t_w	Waveguide thickness (µm)
U	Modal parameter
u	Undercut of the suspended resonator (µm)
V	Waveguide parameter
V_m	Molar volume (m^3/mol)
v	Ink velocity (m/s)
W	Modal parameter
We	Weber number
w_w	Waveguide width (µm)
x	X coordinate (µm)
y	Y coordinate (µm)
Z	Z number
z	Z, axial or propagation coordinate (µm)
α	Accumulated loss (dB)
α_r	Linear loss (dB/µm)
α_{vscat}	Volume scattering loss (dB/µm)
β	Propagation constant (μm^{-1})
γ	Surface tension (mN/m)
Δc	Change in analyte concentration (ppm)
Δn	Change in refractive index
ΔR	Change in radius of the resonator (µm)
ΔT	Change in temperature (°C)
$\Delta \epsilon$	Change in elongation (%)
$\Delta \lambda$	Wavelength shift of a resonance peak (nm)
δ_d	Dispersion solubility parameter ($MPa^{0.5}$)

δ_H	Hildebrand solubility parameter ($MPa^{0.5}$)
δ_h	Hydrogen-bond solubility parameter ($MPa^{0.5}$)
δ_p	Polar solubility parameter ($MPa^{0.5}$)
δx	Structure horizontal separation (µm)
$\delta\lambda$	Peak's full width at half maximum (FWHM) (nm)
ϵ_0	Vacuum permittivity (F/m)
θ	Azimuth coordinate (rad)
θ_i	Incident angle (°)
κ	Coupling constant
λ	Wavelength of light (nm)
λ_0	Wavelength of a resonance peak (nm)
λ_{FSR}	Free spectral range (nm)
λ_m	Wavelength of the m-th mode (nm)
μ	Ink viscosity (mPa s)
$\xi^{(i)}$	Eigenvectors
ρ	Density (g/mL)
σ	Noise of the peak position (nm)
τ_1	Response time (s)
τ_p	Photon lifetime (s)
ϕ	Accumulated phase (rad) or analyte concentration (ppm)
ϕ_a	Absorbed volume fraction of an analyte (ppm)
Ψ	Optical wave amplitude
$\Psi(z)$	Amplitude evolution
$\mathbf{\Psi}(z)$	Evolution matrix
ω_0	Angular frequency (rad/s)
$\mathcal{F}$	Finesse

LIST OF APPENDICES

Appendix A Diffusion of a gas in a polymer slab from both sides 146
Appendix B Numerical Comparison of the Effective Refractive Index and Transmission Peak Height of Waveguides With Different Materials, Configurations and Dimensions. 150

CHAPTER 1 INTRODUCTION

Our perception of reality is solely based on the input of our senses. The "Brain in a vat" hypothesis illustrates the limit of our existence by supposing that our brain could be in a vat and kept alive while being fed false sensory signals. This concept is similar to the movie "The Matrix" where humans are kept in a computer simulation. It can be summarized by this quote of Morpheus to Neo:

> What is real? How do you define "real"? If you're talking about what you can feel, what you can smell, what you can taste and see, then "real" is simply electrical signals interpreted by your brain.

While the philosophical question of our reality, explored in ontology, challenges the limits of human perception, it highlights the crucial role of our senses in experiencing the world. Traditionally, we recognize five human senses: sight, hearing, smell, taste, and touch. However, we can also consider additional senses, such as balance and various internal senses like hunger. These senses enable us to perceive the world and respond to stimuli.

Humans have developed devices to replicate and extend their sensory capabilities, such as microphones, pressure sensors, and cameras. Additionally, we have created devices to detect other physical quantities, including electromagnetic fields, acceleration, and temperature. In some cases, these devices surpass human sensory limitations. For example, single-photon cameras, hyperspectral cameras, and infrared and ultraviolet cameras offer capabilities beyond the human eye.

Our senses of smell and taste still have to be outperformed. Humans can discriminate over one trillion olfactory stimuli [1] with a very fast response time of about 1 s [2]. Nevertheless, some gas sensing methods are better than our nose for some aspects of performance. First, our nose detects odors and not chemical species directly. An odor is a mixture of odor molecules that will trigger some receptor neurons which are expressed by 400 functional genes [3]. For example, the smell of a rose comes from a mixture of 275 components. Thus, our sense of smell is only subjective and qualitative [4]. This has not been a barrier for professional perfumers which are called 'noses'. With their trained olfaction capabilities, complex perfumes were developed. Similarly, in the winery industry, professionals smell the wine to comment and adjust the final mixes. However, in some cases, it might be necessary to have a continuous monitoring of the gas environment and the need to detect harmful gases where human capabilities are exceeded. Some gases, like carbon dioxide and carbon

monoxide, are imperceptible to humans, or may be present at concentrations too high for safe exposure.

Our understanding of gases is relatively recent. The term "gas" was coined by Dr. Johann Baptist Van Helmont in 1610, and the foundations of scientific gas analysis were laid by Robert Bunsen in 1837. Since then, gas sensors have been developed to measure gas concentrations at the parts-per-trillion (ppt) level.

1.1 Gas Sensing Applications

Gas sensors, essential devices in various applications, are categorized into two primary functions: quality assurance and security monitoring. Quality assurance necessitates precise quantification of gas concentrations to safeguard the environment and optimize system performance. On the other hand, security monitoring demands the timely detection of gas levels exceeding critical thresholds to ensure plant safety and protect occupational health.

1.1.1 Sectors

Food Industry

Winemakers and brewers, pioneers in gas detection, recognized the dangers of fermentation in confined spaces like cellars. To mitigate risks, they employed a simple yet effective method: the candle test. A flickering or extinguished flame indicated unsafe conditions, signaling the presence of carbon dioxide, a gas that can displace oxygen and lead to asphyxiation. While this historical technique provided a basic level of safety, its reliability is limited, highlighting the need for more sophisticated gas detection methods.

Today, gas sensors find widespread application in the food industry, encompassing a diverse range of uses. These include oenology for wine analysis, food storage, animal anesthesia, greenhouse monitoring, fruit and vegetable ripening, microalgae cultivation, meat spoilage detection, and modified atmospheric packaging techniques [5].

For instance, gas sensors are employed to assess the freshness of kiwifruit by measuring volatile organic compounds (VOCs), which exhibit distinct patterns between ripe and overripe stages. This non-destructive, portable, and real-time method offers a reliable means of monitoring kiwifruit quality [6].

Spoiled food poses a significant health risk due to the release of toxic vapors which are detectable by gas sensor arrays [7]. The detection of sulfurous compounds and biogenic amines aids in assessing meat freshness [8], while formaldehyde detection indicates the freshness of

fruits [9].

Mining and Petrochemical Industry

The Davy lamp, invented in 1816, was a pioneering effort to protect coal miners from methane (CH_4) and other flammable gases. This oil lamp, equipped with a mesh screen to act as a flame arrestor, provided a visual warning: a heightened, reddish flame signaled unsafe conditions. However, the device's susceptibility to misuse and its false sense of security contributed to numerous mining accidents and fatalities.

Canaries, more sensitive to harmful gases than humans, subsequently took over as early warning systems. Their cessation of chirping served as an alarm to evacuate the mine. It wasn't until the 1950s that electronic gas sensors, offering greater reliability, began to replace these birds.

The mining and petrochemical industries, which deal with a variety of toxic and explosive gases like carbon monoxide, hydrogen, methane, ethane, and ammonia, face significant safety challenges for both workers and the surrounding communities. Prompt detection of gas emissions within the initial hours is crucial to mitigate these risks [10].

Environment and Climate Change

The Earth's atmosphere is primarily composed of nitrogen (78 %), oxygen (21 %), argon (0.9 %), carbon dioxide (0.03 %), and other trace gases (0.07 %). Water vapor, though highly variable, can range from 0 % to 8 % and plays a significant role in atmospheric processes. This delicate balance of gases is essential for sustaining life on Earth.

However, human activities, particularly industrialization, have disrupted this equilibrium. The release of chlorofluorocarbons (CFCs) from air conditioning systems and refrigeration units has led to the depletion of the ozone layer, which shields the planet from harmful ultraviolet radiation. Recognizing this threat, the Montreal Protocol was ratified by 198 countries to phase out the production and consumption of CFCs.

Another pressing environmental issue is acid rain, caused by the emission of sulfur dioxide and nitrogen oxide. These pollutants react with atmospheric water vapor to form sulfuric acid and nitric acid, which can have detrimental effects on ecosystems and human health. These two examples underscore the imperative to monitor atmospheric gas concentrations to document and address these environmental challenges through appropriate legislation.

The next major environmental crisis is climate change, driven by the greenhouse effect. Gases

such as carbon dioxide, methane, and water vapor trap heat from the sun, maintaining Earth's temperature within a habitable range. However, increased concentrations of these gases, primarily due to anthropogenic emissions, are causing global temperatures to rise, leading to significant climate disruptions [11].

While CH_4 emissions are lower than carbon dioxide, their global warming potential is significantly higher, approximately 25 times greater. Agriculture contributes approximately 18 % of anthropogenic greenhouse gas emissions, with enteric CH_4 from ruminants being a major contributor. Reducing CH_4 emissions per dairy product through dietary modifications and selective breeding can mitigate this impact [12]. It's important to note that most enteric emissions are released through eructation and lung respiration, rather than flatulence.

Beyond climate change mitigation, reducing enteric methane can enhance feed efficiency, as CH_4 represents an energy loss for the animal. This can lead to direct economic benefits for producers, even before potential future regulations like carbon taxes incentivize greenhouse gas reduction efforts.

Another significant greenhouse gas is sulfur hexafluoride (SF_6), primarily produced for electrical switchgear and electronics manufacturing. This emerging climate change challenge necessitates innovative monitoring solutions for greenhouse gases.

Air Quality

Volatile organic compounds (VOCs) are organic compounds that readily evaporate at standard temperature and pressure. Common VOCs include acetaldehyde, acetone, carbon tetrachloride, ethyl acetate, heptane, hexane, isopropyl alcohol, formaldehyde, naphthalene, and styrene, many of which are toxic. Among these, benzene, toluene, ethylbenzene, and xylene (BTEX) are particularly hazardous aromatic hydrocarbons essential to the petroleum industry. Other harmful gases include carbon dioxide, carbon monoxide, ozone, radon, and ammonia. The Canadian government has established exposure limit recommendations for several of these gases [13].

Toxic VOCs and gases originate from various sources, including industrial emissions, vegetation, petroleum products, coal combustion, cigarette smoke, combustion processes, cleaning products, laser printers, floor adhesives, paint, wood paneling, and vehicular emissions. Gas sensors are crucial for monitoring air quality, identifying localized emission sources, and safeguarding public health both indoors and outdoors. Air pollution has been linked to increased COVID-19 transmission [14], while chemical warfare agents pose a threat in the event of armed conflict, terrorist attacks, or laboratory accidents [15]. The concept of smart cities,

characterized by networks of gas sensors deployed across urban areas, offers a promising approach to preventing exposure to harmful gases [16].

Healthcare

In healthcare, gas sensors were initially employed for anesthetic gas analysis. More recently, dogs have been utilized to detect cancer-related VOCs in patients' breath [17, 18]. However, the impracticality of using dogs in hospitals and their potential unreliability necessitate the development of portable gas sensors capable of detecting these low-concentration biomarkers.

1.1.2 Gas Sensor Market

To address these challenges and meet growing demand, gas sensors must be cost-effective, sensitive, selective, and robust. They must also be capable of detecting target gases in complex mixtures. Additionally, with the advent of the internet of Things (IoT), there is a growing need for miniaturized, portable, and connected gas sensors to enable a wide range of applications.

The global gas sensor market is projected to reach USD 2.53 billion in 2032, with over 13 million units produced. This market is expected to grow at a compound annual growth rate (CAGR) of approximately 8 % between 2024 and 2032, driven by increasing demand for air quality monitoring, industrial safety, and healthcare applications [19]. Carbon dioxide detection currently dominates the market, but emerging regulations are likely to stimulate demand for connected gas sensors across various sectors.

This increased connectivity will not only enhance safety and efficiency but also enable predictive maintenance, allowing for proactive responses to potential hazards.

1.2 Problem Statement & Motivation

Ongoing research is dedicated to the development of advanced gas sensors. Currently, various technologies, each with distinct advantages, are available. A comprehensive comparison of these technologies is presented in the literature review (Sec. 2.1). Polymer-based gas sensors are particularly noteworthy due to their versatility, room-temperature operation, and portability.

Physical-chemical gas sensors, including polymer-based sensors, rely on changes in material properties upon gas absorption. Optical methods, known for their high sensitivity, are well suited for detecting these property changes. Furthermore, the use of optical fibers for sig-

nal transmission offers low loss and compatibility with optical networks. The absence of electronics at the sensing device eliminates the risk of fire or explosion.

Previous research has demonstrated the potential of polymer-functionalized Fabry-Perot interferometers (FPIs) for gas concentration measurement [20, 21]. However, the inherent lack of selectivity in polymers necessitates the use of multiple sensing elements with different polymer coatings [22].

High-quality resonators offer the advantage of narrow resonance peaks. Previous research has demonstrated the use of polymer disk resonators for humidity sensing [23]. These devices were fully integrated on-chip, coupled with a waveguide. However, due to the disk's attachment to the substrate, only changes in the polymer's refractive index contribute to the sensing mechanism, limiting sensitivity compared to polymer-functionalized FPIs. To enhance sensitivity, suspended polymer disk resonators on pillars have been proposed, as they can leverage both refractive index changes and polymer expansion [24]. A limitation of this approach is the loss of device integration. Coupling light to the resonator requires a fragile tapered optical fiber. Furthermore, traditional UV photolithography, used to fabricate these disk resonators, is restricted to a single UV-sensitive polymer per optical chip, preventing the realization of sensing arrays.

To address these limitations, an integrated suspended polymer disk resonator fabricated using an additive fabrication technique is proposed. Specifically, inkjet printing is selected for its ability to rapidly produce high-quality factor resonators. This technique has been successfully employed to fabricate microdisk lasers and biosensors [25–28]. Additionally, inkjet printing offers a wide range of printable polymer inks, enabling the development of diverse sensing devices.

1.3 Objectives & Original Contributions

The primary objective of this thesis is to:

> Measure the concentration of multiple gases within a mixture simultaneously using suspended microresonators fabricated from various polymers. These microresonators will be integrated on-chip through inkjet printing and vertically coupled with a photonic integrated circuit.

To achieve this goal, the following specific objectives have been established:

(A) Investigate the temperature dependence of inkjet-printed polymer microresonators.

(B) Measure the sensitivity and limit of detection of different polymer suspended microresonators fabricated using inkjet printing.

(C) Develop a photonic integrated gas sensing platform by optimizing the integration of inkjet-printed polymer resonators on a single chip.

Having outlined the objectives, it is now crucial to consider their impact. The proposed fabrication method, combining inkjet printing and microfabrication, holds significant potential for realizing suspended whispering gallery mode resonators with high quality factors, fabricated from diverse polymers integrated onto a single optical chip.

Specifically, the first specific objective (A), investigating the temperature dependence of these devices, is essential for understanding and mitigating the influence of temperature fluctuations on gas sensor performance. A thorough understanding of this temperature dependence is critical for minimizing cross-talk and reducing added noise. Developing a strategy for temperature-insensitive sensor operation would represent a substantial advancement in sensor performance and reliability.

Furthermore, specific objective (B), focused on gas sensor applications, serves to demonstrate the versatility of the proposed fabrication method. By utilizing multiple polymers and analytes, this objective not only highlights the method's adaptability but also provides valuable insights into the potential performance characteristics of the devices as gas sensors. This exploration of diverse materials and analytes is crucial for optimizing sensor selectivity and sensitivity.

Finally, the development of a photonic platform for device integration (objective C) showcases the feasibility of creating a sensing array comprising different polymers on a single optical chip. This integrated approach is fundamental to achieving selective sensing with polymers, enabling the simultaneous detection of multiple analytes with enhanced specificity. Moreover, this integration contributes to the realization of compact and efficient sensing devices, a critical factor for miniaturized applications.

1.4 Thesis Structure

The thesis begins by a literature review on gas sensing, optical microresonators, additive fabrication techniques, and optical vertical integration (Ch. 2). A theoretical framework on whispering gallery mode resonator sensors is presented to facilitate understanding of following chapters (Ch. 3).

The subsequent chapter (Ch. 4) integrates the first article, which details the fabrication of

inkjet-printed optical resonators. In this preliminary work, coupling is achieved through a tapered optical fiber. The temperature sensitivity and its correlation with the microresonator's undercut are investigated (sub-objective A).

The second article, presented in the next chapter (Ch. 5), builds upon the previous work by demonstrating the versatility of the fabrication process. Microresonators made of two additional polymers are fabricated, and their application in gas sensing is explored through the measurement of their sensitivity to three different analytes (sub-objective B).

Each article addresses a specific sub-objective and constitutes the first two main themes of this thesis. The final theme, presented in Chapter 6, focuses on the integration of suspended polymer microresonators on a chip. The challenges associated with the low effective refractive index of the optical resonance mode are discussed, and various photonic platforms are proposed and analyzed. The chapter concludes with recommendations for optimal integration strategies (sub-objective C).

The thesis concludes with a summary of the work (Ch. 8). Potential limitations are discussed, and directions for future research are proposed.

CHAPTER 2 LITERATURE REVIEW

A sensor is a device that transduces a physical quantity (e.g., temperature, pressure, light intensity) into a measurable electrical or optical signal. This signal can then be processed to detect or quantify the original physical quantity. A sensor exhibits a wide range of characteristics [29].

A crucial characteristic of a sensor is its sensitivity, which quantifies the change in output signal per unit change in input quantity. For instance, a resistance temperature detector (RTD) might have a sensitivity of X Ω per °C. This metric allows for comparisons between sensors with similar output types.

Beyond sensitivity, other performance metrics influence a sensor's capabilities. Reversibility refers to a sensor's ability to produce the same output for a given input, regardless of whether the input is increasing or decreasing. Precision, resolution, and accuracy define a sensor's ability to provide reliable and precise measurements.

However, several factors can limit a sensor's performance. Hysteresis, repeatability, stability, and zero-shift can introduce errors and affect the long-term reliability of a sensor. Additionally, selectivity, or a sensor's ability to respond primarily to the target quantity, can be compromised by interference from other physical factors, such as temperature or electromagnetic fields.

These sources of errors will limit the range of measurable values. The limit of detection (LOD) is the lowest quantity that can be detected and is defined as three times the standard deviation on the noise without the unknown quantity over the sensitivity. Moreover, the limit of quantification (LOQ) is the lowest quantity that can be quantified which is defined as ten times the standard deviation on the noise without the unknown quantit over the sensitivity.

The temporal response of a sensor, encompassing its response time, recovery time, and bandwidth, is crucial for applications where timely measurements are essential.

Beyond temporal response, a sensor's practical utility is influenced by factors such as physical dimensions, weight, material composition, complexity, lifespan, power requirements, and cost. For instance, space applications necessitate low-power consumption sensors. Portability is another key characteristic, with chip-based sensors enabling on-site measurements.

The subsequent literature review delves into various gas sensing methods, with a particular emphasis on physical-chemical methods and their associated sensing materials. The topic of selectivity is explored, including discussions on chemical engineering of sensing materials,

polymer selectivity, and sensing arrays. Prior to a deeper dive into gas sensing, the review introduces optical resonators, with a focus on whispering gallery mode (WGM) resonators and their applications. Following this, the literature review concentrates on gas sensors employing WGM resonators, providing several examples. The discussion then transitions to additive fabrication techniques, with a specific focus on inkjet printing for optical resonators and gas sensors. Before concluding the chapter, a literature review on optical vertical integration, primarily for disk resonators, is presented.

2.1 Gas Sensing Methods

2.1.1 Overview

Gas sensing encompasses a variety of methods [30, 31] as illustrate in the concept map of Fig. 2.1.

Gas chromatography, often considered the gold standard, involves passing a gas sample through a long column filled with a stationary phase such as a polymeric liquid. This technique excels in separating and detecting individual analytes, offering high selectivity and sensitivity. However, traditional gas chromatography systems are typically bulky. Ongoing research aims to miniaturize this technique onto chip-scale devices [32–34]. Additional separation methods include ion mobility spectroscopy and mass spectrometry.

Gases can be detected through physical means such as paramagnetic [35], mass, thermal conductivity [36], and ionization processes [37]. However, these methods often lack the ability to measure individual gases within a mixture, as the measured quantity typically represents an average of all the analytes present.

Infrared (IR) absorption spectroscopy can measure gas concentration by detecting the light absorption spectra of molecules due to their vibrational modes. For example, acetylene is detected by its absorption at 1531.59 nm [38] with a LOD as low as 76.75 ppb. However, since the absorption is a function of concentration, low concentrations necessitate long optical path lengths (21.9 m) and integration times (340 s). One approach to reduce the device's size and sample volume is to employ mirrors to increase the number of times the light path traverses the sample. Additionally, the absorption wavelengths must be carefully selected, as certain bonds exhibit similar absorption wavenumbers (e.g., 1380 cm^{-1} for C−H and N−O [39]), and similar molecules can possess highly similar absorption spectra. Thus, many applications require the measurement of multiple absorption wavelengths which increase the system's complexity and cost. To miniaturize this type of sensor, resonant metamaterials can enhance the electromagnetic field at the surface, paving the way for on-chip IR absorption

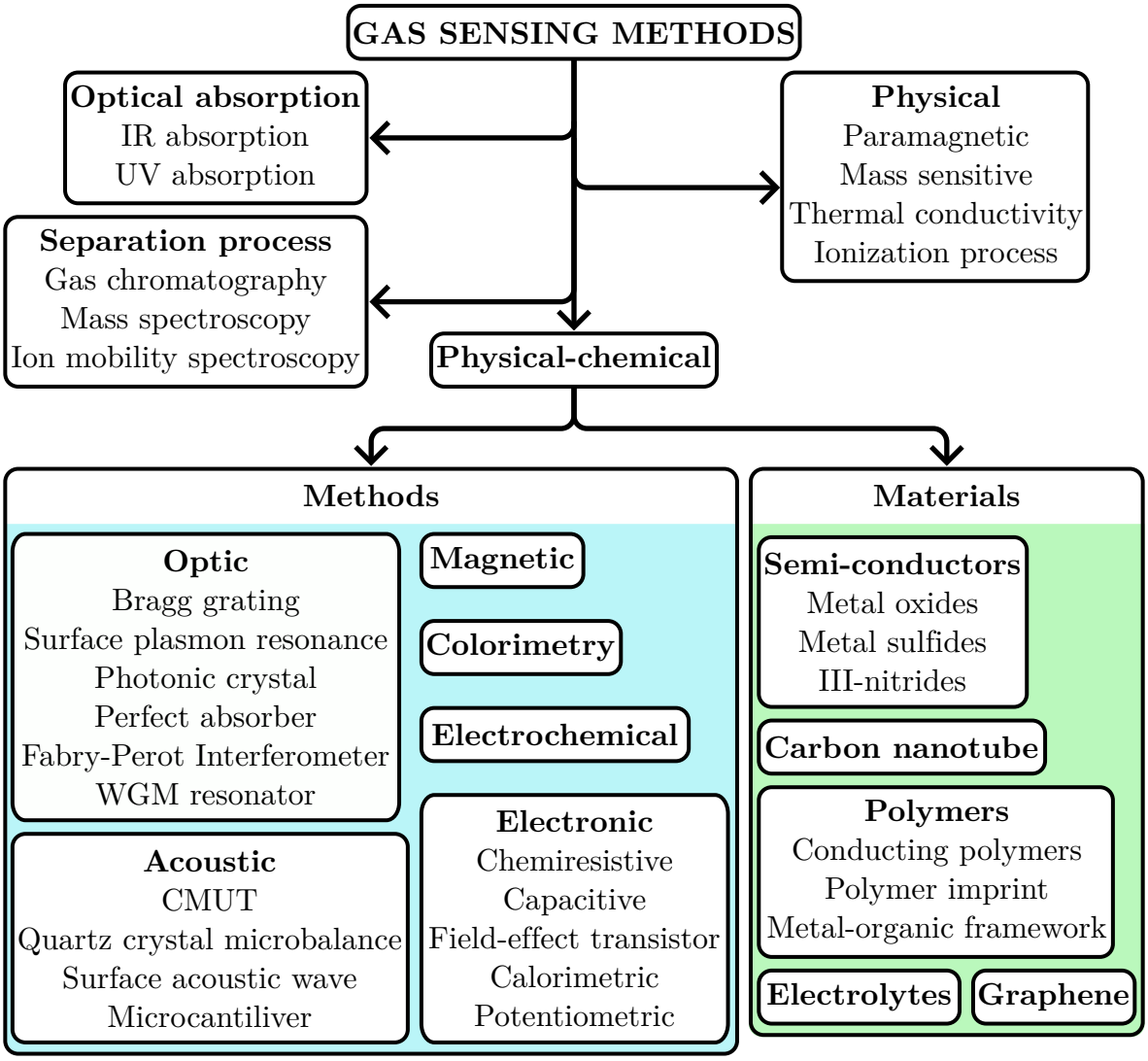

Figure 2.1 Concept map of gas sensing methods and materials

spectroscopy [40].

With the same principle but utilizing electronic transitions, ultraviolet (UV) absorption spectroscopy can also measure gas concentration [41].

2.1.2 Physical-Chemical Methods

Gas sensors can employ physical-chemical interactions, utilizing a sensing material as a transducer. When a gas interacts with the material, changes in its properties can be measured. This indirect detection method differs from the direct methods discussed earlier.

A popular type of gas sensor is the electronic gas sensor. These devices rely on the interaction

between a gas and a material that undergoes changes in its electronic properties, which can then be measured. Electronic gas sensors are further categorized based on the specific parameter measured. This can include resistance (and conductance) [42,43], capacitance [44], field-effect transistor parameters [45], temperature [46], or the voltage and current of an electrochemical cell [47].

Materials can be metal oxide semiconductors (MOSs) such as Cr_2O, ZnO, $ErFeO_3$, CuO, In_2O_3 and $BiFeO_3$. For example, the concentration of isopropanol (IPA) was measured with SnO_2 with a LOD of 50 ppm [42]. In this case, the gas reduces the sensing material by reacting with its oxygen anion, which reduces the sensor's resistance. Typically, these sensors need to operate at high temperature (e.g., 150 °C) and are not inherently selective. Metal catalysts like Ag with In_2O_3 for IPA sensing [43] are used to address this issue. Other semiconductors, such as III-nitride semiconductors and metal sulfides, have been studied for gas sensing [46].

Conducting polymers constitute another class of sensing materials utilized in electronic gas sensors [48]. Examples include popypyrrole (PPy), polyaniline (PANI), polythiophene (PTh) and poly(3,4-ethylenedioxythiophene) (PEDOT). The target gas can either reduce (e.g., methane (CH_4)), or oxide (e.g., carbon dioxide (CO_2)) the polymer leading to a corresponding increase or decrease in resistivity, respectively. These polymers can be combined with other materials to form conducting polymer hybrids enhancing their selectivity. Metal oxides, metals, other polymers, carbon nanotubes and graphene are potential materials for such hybrids [49].

For electrochemical cell sensors, electrolytes such as Na_2CO_3 are employed as the sensing material [50].

Similarly, magnetic gas sensor relies on mechanisms like the Kerr effect, the Hall effect, ferromagnetic resonance effect and magneto-plasmonic effect to detect gases [51]. They also used metal oxide semiconductors as the sensing material.

Another class of physical-chemical sensors is acoustic gas sensing, which includes quartz crystal microbalance (QCM) sensors [9], capacitive micromachined ultrasonic transducer (CMUT) sensors [52], microcantiliver sensors [53] and surface acoustic wave (SAW) sensors [6, 54, 55]. The sensing material is often a polymer [6, 9, 52], but it can also be lipids, chromatographic stationary materials, metal oxides and carbon nanotubes [9]. The mechanism is based on the gas absorption, which alters the mass of the sensing material. All these methods rely on the change in resonance frequency that occurs when the mass of the sensing material increases due to gas absorption.

Colorimetry relies on the color change of a material upon gas interaction [56]. This simple

method allows for visual detection of gas exposure. By incorporating a camera, continuous monitoring can be achieved. While colorimetric sensors often exhibit high selectivity and sensitivity, they suffer from limitations such as irreversibility and quantitative challenges. Nevertheless, their low power consumption makes them attractive for various applications.

Non-Absorbance Optical Gas Sensors

Sensing materials can also serve as transducers in non-absorptive optical gas sensors. Unlike optical absorption methods, the optical sensing principle does not rely on the optical properties of the analyte. These sensors can be based on long [57] and subwavelength [58] Bragg gratings, photonic crystals (PhCs) [59], surface plasmon resonance [60], perfect absorbers [61], and resonator sensors [62]. The sensing mechanism is based on the change in the optical path or the refractive index which induces a wavelength shift. This technology can be integrated onto optical fibers or photonic chips [62].

Similarly to acoustic methods, sensing materials do not require conductivity. Polymers such as polystyrene (PS) [59] and polyhexamethylene biguanide (PHMB) [63], metal-organic frameworks (MOFs) [64], metal oxides like WO_3 [65], and graphene [60] are commonly used.

Optical gas sensors offer high efficiency [66]. They require very low power to operate. As the interrogation setup and sensing device are linked by optical fibers, which exhibits minimal propagation loss, they can be separated by kilometers and integrated into optical fiber networks [67]. Combined with the reversible diffusion process of gases in polymers, there is no need to heat the sensing material, eliminating the requirement for electronic or electric power at the sensing location. This mitigates risks of fire and explosion [68]. Additionally, the sensing device is insensitive to electromagnetic perturbations.

2.2 Selectivity

Physical-chemical sensors rely on sensing materials to detect gases. The selectivity of these sensors is determined by the chemical interaction between the material and the gases present in a mixture. However, these sensors often suffer from cross-sensitivity. To address this issue, chemical engineering techniques can be employed to modify the sensing material. The three primary approaches include catalyst decoration, composite formation, and surface functionalization [69].

In catalyst decoration, the sensor's reaction rate with the gas is increased by incorporating a catalyst into the sensing material, such as using a noble metal with a metal-oxide sensor [43]. In composite formation, the gas is absorbed by the sensing material to form a composite.

Dipole-dipole interaction in conductive polymers can be tuned to target specific electron transfers, enhancing selectivity [48].

In dielectric polymers, non-conjugate interaction can be adjusted by selecting a polymer with good solubility for the target gas, aided by the Flory-Huggins theory [6]. Additionally, molecularly imprinted polymers can detect target gases based on shape and size, improving selectivity [70].

In surface functionalization, active chemicals, organometallic compounds and self-assembled monolayers can be added to the surface to increase the selectivity [69].

2.2.1 Polymers

As previously discussed, polymers are frequently employed as sensing materials due to their vast diversity, encompassing both natural and synthetic varieties. Polymers exhibit a wide range of properties, including variations in constituents, shape, chain length, and structure [71]. Moreover, polymers are readily amenable to modification and combination with other materials. For instance, non-conductive polymers can be utilized in chemiresistors by incorporating a carbon backbone [72].

Polymers can sense not only gas concentration but also other quantities such as pH [73], temperature [74], and pressure [75]. However, this sensitivity to multiple parameters can lead to cross-sensitivity, not only with other gases but also with other quantities. Consequently, significant research efforts are dedicated to mitigating this issue [60, 76–79]. This topic is further explored for cross-sensitivity with temperature in the first article presented in this thesis (Section 4), and with other gases in the second article (Section 5).

The selectivity of a polymer-based sensor is determined by the affinity between the target gas and the polymer, which is characterized by solubility. Hildebrand solubility parameter (δ_H) [80] provides an initial description of this affinity, derived from thermodynamic principles:

$$\delta_H = \sqrt{\frac{E}{V_m}} \tag{2.1}$$

where E is the energy of vaporization and V_m is the molar volume specific to the solute and solvent.

If the solubility parameter of the solute is similar to that of the solvent, the solute is more likely to dissolve. However, this theory struggles to describe solubility in polar solvents and is limited to a one-dimensional representation of solubility since it considers primarily the dispersion forces and not the dipole-dipole interactions and the hydrogen bonding.

Hansen solubility parameters, introduced by the chemist of the same name [81], added two more parameters to the original model. The Hildebrand solubility parameter includes atomic dispersion forces (δ_d). The added parameters are related to polar forces (δ_p) and hydrogen bonds (δ_h). This theory can account for polar solvents and provides a three-dimensional representation, aiding in the design of selective polymer-based chemical sensors. To calculate solubility, the ratio RED, defined as the distance between the solute and solvent in this 3D space (R_a) divided by the interaction radius of the solute (R_0), is compared to unity. The parameters of the solute and the solvent are noted by the numbers 1 and 2 respectively. R_0 is representing the radius of a sphere in the 3D space generated by the Hansen solubility parameters. If RED is less than one, the solute is likely to dissolve.

$$R_a^2 = 4\left(\delta_{d2} - \delta_{d1}\right)^2 + \left(\delta_{p2} - \delta_{p1}\right)^2 + \left(\delta_{h2} - \delta_{h1}\right)^2 \tag{2.2}$$

$$RED = \frac{R_a}{R_0} \tag{2.3}$$

Figure 2.2 illustrates the Hansen solubility model as a three-dimensional space. Commonly sensed gases, represented by black dots, and three polymers, represented by colored dots, are depicted. Unfortunately, the Hansen solubility parameters for SU-8 and PHMB, two polymers used as sensing materials in the second article (Section 5), are not available in the literature. Only PS is represented. However, all three analytes (IPA, water (H_2O), CO_2) are included in the graphic.

The selection of polymers for the sensing materials should cover a large region of the Hansen solubility parameter space, with the polymers positioned at distinct coordinates. Additionally, each target gas should have an associated polymer located nearby. Similar gases, such as isopropanol and 2-butanol in this example, will be more challenging to distinguish. Therefore, a greater number of polymers with smaller interaction radii are needed in this region of the 3D space.

Since no chemical reaction is involved, this solubility-based sensing mechanism is inherently reversible [82].

2.2.2 Sensing Array

Since most materials have cross-sensitivity, i.e., they are sensitive to more than one gas, it is necessary to use different sensing materials at the same time to deconvolute the gas mixture. Arrays of biofunctionalized Mach-Zehnder interferometers [83], polymer-coated surface-acoustic-wave sensors [6], polymer-coated CMUT-based resonant gas sensors [52],

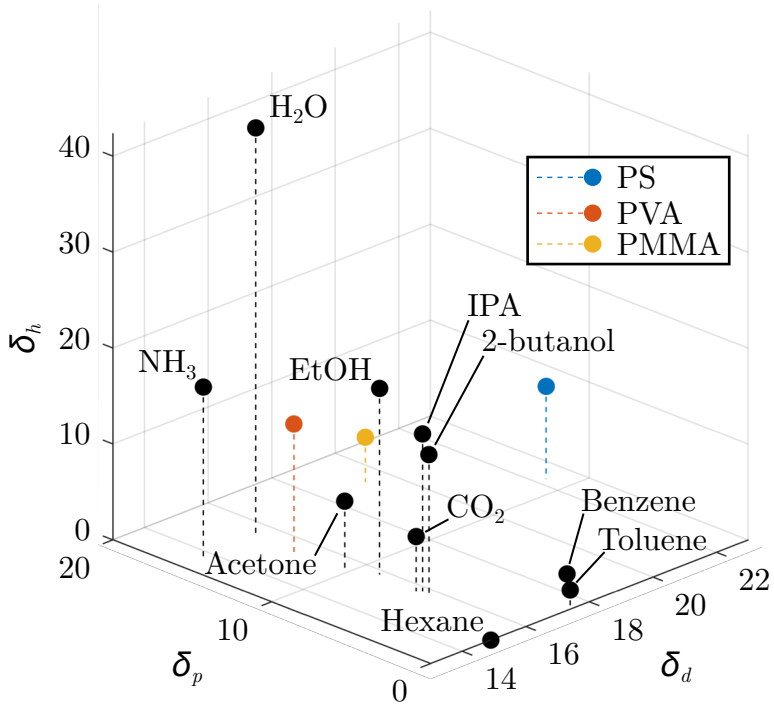

Figure 2.2 Hansen solubility model represented by a three-dimensional space with axes corresponding to dispersion (δ_d), polar (δ_p), and hydrogen-bonding (δ_h) components. The solubility is determined by the ratio between the distance between the solute and solvent in this 3D space (R_a) and the solute's interaction radius (R_0). Acetone, ammonia (NH_3), benzene, 2-butanol, carbon dioxide (CO_2), ethanol (EtOH), hexane, isopropanol (IPA), toluene and water (H_2O) are the gases (solvents) represented by black dots. Polystyrene (PS), polyvinyl alcohol (PVA) and poly(methyl methacrylate) (PMMA) are the polymers (solutes) represented by colored dots.

chromatography arrays of chemoresponsive colorants [84] and conducting polymer sensors [85] have been demonstrated.

On-chip optical resonators have been functionalized with various polymers [20, 21]. By employing an array of functionalized resonators, it has been demonstrated that two gases could be selectively measured [22].

Sensing arrays with cross-sensitivity can make data interpretation and gas concentration determination challenging. When cross-sensitivity is linear and independent, matrix inversion [22] and principal component analysis (PCA) [8, 86] can be employed. For more complex systems, machine learning techniques are more appropriate [87].

2.2.3 Summary

Numerous methods exist for gas detection and concentration measurement, each with its own advantages and disadvantages [30, 31, 46, 88, 89]. The ideal gas sensor does not exist, and the choice of technology depends on specific application requirements. While separation methods offer superior performance, they are costly and challenging to miniaturize. Physical methods, while sensitive and low-cost, cannot distinguish between gases within a mixture. Absorption optical sensors, on the other hand, are selective, sensitive, and environmentally robust. However, they are complex, expensive and difficult to miniaturize.

On the other hand, physical-chemical sensors offer advantages such as low cost, portability, and rapid response times. However, they often suffer from environmental sensitivity, the need for calibration and poor selectivity. The latter issue can be mitigated by employing arrays of different sensing materials.

Compared to semiconductor gas sensors, polymer-based gas sensors stand out for their low energy consumption and reduced risk of fire and explosion due to their ability to operate at room temperature. Additionally, the vast array of polymers offers significant potential for tailoring sensor properties.

Non-absorptive optical gas sensors are particularly noteworthy for their high sensitivity to changes in the properties of the sensing material.

2.3 Optical Resonators

2.3.1 Overview

Optical resonators are structures that confine light. The first discovered optical resonator, the Fabry-Perot interferometer (FPI) [90], traps light between two facing mirrors. Other types of resonators include PhC, optical fiber rings, microrings, and WGM resonators.

These resonators are characterized by their quality factor, finesse, and mode volume. Resonators find applications in telecommunications for add-drop [91] and filtering [92], as well as in sensing [93]. For example, temperature [74] and pressure [75] have been measured using polymer-functionalized FPI resonators. In gas sensing, concentrations of volatile organic compounds (VOCs) such as isopropanol, acetone, and toluene have been measured using a polymer-functionalized fiber-optic FPI based on the swelling behavior of polydimethylsiloxane (PDMS) [93]. The advantage of resonator sensors lies in their ability to increase light-matter interaction with the sensing material, enabling the detection of small changes in the material's properties such as its volume and refractive index.

2.3.2 Whispering Gallery Mode Resonators

Whispering gallery mode (WGM) resonators were first discovered in acoustics to explain how sound travels within St. Paul's Cathedral [94]. The equations governing acoustics are similar to those of optics, allowing for analogous phenomena in microphotonics. Due to the shorter wavelength of light compared to sound, the optical resonance structures operate on the micrometer scale rather than the meter scale. In axisymmetric dielectric structures, light travels along the edge and resonates. Optical WGM resonators encompass microdisk, microtorus, microbubble, microbottle, and microsphere resonators [95]. Table 2.1 provides the quality factor of various WGM resonators with microspheres exhibiting the highest quality factor.

Table 2.1 Comparison of quality factors for various whispering gallery mode resonator geometries

Resonator type	Quality factor	Source
Microbubble	1.0×10^6	[96]
Microdisk	2.4×10^7	[97]
Microbottle	1.0×10^8	[98]
Microtorus	1.5×10^8	[99]
Microring	4.2×10^8	[100]
Wedge microdisk	1.1×10^9	[101]
Microsphere	3.0×10^{11}	[102]

The sensitivity of WGM resonators to changes in refractive index has been demonstrated using PS microspheres [103]. By tracking the wavelength shifts of higher-order modes with distinct spatial distributions, researchers studied the radial distribution and evolution of the refractive index during the glass transition which is the transition between a hard and rubbery state of an amorphous material at the glass-transition temperature. Additionally, an Al_2O_3:Yb_3^+ integrated microdisk laser has been employed as a label-free biosensor [104]. Other sensing applications include refractive index sensing [105], nanoparticle detection [106], biosensing [107], magnetic field sensing [108] and pressure sensing [109]. Furthermore, simultaneous measurement of refractive index and temperature has been achieved using a microring resonator by exploiting polarization-dependent effects [110].

2.3.3 WGM Resonator Gas Sensors

Functionalized WGM resonators can serve for gas sensing. Various resonator geometries have been investigated, including microbubbles [111], microbottles [62, 112–115], microtubes [86, 116], microdisks [23, 24, 117], microtoroids [118, 119] and microspheres [120]. The quality factors (Q-factors) of these resonators range from 1×10^3 to 2×10^6. Table 2.2 summarizes the WGM resonator gas sensors discussed in this section.

The sensing material is often a polymer. The resonator can be fabricated entirely from the polymer [23, 24, 117] or simply coated with it [62, 111, 112, 115, 118]. To enhance selectivity and sensitivity, the polymer can be combined with other sensing materials such as metal [86], metal-catalyzed metal-oxide [114] or graphene [113, 119]. MOFs (e.g., ZIF-8) [116] and silica gel [120] have also been explored as sensing materials.

Most WGM resonator sensors are not fully integrated. Microbubbles, microtubes, and microspheres are challenging to integrate and require either a fragile tapered optical fiber for coupling [62, 86, 111–115, 120] or a complex photoluminescence setup [116]. While disk and microtoroid resonators are chip-based, some still require a tapered optical fiber [24, 118, 119] or a photoluminescence setup [117]. Among the presented sensors, only one is fully integrated [23]. However, as this sensor comprises a polymer disk on a substrate, radial expansion of the polymer is limited, restricting its sensitivity to refractive index changes.

Sensitivities and LODs are difficult to compare across different gases, as the saturated partial pressure significantly influences sensitivity [24]. Nonetheless, very low LODs in the parts-per-trillion (ppt) range have been achieved [119]. WGM resonator sensors can detect and quantify a wide range of target gases over various concentration levels.

Most of these sensors rely solely on the total wavelength shift to measure concentration. However, some studies have utilized Langmuir's adsorption theory, measuring the rate of wavelength shift instead [118, 119].

All of these sensors exhibit limited selectivity. WGM resonators are often multimodal, a characteristic that can be exploited to distinguish different analytes by studying molecular diffusion dynamics within the polymer [121], similar to the refractive index studies of a polystyrene (PS) microcavity [103]. Additionally, the differing sensitivities of different modes to various gases can be leveraged to measure gas mixtures [122]. However, these approaches are limited by the number of measurable variables. Sensing arrays offer a more promising solution, but require fully integrated WGM resonators on a single optical chip fabricated from different polymers.

Table 2.2 Comparison of whispering gallery mode resonator gas sensors of different resonator types and sensing materials

Resonator type	Sensing material	Analyte	Diameter (µm)	LOD (ppm)	Range (ppm)	Sensitivity (pm/ppm)	Response time (s)	Q-factor	Integration	Source
Polymer-coated glass microbubble	PHMB	CO_2	320	5.0×10^1	7.0E+02	4.6E-01	140	7.3E+04	Off-chip, tapered fiber	[111]
Polymer-coated glass microbottle	PDMS	Ethanol	254	4.2	2.7E+02	3.6E+01		2.2E+04	Off-chip, tapered fiber	[62]
Polymer-coated glass microbottle	PVA	Acetone	332	3.2	1.6E+02	-6.3E+00	480		Off-chip, tapered fiber	[112]
Polymer-coated glass microbottle	Pd-WO_3 PDMS	H_2	250	1.0×10^3	3.0E+04	-3.1E-01			Off-chip, tapered fiber	[114]
Coated glass microbottle	Graphene	NH_3*, acetone, H_2O, EtOH, p-xylene, H_2	119	1.0	4.0E+02	1.6E-04	30	2.0E+06	Off-chip, tapered fiber	[113]
Polymer-coated glass microtube	Pd coated PDMS	H_2	135	6.0×10^1	7.5E+03	1.4E-02	858	5.1E+04	Off-chip, tapered fiber	[86]
Coated glass microtube	ZIF-8	CO_2	23	1.5×10^4	1.0E+06	7.4E-04	60		Photoluminescence	[116]
Suspended polymer microdisk	PEG-DA hydrogel	H_2O	20		1.6E+4	1.7E-01		2.8E+03	On-chip, photoluminescence	[117]
Suspended polymer microdisk	SU-8	Toluene, 1-butanol, H_2O, limonene, IPA, valeric acid*	100	6.0×10^{-1}	2.3E+01	2.3E+01	14	1.5E+04	On-chip, tapered fiber	[24]
Polymer microdisk	SU-8	H_2O	200	7.4	1.7E+03	4.4E-01	80	1.0E+03	On-chip, integrated	[23]
Coated glass microsphere	Silica gel	NH_3	282	2.5×10^{-4}	3.0E+01	8.0E+02	1.5	2.6E+05	Off-chip, tapered fiber	[120]

2.4 Additive Fabrication Techniques

2.4.1 Overview

Additive manufacturing involves the controlled addition of materials to create complex structures. Despite lower resolution, additive fabrication techniques have been integrated into traditional microfabrication processes [123]. These techniques have found applications in diverse fields, ranging from aerospace [124] to medicine [125]. Extensive research has been conducted on their use in flexible electronics [126].

These fabrication techniques can be categorized into two primary groups: non-contact and contact printing. Non-contact printing techniques include inkjet printing, aerosol jet printing, selective laser melting (SLM), fused deposition modeling (FDM), stereolithography (SLA), dip pen nanolithography (DPN), electrohydrodynamic (EHD) jet printing, and direct laser writing (DLW) [127, 128]. Contact printing techniques encompass flatbed screen printing, rotary screen printing, gravure printing, and flexographic printing [127]. Non-contact printing techniques offer advantages in terms of rapid prototyping and reduced ink consumption [127].

An ink typically comprises a pigment, a binder, a solvent, and optional additives [127]. For gas sensing applications, the pigment, the functional material, can be in the form of nanoparticles [129, 130] or polymers [131]. Additives, such as ethylene glycol and Triton X-100, can be included to prevent clogging during inkjet printing by modifying the viscosity and surface tension of the ink [132].

Printed gas sensors, such as capacitive [133] and chemiresistive [134, 135] devices, have been fabricated. Various materials, including metal oxides (e.g., TiO_2) fabricated by screen printing and polymers (e.g., PANI) fabricated by gravure printing, have been employed [135]. These methods are well-suited for integrating different materials onto a single substrate, a crucial requirement for sensor arrays to enhance selectivity [127].

Not all additive fabrication techniques are capable of producing optical-quality devices. Among the techniques discussed, SLM, FDM, and SLA have been used to fabricate optical devices, but their quality without additional post-processing steps is limited by low surface quality, inhomogeneity, and low resolution [128]. In contrast, two-photon polymerization (2PP), a DLW fabrication process, offers nanometer-scale resolution [136], enabling the fabrication of lenses [137]. 2PP has also been used to fabricate multiple suspended polymer micro-rings on a multicore fiber for vapor sensing [138]. Additionally, a polyethylene glycol (PEG) suspended disk has been fabricated for humidity sensing [117]. Other nanoscale techniques, such as DPN, EHD jet printing, and other direct laser writing DLW techniques, have been successfully employed to fabricate optical devices. However, there is a trade-off

between voxel size, which influences optical performance, and fabrication time and cost [128].

Inkjet printing distinguishes itself by its ability to fabricate optical-quality devices using polymers that are not necessarily UV-curable, expanding the range of available materials. The surface quality achieved is comparable to injection molding, with roughness values as low as 10 nm [139]. By leveraging surface tension during drying, smooth surfaces can be created on polymer structures, enabling the fabrication of high-quality factor resonators [25]. Finally, inkjet printing offers higher printing speeds compared to nanometer-scale additive fabrication techniques. While contact printing can achieve high throughput and even roll-to-roll processing, it often lack the precision and optical quality offered by inkjet printing.

2.4.2 Inkjet Printing

Inkjet printing is an additive technique that involves precisely depositing ink onto a substrate by printing individual tiny droplets in a pattern [140]. It is the most widely used technique in consumer paper printers. This technique has applications ranging from wearable electronic devices [126] to tissue engineering with biomaterials [141].

Two primary inkjet printing technologies exist: continuous inkjet (CIJ) and drop-on-demand (DOD). In CIJ, a continuous flow of ink is deflected onto or off the substrate. In DOD, droplets are ejected by impulses, with volumes as low as a picoliter [142]. Figure 2.3 a) illustrates a DOD inkjet system with a piezoelectric actuator. DOD inkjet printer heads can also employ thermal actuators. Initially, ink is pushed into the printer head, and back pressure is maintained to prevent ink slippage without actuation. Droplets are ejected one by one by the actuator, and land on the substrate, where the solvent evaporates.

Research has been conducted on the printing stability of inkjet printing parameters [143,144]. To describe the stable printing region in parameter space [145], dimensionless fluid dynamic quantities are introduced. The Reynolds number Re represents the ratio of inertial to viscous forces, while the Weber number We represents the ratio of inertial pressure to surface tension. These quantities depend on both fluid properties and printing characteristics. To isolate the printability of an ink, the number Z which is the inverse of the Ohnesorge number Oh is more appropriate, as it is independent of the droplet velocity:

$$Re = \frac{\rho v d}{\mu} \tag{2.4}$$

$$We = \frac{\rho v^2 d}{\gamma} \tag{2.5}$$

$$Z = \frac{1}{Oh} = \frac{Re}{\sqrt{We}} \tag{2.6}$$

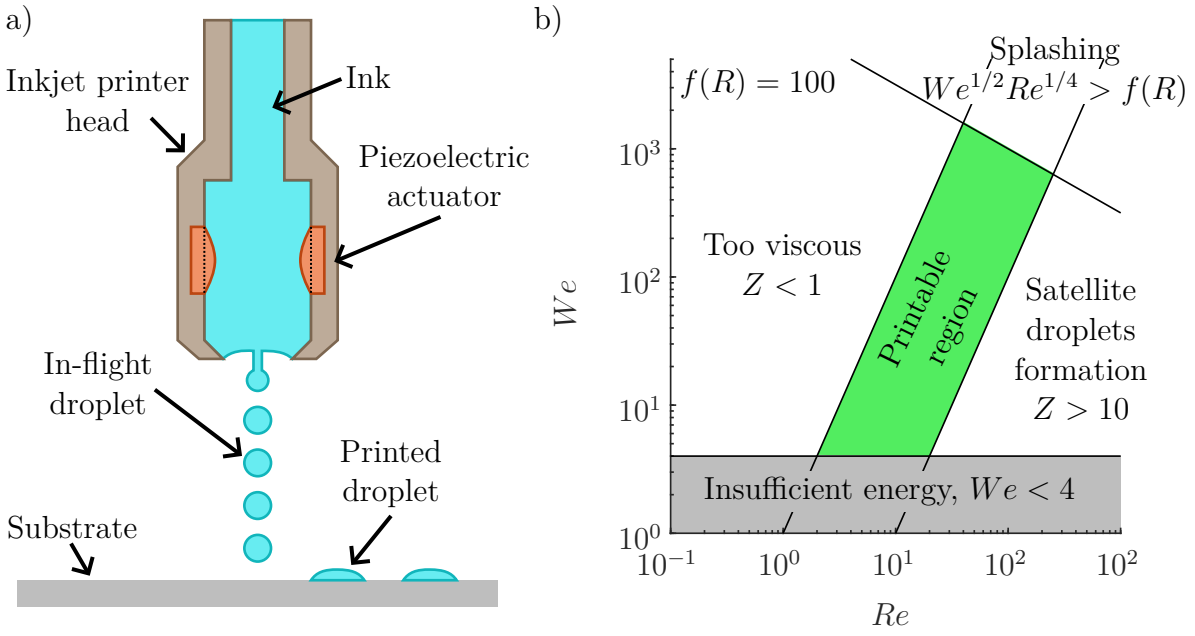

Figure 2.3 a) Schematic diagram showing drop-on-demand inkjet printing in operation with piezoelectric actuation. b) Parameter space of the Reynolds number Re and Weber number We defining the printable region colored in green.

where ρ is the density, v is the ink velocity, μ is the viscosity, γ is the surface tension, and d is the characteristic length, typically the nozzle diameter. The droplet diameter is approximately equal to this value.

A printable ink should have a Z number between 1 and 10. If the Z number is below 1, the ink is too viscous. If it is above 10, satellite droplet formation occurs. Additionally, there are other printing boundaries: sufficient energy to eject the droplet ($We > 4$) and excessive energy that causes splashing ($We^{1/2}Re^{1/4} > f(R)$) where $f(R)$ is a function of the substrate's surface roughness (R). Figure 2.3 b) illustrates the printable region, colored in green, in the Reynolds-Weber number parameter space. This region is bounded by the limits imposed by various printing conditions.

Another factor to consider when using inkjet printing is the temperature of the substrate [146]. Substrate temperature influences the evaporation rate of the ink's solvent. At high evaporation rates, the Marangoni effect induces a flux of solid matter from the center to the edge of the droplet, similar to the "tears of wine" phenomenon. This effect leads to the formation of a coffee-ring-like deposit with more material at the edge than in the middle.

Materials printed by inkjet printing include perovskite [147, 148], diamond [149], nanoparticles [150] and ceramics [151]. Polymers such as PEG [152–154], PDMS [155, 156], SU-

8 [157] and poly(vinyl alcohol) [158] can also be printed. These polymers may be UV-curable [152–154, 157] or non-curable [155, 156, 158]. At high polymer concentrations, polymer chains begin to interact, leading to increased viscosity and limiting printability [159,160]. This effect is exacerbated by high-molecular-weight polymers, which exhibit non-Newtonian behavior [161]. Hence, modeling the behavior of polymer inks in inkjet printing has been investigated [162].

Inkjet Printing for Gas Sensing

Additive fabrication techniques offer a clear advantage in fabricating sensor arrays for gas sensing. Multiple materials can be easily integrated onto a single device, resulting in compact, selective, and versatile sensors [127]. Inkjet printing has been used to fabricate chemiresistive gas sensor arrays [70]. The inks used to fabricate these sensors contained molecularly imprinted polymers as the sensing material. Another example of inkjet-printed chemiresistive gas sensor arrays involves inks composed of polystyrene, a carbon backbone, and PGMEA solvent, which were deposited onto electrodes [72]. The sensitivities of these sensors to ethanol and acetone were investigated.

Inkjet Printing of Optical Devices

Inkjet printing has been used to fabricate various optical devices [128] including passive components like lenses [163] or active components like light-emitting diodes [164], optoelectronic devices [147] and lasers [148].

WGM resonators have also been fabricated using inkjet printing, including deformable microdroplet cavities [165] and microdisk cavities [166]. High-quality factor resonators, necessary for low-threshold lasing, have been demonstrated using inkjet-printed active polymer blends [25–27]. These inkjet-printed microdisk lasers were used to control the non-specific absorption of biomolecules [28].

2.5 Optical Vertical Integration

Whispering gallery mode sensors can be integrated on chip in different ways to facilitate the packaging, the robustness and the compactness of the sensing device comprised of many polymer resonators. Beyond tapered optical fiber coupling, alternative coupling techniques include free-space coupling, where the resonator is aligned with a focused laser beam, prism coupling, which utilizes a prism to couple light into and out of the resonator, and bent optical fiber coupling, where a small fiber loop is positioned near the resonator's edge (Figure 2.4).

For off-chip whispering gallery mode resonators, additional methods such as angle-polished fiber, no-core fiber, and in-fiber coupling have been explored [167, 168].

The coupling methods compatible with on-chip resonators generally require precise alignment of delicate structures and optics, thereby increasing the complexity, fabrication time, and cost of the manufacturing process.

Photoluminescence can be employed to interrogate whispering gallery mode resonators by incorporating fluorescent molecules within the cavity. Excitation of these molecules with light at a specific wavelength leads to the excitation of resonance modes, which can be probed using an objective [25, 28]. However, this approach also necessitates a complex optical setup.

To achieve the goal of a compact and practical sensor, on-chip coupling is essential. Photonic integrated circuits (PICs) offer advantages in terms of parallel fabrication, reduced manufacturing costs, and robustness. Inkjet printing has been employed to draw polymeric optical waveguides [169, 170]. While underetching and suspended resonators are desirable for optimal performance, they are incompatible with in-plane waveguides. The wedge shape of the inkjet-printed resonators, coupled with the fabrication process, limits horizontal coupling. The wedge edge pushes the optical mode towards the center, leading to inefficient coupling. For instance, with tapered optical fibers, coupling was achieved by positioning the fiber either above or below the resonator to ensure an optimal light transfer. Recent work demonstrated vertical on-chip coupling between inkjet-printed polymer resonators and SU-8 waveguides [171]. However, the resonator in that study was not suspended.

In recent years, PICs have evolved towards multi-layer configurations, mirroring the structure of its electronic counterpart. PICs enable low-cost, high-yield, and robust manufacturing processes of optical system on a chip [172]. To enhance the capabilities of these systems, hybrid integration is crucial. This approach allows the integration of active materials onto silicon waveguides to create lasers, photodetectors, and modulators [173]. Beyond silicon-on-insulator platforms, other platforms such as silicon nitride are being explored [174].

As circuits become increasingly complex, hybrid integration and multilayer platforms are necessary. In electronics, transistors are interconnected by complex copper circuits. To accommodate non-planar circuit designs, multiple layers of copper wires are connected using copper vias. Similarly, in photonics, layers of photonic waveguides are coupled together using evanescent coupling [175, 176], which minimizes crosstalk at junctions [177]. A common approach involves superimposed tapered waveguides on both layers to facilitate adiabatic coupling.

This technology has been used to integrate wedge-shaped disk resonators [178–181]. In this

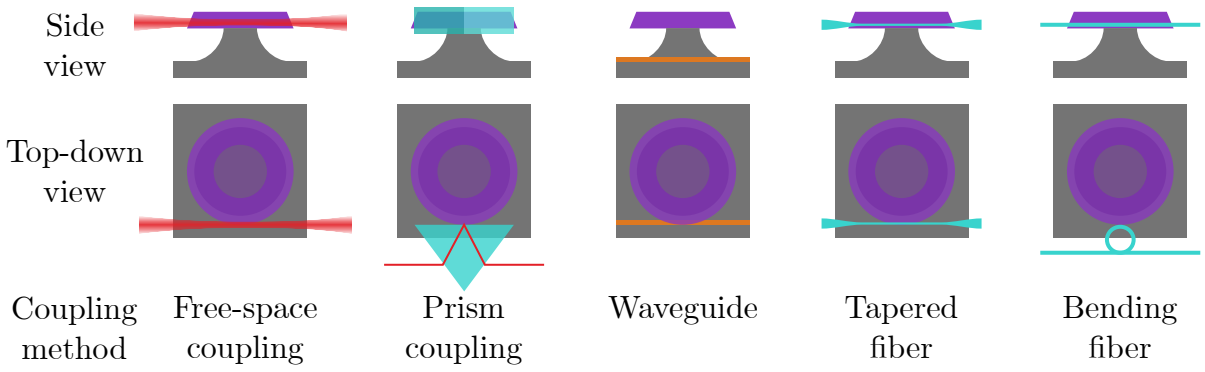

Figure 2.4 Illustration of a side and top-down view of optical coupling methods with a suspended polymer wedge resonator on a chip.

example, the photonic platform is composed of a silicon nitride waveguide with a silicon dioxide cladding. The whispering gallery mode resonators were either disk-shaped or wedge-shaped and, both suspended and attached to the substrate. These resonators were fabricated from silicon oxynitride. Due to the wedge shape, optical modes are pushed towards the center, making horizontal coupling challenging. As a result, the resonator is better coupled to a waveguide that is placed beneath the optical mode. Notably, this approach allows the resonator to be suspended. This method has also been employed to vertically coupled wedge-shaped disk resonators together, forming a coupled-resonator optical waveguide [182].

The advantages of this approach in sensing have been demonstrated with an integrated silicon oxy-nitride wedge disk for refractive index sensing [183]. The resonator was fully encapsulated within a fluidic channel, which would be challenging to achieve with a tapered optical fiber.

2.6 Synthesis

The literature review explored gas sensing methods, optical resonators, additive fabrication techniques, and vertical integration. A particular focus was given on non-absorptive optical gas sensing, physical-chemical gas sensors based on polymers, WGM resonators, and inkjet printing. These concepts form the foundation of the proposed gas sensing platform of this thesis.

To recapitulate the advantages of the chosen technologies, physical-chemical sensing is selected for its low cost, potential selectivity, and portability. More specifically, optical sensing offers the ability to measure minute changes in material properties with low power consumption and enables network integration. Polymer-based sensing materials are selected for their

versatility. Therefore, a disk-shaped WGM resonator fabricated from polymeric materials can serve as a transducer, converting gas concentration into an optical signal. To enhance selectivity, an array of different polymer-based resonators is necessary. Inkjet printing, combined with PIC technology and vertical coupling, is well-suited for integrating diverse polymers onto a single optical chip. Finally, by suspending these polymeric disks, both refractive index and volume changes can contribute to the sensing signal.

CHAPTER 3 THEORY ON WHISPERING GALLERY MODE GAS SENSORS

At the interface between two media with refractive indices n_1 and n_0, where $n_0 < n_1$, total internal reflection occurs when a light ray incident from the medium with refractive index n_1 strikes the interface at an angle greater than the critical angle, as depicted in Fig. 3.1. This is a consequence of the Snell-Descarte law.

$$\theta_i < \cos^{-1}\left(\frac{n_1}{n_0}\right) \tag{3.1}$$

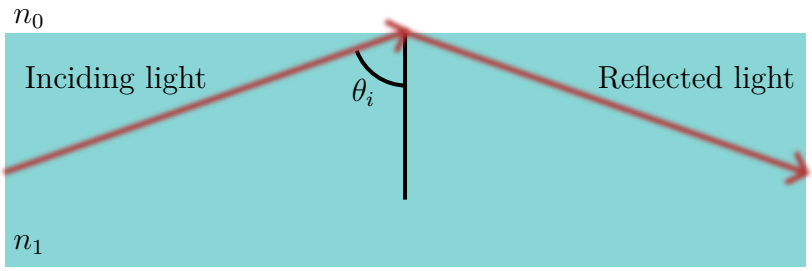

Figure 3.1 Total internal reflection of a light ray at the interface between two mediums ($n_1 > n_0$).

Waveguides are dielectric structures that utilize total internal reflection to confine light. A waveguide consists of a core with a higher refractive index surrounded by a cladding with a lower refractive index. When the core's dimensions approach the wavelength of light, a wave-based approach, rather than a geometric one, becomes necessary. By assuming a scalar, monochromatic, planar, and linearly polarized electromagnetic field (TEM), an optical wave with amplitude Ψ and wavelength λ can be described by the time-independent form of the wave equation, known as the Helmholtz equation:

$$\left(\nabla^2 + k_0^2 n^2\right)\Psi = 0, \tag{3.2}$$

where $k_0 = 2\pi/\lambda$ is the wave number. ∇^2 is the Laplacian operator and n is the refractive index distribution. This equation applies to both the transverse electric (TE) and the transverse magnetic (TM) modes.

A rectangular disk, as depicted in Fig. 3.2, is a whispering gallery mode resonator similar to those investigated in this thesis. Its simple geometry allows for a separation of the problem into two distinct structures within the cylindrical coordinate system: a 2D whispering gallery mode disk, $R(r, \phi)$, and a slab waveguide, $Z(z)$, also referred to as a planar waveguide.

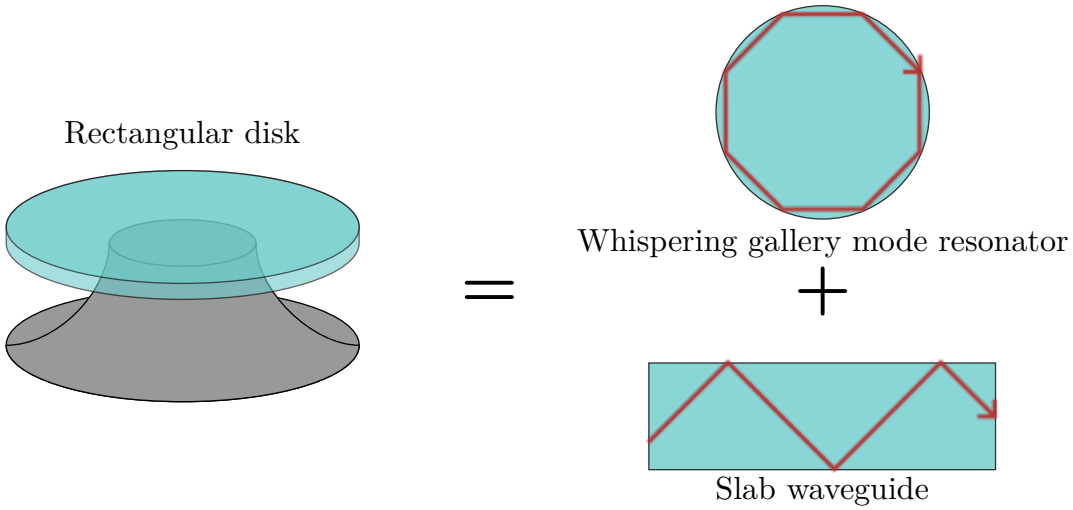

Figure 3.2 A rectangular disk is decomposed in between a 2D whispering gallery mode resonator and a slab waveguide.

3.1 Slab waveguides

A slab waveguide, as shown in Figure 3.3, has a core with a refractive index n_1 bounded between two cladding layers with a refractive index n_0 above and below [184]. The waveguide has a finite thickness, h, in the x direction but is infinite in the y direction. Light propagates along the z axis, and the Helmholtz equation simplifies to a one-dimensional equation in the x direction.

Modal parameters U and W and waveguide parameter V are defined as follows:

$$U = \frac{h}{2}\sqrt{k_0^2 n_1^2 - \beta^2} \tag{3.3}$$

$$W = \frac{h}{2}\sqrt{\beta^2 - k_0^2 n_0^2} \tag{3.4}$$

$$V = \sqrt{U^2 + W^2} = \frac{k_0 h}{2}\sqrt{n_1^2 - n_0^2}, \tag{3.5}$$

where β is the propagation constant. The V number depends only on the waveguide parameters. However, U and W numbers need to be solved.

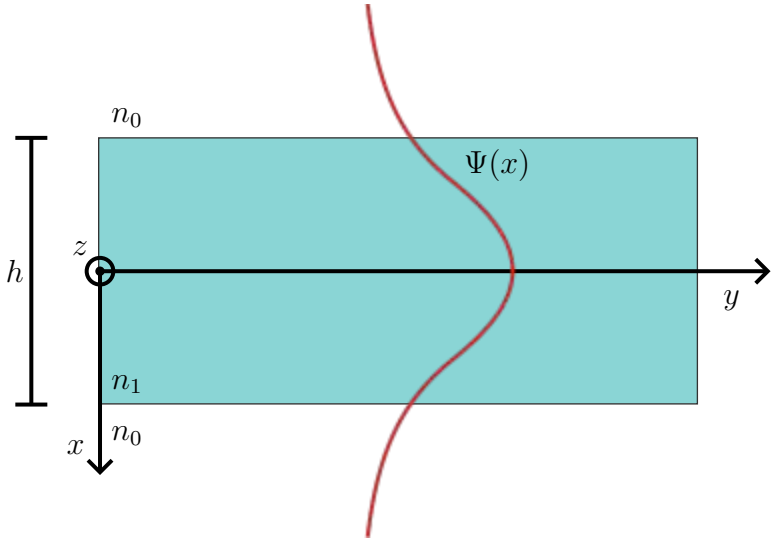

Figure 3.3 Slab waveguide of height h and an example of an optical mode amplitude $\Psi(x)$

The solution of the Helmholtz equation for this structure is the optical amplitude $\Psi(x)$. The amplitude is for the y-component of the electric field E_y for the TE polarization and the y component of the magnetic field H_y for the TM polarization. It has two forms depending on the mode number.

For the even solutions:

$$\Psi(x) = \begin{cases} \frac{\cos(2Ux/h)}{\cos U}, & |x| < h/2 \\ \frac{\exp(2W|x|/h)}{\exp -W}, & |x| > h/2 \end{cases}. \tag{3.6}$$

For the odd solutions:

$$\Psi(x) = \begin{cases} \frac{\sin(2Ux/h)}{\sin U}, & |x| < h/2 \\ \frac{x}{|x|}\frac{\exp(2W|x|/h)}{\exp -W}, & |x| > h/2 \end{cases}. \tag{3.7}$$

Since the tangential component of the electric field and its derivative must be continued at the interfaces between the core and the cladding, transcendental equations must be solved that depend on the polarization.

For TE polarization:

$$\tan U = \frac{W}{U} \quad \text{Even modes} \tag{3.8}$$

$$\tan U = -\frac{U}{W} \quad \text{Odd modes} \tag{3.9}$$

For the TM polarization:

$$\tan U = \frac{n_1^2}{n_0^2}\frac{W}{U} \quad \text{Even modes} \tag{3.10}$$

$$\tan U = -\frac{n_0^2}{n_1^2}\frac{U}{W} \quad \text{Odd modes} \tag{3.11}$$

The solutions to these equations are presented in Fig. 3.4 a) as a function of the waveguide parameter which only depends on the height, the wavelength and the refractive indices of the core and the cladding. The solution is given for the modal parameters U from which W can be calculated as well. For both polarization, the first five modes are shown represented by U_p where p is the mode number. The number of possible optical modes supported by the waveguide depends on the parameter V. Below $V = \pi/2$, only the fundamental mode is possible (U_0). A new mode is added at each $V = k\pi/2, k = 0, 1, 2, ...$ with a modal parameter U equal to V.

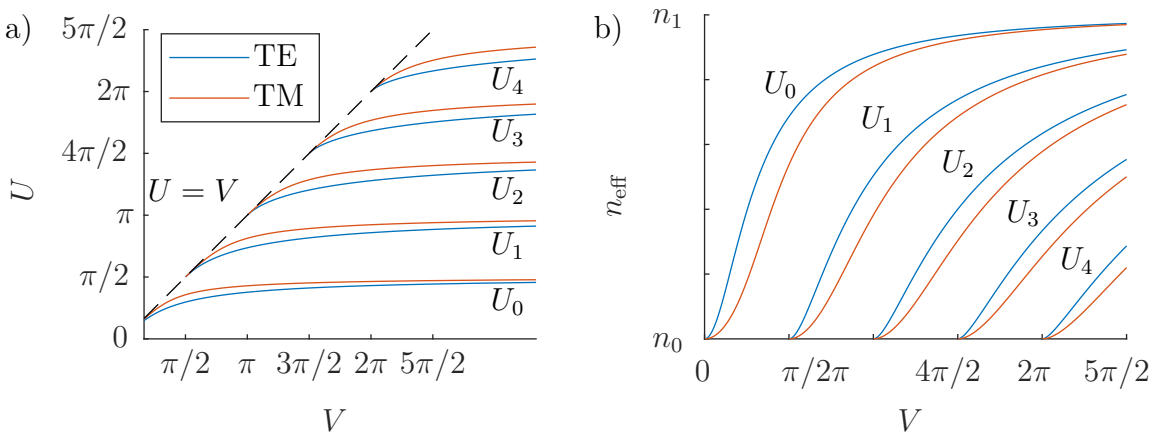

Figure 3.4 a) First five modal solutions U_p of the transcendental equations for the slab waveguide for both polarization TE and TM shown as modal parameter U as a function of waveguide parameter V. b) Corresponding refractive index.

From this, we can extract a maximal slab height h_c to have a mono-modal waveguide which depends on the wavelength and the refractive indices of the core and the cladding:

$$h_c = \frac{\lambda}{2\sqrt{n_1^2 - n_0^2}}. \tag{3.12}$$

Another important waveguide parameter is the effective refractive index of the optical modes

which is related to the phase constant $\beta = n_{\text{eff}} 2\pi/\lambda$. It is calculated with:

$$n_{\text{eff}} = n_1 \sqrt{1 - 2\Delta \left(\frac{U^2}{V^2}\right)}, \tag{3.13}$$

$$\Delta = \frac{n_1^2 - n_0^2}{2n_1^2}. \tag{3.14}$$

Figure 3.4 b) shows the effective refractive index of the first five optical modes for both TE and TM polarization as a function of the waveguide parameter V. It is always between the refractive indices of the core and the cladding. When the optical mode starts to exist at low V numbers, the effective refractive index is close to the cladding one. At large V numbers, it tends to the refractive index of the core.

3.2 Whispering Gallery Mode Resonators

An optical resonator is a structure that confines light to a closed loop. After a single round trip, the light interferes with itself. The resonant wavelengths, λ_m, are those that exhibit constructive interference. These resonant modes correspond to integer multiples, $m = 1, 2, ...$, of the optical path length (OPL) for a complete round trip. In a whispering gallery mode resonator of radius R, the OPL is equal to the circumference of the circular structure, multiplied by the refractive index, n:

$$m\lambda_m = \text{OPL} \tag{3.15}$$

$$= 2\pi Rn \tag{3.16}$$

The free spectral range λ_{FSR} is the wavelength separation between two adjacent optical modes:

$$\lambda_{\text{FSR}} = \frac{\lambda^2}{2\pi Rn}. \tag{3.17}$$

A typical transmission spectrum of a whispering gallery mode resonator, as shown in Figure 3.5, exhibits a series of peaks corresponding to individual optical modes, m, separated by the free spectral range (λ_{FSR}). In the absence of loss, these peaks would be infinitely narrow. However, due to unavoidable losses, the peaks are broadened to a full width at half maximum (FWHM) of $\delta\lambda$.

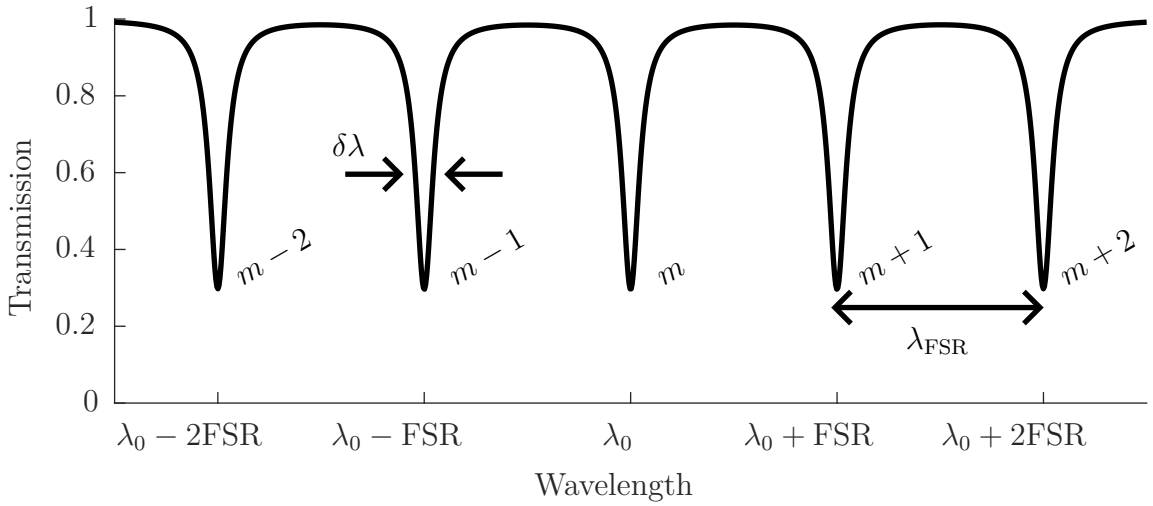

Figure 3.5 Theoretical transmission spectrum of a whispering gallery mode resonator.

3.2.1 Optical Loss

A resonator is characterized by its quality factor Q which is a proportional to the stored energy divided by the energy loss per cycle. It is also related to the photon lifetime in the cavity τ_p and the linear loss α_r:

$$Q = 2\pi \frac{c_0}{\lambda} \tau_p \tag{3.18}$$

$$= \frac{2\pi}{\lambda \alpha_r} \tag{3.19}$$

$$\tag{3.20}$$

where c_0 is the speed of light in vacuum.

Optical loss is inevitable due to many factors. The different contributions for the intrinsic quality factor Q_{int} are the radiation Q_{rad}, the surface scattering Q_{ss}, the surface absorption Q_{sa}, the volume scattering Q_{vs} and the volume absorption Q_{va} [185].

$$\frac{1}{Q_{\mathrm{int}}} = \frac{1}{Q_{\mathrm{rad}}} + \frac{1}{Q_{\mathrm{ss}}} + \frac{1}{Q_{\mathrm{sa}}} + \frac{1}{Q_{\mathrm{vs}}} + \frac{1}{Q_{\mathrm{va}}} \tag{3.21}$$

The quality factor is related to the full width at half-maximum $\delta\lambda$ with [95]:

$$Q = \frac{\lambda_0}{\delta\lambda}. \tag{3.22}$$

Optical resonator are also characterized by their finesse which is defined by:

$$\mathcal{F} = \frac{\pi e^{-\pi\alpha_r nR}}{1 - e^{-\pi\alpha_r nR}} \tag{3.23}$$

When the finesse is large ($\mathcal{F} >> 1$), it can be approximated with:

$$\mathcal{F} = \frac{\lambda_{\text{FSR}}}{\delta\lambda}. \tag{3.24}$$

3.2.2 Solutions to the Whispering Gallery Mode Resonator

The 2D whispering gallery mode resonator problem can be separated between the radial and the azimuth part. The solution of the latter is a complex exponential function with a mode number m:

$$\Psi_m(\theta) = e^{\pm im\theta}. \tag{3.25}$$

The solution of the radial problem is one of the Bessel's function:

$$\Psi_m(r) = \begin{cases} A_m J_m\left(k_1 r\right) & r < R \\ B_m H_m^{(1)}\left(k_2 r\right) & r > R \end{cases} \tag{3.26}$$

where R is the radius of the resonator.

Since the electric field and its derivative needs to be continuous, transcendental equations need to be solved for k_i:

$$\frac{J'(k_1 R)}{k_1 J_m(k_1 R)} = \frac{H'^{(1)}(k_2 R)}{k_2 H_m^{(1)}(k_2 R)} \quad \text{TE}, \tag{3.27}$$

$$\frac{k_1 J'(k_1 R)}{J_m(k_1 R)} = \frac{k_2 H'^{(1)}(k_2 R)}{H_m^{(1)}(k_2 R)} \quad \text{TM}. \tag{3.28}$$

Figure 3.6 illustrates solutions of these equations for both polarizations where each blue dot is a solution. They are classified by two mode numbers. For a particular azimuthal mode number m, multiple radial solutions can be found at different resonance wavelengths which are classified with the radial mode number l [186]. This is illustrated by the orange dashed lines that link different radial mode of the same azimuth mode. The y-axis represents the finesse which is due only to radiation loss, and is calculated from the imaginary part of the solution. Low finesse is achieved for small resonators compared to the resonance wavelength, and thus, smaller azimuthal mode number m, and higher radial mode number.

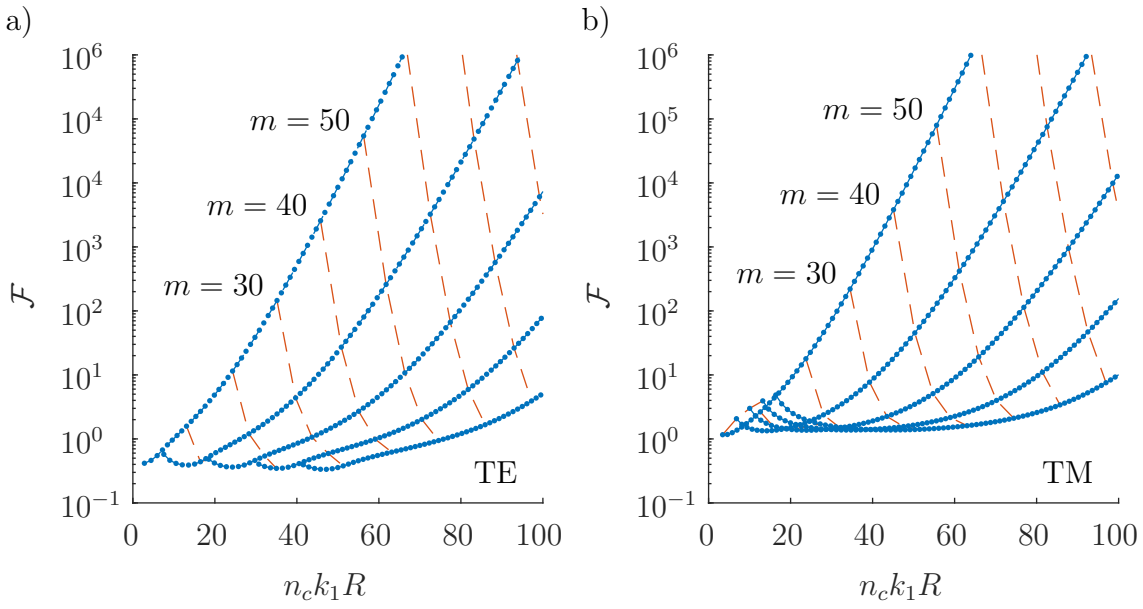

Figure 3.6 Solutions to the transcendental equations of the whispering gallery mode resonator for both polarization (TE and TM). Each solution is a blue dot.

The radial amplitudes of solutions to the whispering gallery mode (WGM) resonators are given in Fig. 3.7 for the first three radial modes of each polarization of the azimuthal mode 10 with a refractive index ratio of 2. When the radial mode number is increased, more oscillations are presented inside and outside the resonator. The latter cause the radiating loss.

Figure 3.8 shows the 2D representation of the whispering gallery mode ($m = 10$, TE1, $n_1/n_0 = 2$). The black circle represents the disk boundary of radius R. The phase velocity is dependent on the radius inside the disk, and constant outside, which cause a spiral pattern.

Arbitrary Axis-Symmetric Optical Resonator

While analytical solutions can be obtained for rectangular resonators by combining slab waveguide and WGM solutions, axis-symmetric resonators with arbitrary shapes require numerical methods for their vector optical modes. This thesis employs COMSOL Multiphysics software (Section 4.6 and 5.5.2) to compute the optical modes of drop-shaped resonators. By fixing the azimuthal mode number (m), we can identify multiple resonant modes characterized by axial (p) and radial (l) indices for both transverse electric (TE) and transverse magnetic (TM) polarizations.

As a demonstration of this approach, a rectangular resonator with a radius of 50 µm and a

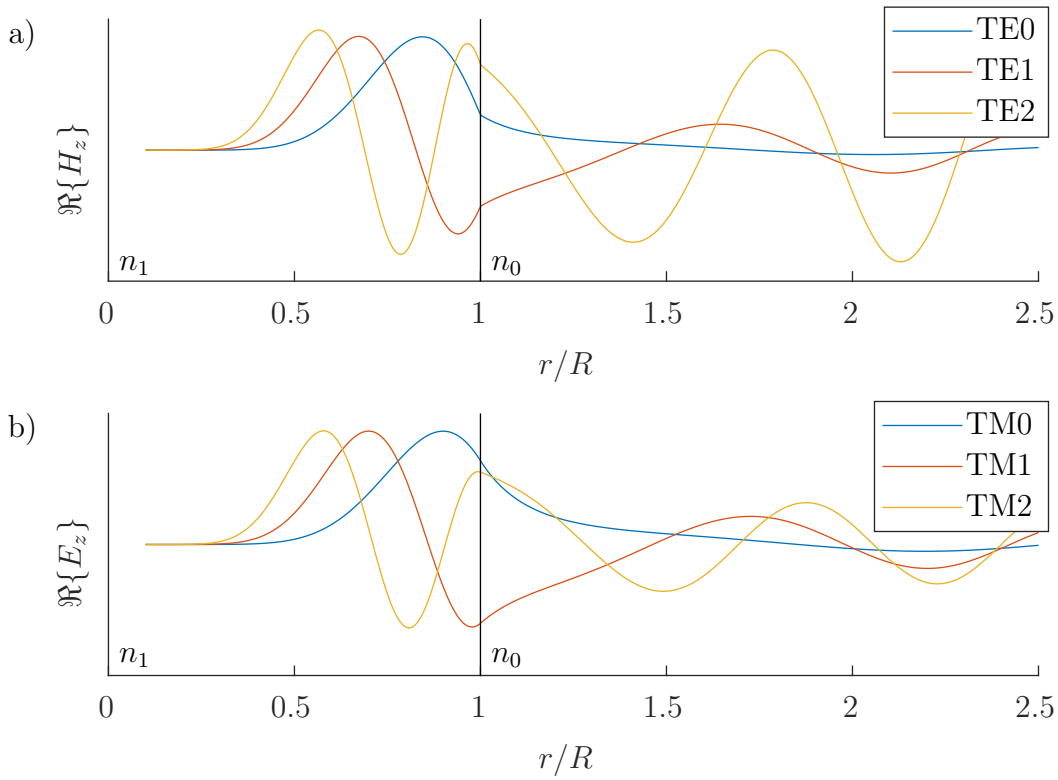

Figure 3.7 Radial amplitudes of the first solutions to a whispering gallery mode resonator with a refractive index ratio of 2. The azimuthal mode number is 10.

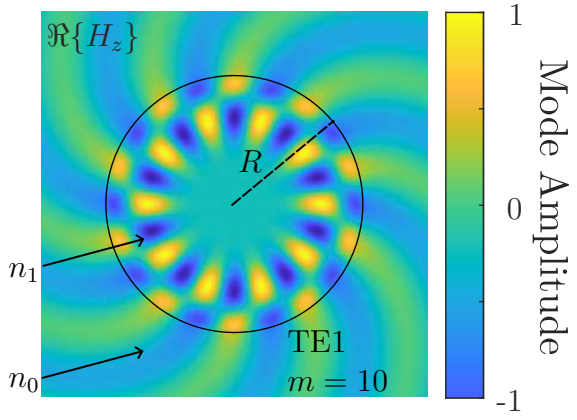

Figure 3.8 Whispering gallery mode amplitude of a disk with a radius R. The resonance mode has azimuthal number 10, and radial number l.

thickness of 2 µm was investigated at a central wavelength of 1550 nm. Figure 3.9 presents five identified modes, denoted as either TE_{pl} or TM_{pl}. The modal amplitude profiles exhibit

characteristics of both slab waveguide modes along the z-axis and WGMs along the radial axis.

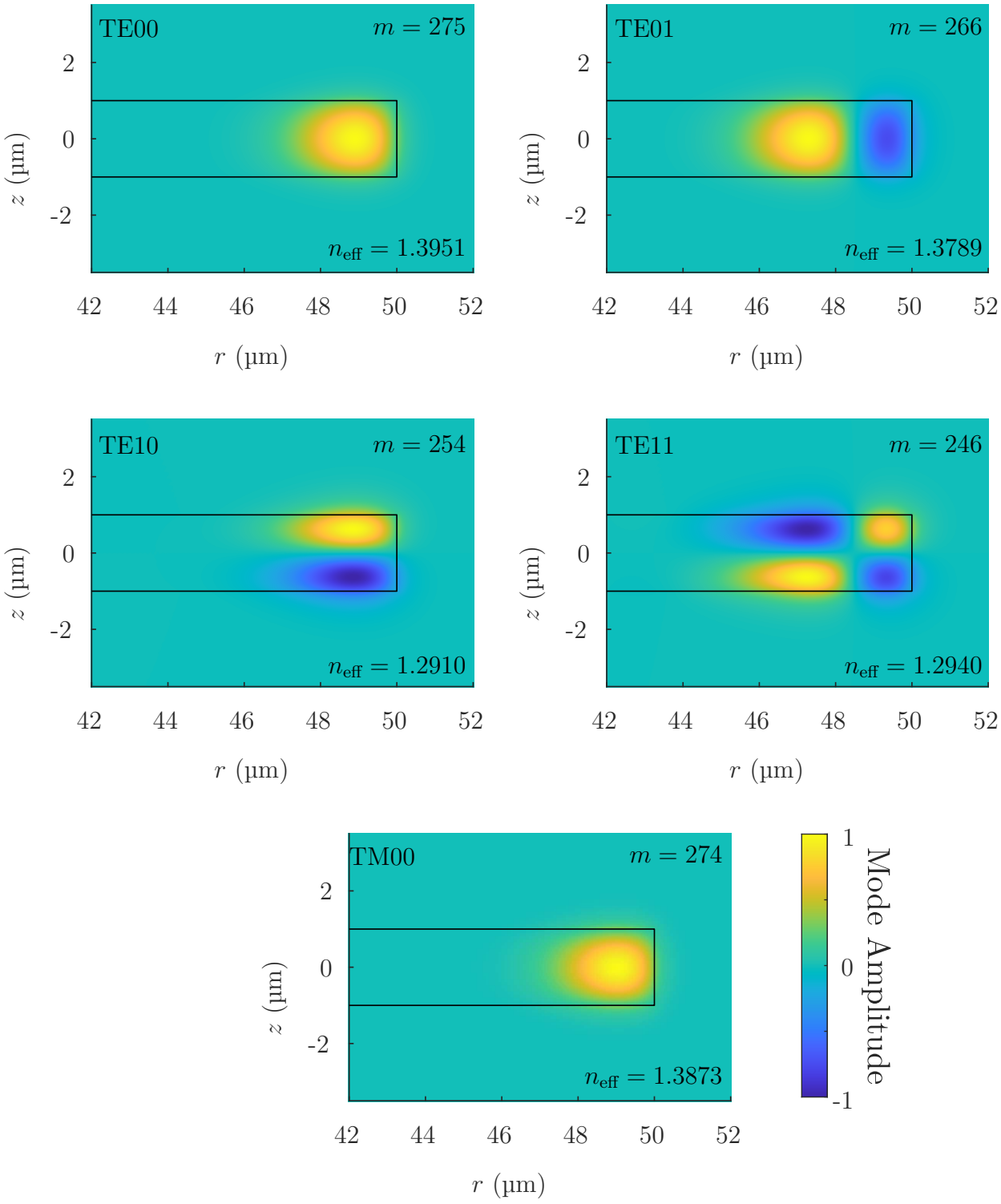

Figure 3.9 Calculated TE and TM mode profiles for a rectangular resonator with a radius of 50 µm and a thickness of 2 µm. The mode numbers (m,pl), effective indices (n_{eff}), and polarization types (TE or TM) are labeled for each mode.

3.2.3 Optical Coupling

To interrogate a WGM resonator and acquire its transmission spectrum, efficient coupling is essential. Various methods can be employed to couple light into and out of a resonator. In this thesis, coupling is achieved using a tapered optical fiber. This fiber, initially a standard telecommunications fiber (Corning SMF-28) with a cladding diameter of 125 µm, is heated and stretched to create a taper with a minimum cladding radius of only 2 µm. Due to the small core size, the optical mode of this structure is guided within the cladding. Consequently, coupling occurs through the evanescent field that extends into the surrounding air. Additionally, waveguide structures on photonic integrated circuits were also explored for coupling light into the resonator (Sec. 6.3).

Horizontal coupling, where the fiber is positioned at the edge of the resonator in the same plane, results in coupling at a single point, leading to weak coupling efficiency.

Vertical coupling occurs when the tapered optical fiber or waveguide is positioned above or below the resonator, as illustrated in Figure 3.10 a). In this configuration, coupled mode theory can be employed to calculate the coupling, assuming a constant coupling coefficient over an effective length, L_{eff}, as depicted in Figure 3.10 b).

Flat Zone

The coupling region is defined by a constant separation between the optical mode of the resonator and the waveguide [180]. In the waveguide reference frame, the modal horizontal separation $s_h(z)$, relative to the resonator, is a function of the light's position, z, in the waveguide:

$$s_h(z) = \delta x + R - \sqrt{R^2 - z^2} \tag{3.29}$$

where R is the resonator radius and δx is the structure horizontal separation between the optical modes at the coupling point. Figure 3.10 c) illustrates this function in orange, showing no apparent plateau.

The total separation $s_T(z)$ is then given by:

$$s_T(z) = \sqrt{s_h(z)^2 - s^2} \tag{3.30}$$

where s is the constant vertical separation between the optical modes. The blue curve in Figure 3.10 c) represents this function, which exhibits a noticeable plateau.

It's important to note that, in the case of horizontal coupling, the vertical separation, s, is zero, and the total separation is equivalent to the horizontal separation, lacking a plateau.

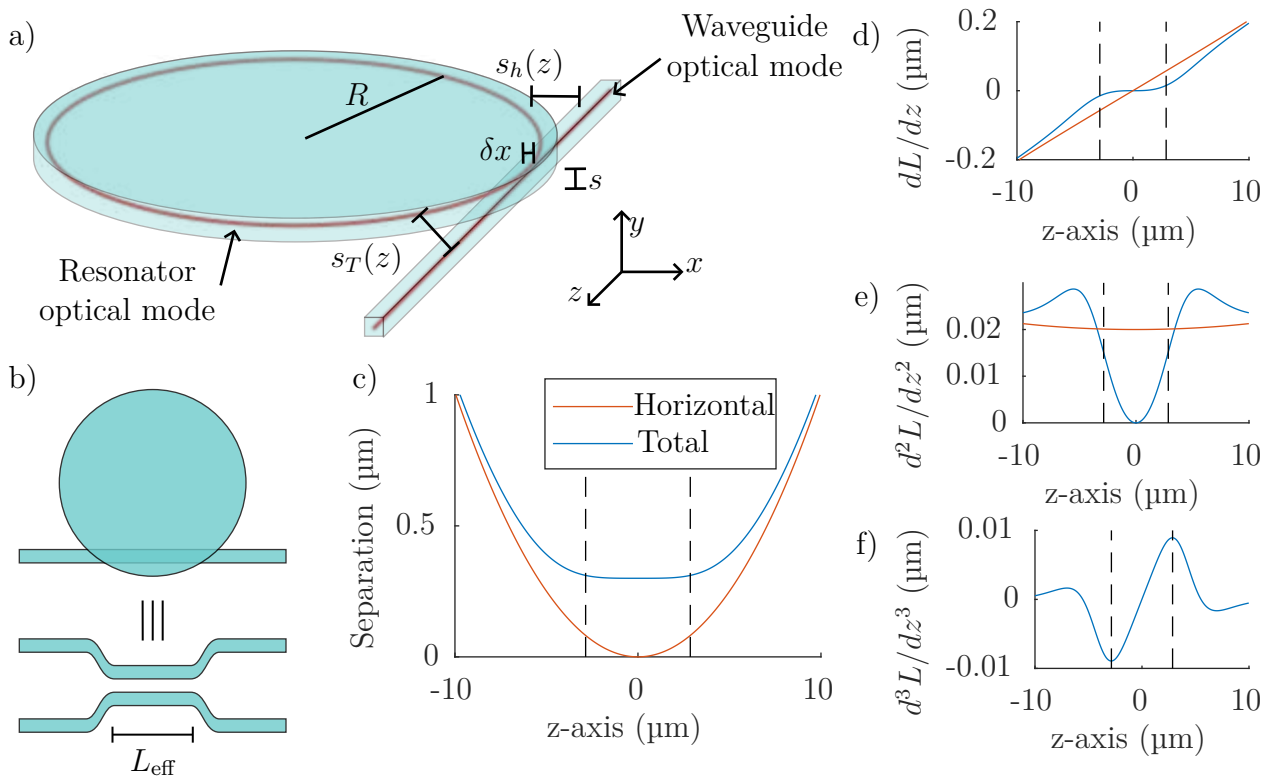

Figure 3.10 a) Vertical coupling between a disk resonator and a waveguide b) by the coupled mode theory with a effective length, L_{eff}. c) Horizontal and total separation as a function of the light propagation in z d-f) and their derivatives.

To determine L_{eff}, the plateau region of the total separation function must be measured. Previous studies have suggested identifying the inflection points of the first derivative, which correspond to the first extrema on either side of the coupling point of the third derivative. These functions are illustrated in Figure 3.10 d) to f).

Coupled Mode Theory

Coupled mode theory (CMT) is an approximation of the coupling between two straight waveguides. Many formalisms were developed [187]. Since the optical modes of the resonator and the waveguide are different, a non-orthogonal coupled-mode formalism is preferred [188]. The linear superposition of the modes is given by:

$$\overrightarrow{E} = a_1(z)\overrightarrow{e_1} + a_2(z)\overrightarrow{e_2} \tag{3.31}$$

$$\overrightarrow{H} = a_1(z)\overrightarrow{h_1} + a_2(z)\overrightarrow{h_2} \tag{3.32}$$

where $\overrightarrow{E}$ and $\overrightarrow{H}$ are the superposition electric and magnetic field, $\overrightarrow{e_i}$, and $\overrightarrow{h_i}$, the vector waveguide modes of both structure and a_i, the mode amplitudes.

The coupled-mode equation can be written as:

$$\mathbf{P}\frac{d}{dz}\mathbf{a} = -i\overline{\mathbf{H}}\mathbf{a} \tag{3.33}$$

with the unknown amplitude vector a:

$$\mathbf{a}(z) = \begin{bmatrix} a_1(z) \\ a_2(z) \end{bmatrix} \tag{3.34}$$

The matrix $\overline{\mathbf{H}}$ is:

$$\overline{\mathbf{H}} = \mathbf{P}\begin{bmatrix} \beta_1 & 0 \\ 0 & \beta_2 \end{bmatrix} + \overline{\mathbf{K}} \tag{3.35}$$

Finally, the power matrix elements P_{ij} and the coupling coefficients $\overline{K}_{ij}$ are:

$$P_{ij} = \frac{1}{4}\int_A \left[\overrightarrow{e_i}^* \times \overrightarrow{h_j} + \overrightarrow{e_j} \times \overrightarrow{h_i}^*\right] \cdot \hat{z}da \tag{3.36}$$

$$\overline{K}_{ij} = \frac{1}{4}\omega\epsilon_0 \int_A \left(\overline{n}^2 - n_j^2\right) \overrightarrow{e_i}^* \cdot \overrightarrow{e_j} da \tag{3.37}$$

where $\overline{n}$ is the refractive index distribution with both structure and n_j is the refractive index distribution of the structure j alone.

These matrices are only dependent on the vector waveguide modes and the refractive index distribution.

The differential matrix equation can be written as:

$$\frac{d}{dz}\mathbf{a} = -i\mathbf{P}^{-1}\overline{\mathbf{H}}\mathbf{a} \tag{3.38}$$

$$= -i\mathbf{M}\mathbf{a} \tag{3.39}$$

which is a system of homogeneous first-order linear ordinary differential equations.

The solution is of the form:

$$\mathbf{a}(z) = c_a\xi^{(\mathbf{a})}e^{-i\beta_a z} + c_b\xi^{(\mathbf{b})}e^{-i\beta_b z}, \tag{3.40}$$

$$= \mathbf{\Psi}(z)\mathbf{c}, \tag{3.41}$$

where $\xi^{(i)}$ and β_i are the eigenvectors and the eigenvalues of the matrix $\mathbf{M}$ and c_i needs to

be determined with the boundary conditions. Thus, it can be written as an evolution matrix $\mathbf{\Psi}(z)$ and a coefficient vector $\mathbf{c}$.

The initial conditions are the amplitude vector $\mathbf{a}_0$. Thus, the coefficients can be expressed with the initial condition and the initial evolution matrix:

$$\mathbf{a}_0 = \mathbf{\Psi}_0 \mathbf{c}, \tag{3.42}$$

$$\mathbf{c} = \mathbf{\Psi}_0^{-1} \mathbf{a}_0. \tag{3.43}$$

The amplitude evolution is then:

$$\mathbf{a}(z) = \Phi(z)\mathbf{a}_0 \tag{3.44}$$

$$\Phi(z) = \mathbf{\Psi}(z)\mathbf{\Psi}_0^{-1} \tag{3.45}$$

The evolution of power transfers between the waveguides is illustrated in Figure 3.11 for the case where all power is initially in the first waveguide (a_1). Three distinct lengths can be defined. First, in the absence of mode beating ($\sqrt{M_{11}M_{22}} = 0$), complete power transfer from one waveguide to the other occurs after the coupling length L_C. However, mode beating limits the maximum power transfer to a shorter length $L_{\max}$, which depends on both the coupling length L_C and the beating length L_b:

$$L_C = \frac{2\pi}{\sqrt{M_{12}M_{21}}}, \tag{3.46}$$

$$L_b = \frac{2\pi}{\sqrt{M_{11}M_{22}}}, \tag{3.47}$$

$$L_{\max} = \sqrt{\frac{1}{L_C^2} + \frac{1}{L_b^2}}. \tag{3.48}$$

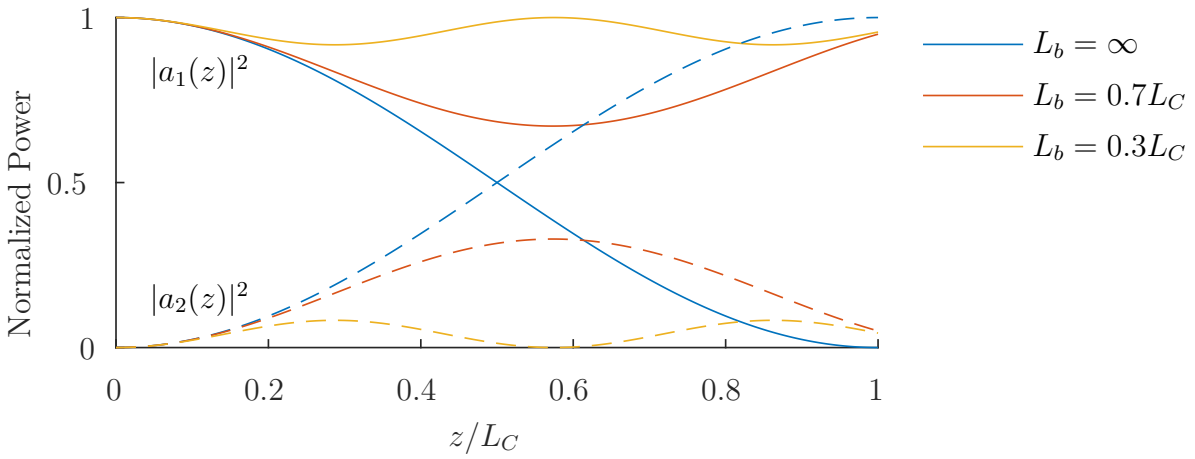

Figure 3.11 Evolution of power coupling between waveguides for varying beating lengths.

Whispering Gallery Mode Resonator Coupling

The coupling system between a resonator and a waveguide is illustrated in Fig. 3.12 for a counterclockwise propagation in the resonator. The coupling is represented by the coupling matrix $\Phi(z)$ evaluated for the effective coupling length due to the flat zone L_{eff}. The input amplitudes of the coupling are noted a and c for the resonator and the waveguide respectively, and, in the same order, b and d for the output coupling amplitudes.

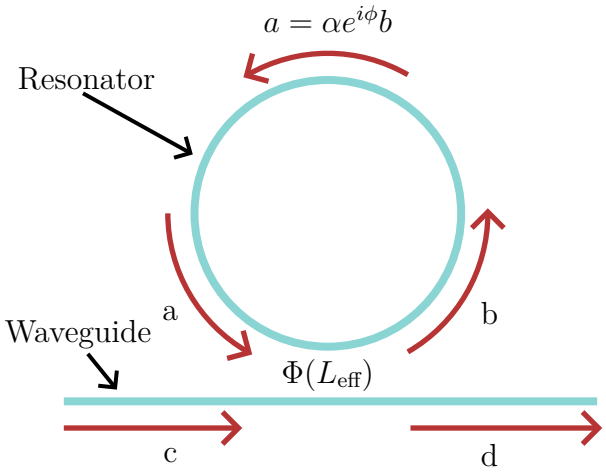

Figure 3.12 Illustration of the coupling between a waveguide and a resonator by the matrix method. The light amplitudes a, b, c, and d are related with the coupling matrix $\Phi(z)$ evaluated for a coupling length equals to the flat zone length L_{eff} and the propagation in the resonator.

These amplitudes are related with the $\Phi(z)$ matrix:

$$\Phi(L_{\text{eff}}) = \begin{bmatrix} t_{11} & \kappa_{12} \\ \kappa_{21} & t_{22} \end{bmatrix} \tag{3.49}$$

$$\begin{bmatrix} b \\ d \end{bmatrix} = \begin{bmatrix} t_{11} & \kappa_{12} \\ \kappa_{21} & t_{22} \end{bmatrix} \begin{bmatrix} a \\ c \end{bmatrix} \tag{3.50}$$

Since it is a resonator, the out-coupling light will come back at the input. In other words, the amplitude a is connected to the amplitude b with:

$$a = \alpha e^{i\phi} b \tag{3.51}$$

where ϕ is the phase accumulated after one round trip ($\phi = 2\pi(R - L_{\text{eff}})n_{\text{eff}}$), and α is the accumulated loss given with $\alpha = 1 - \frac{2\pi R n_{\text{eff}}}{\lambda Q_{\text{int}}}$.

By combining these last two equations, this system can be solved for an arbitrary waveguide input c for both the resonator (b) and the waveguide (d):

$$b = \frac{\kappa_{12}}{1 - \alpha t_{11} e^{i\phi}} c \tag{3.52}$$

$$d = \left(t_{22} + \frac{\alpha \kappa_{12} \kappa_{21} e^{i\phi}}{1 - \alpha t_{11} e^{i\phi}} \right) c \tag{3.53}$$

Thus, the power ratio inside the resonator B and the transmission T are:

$$B = \left| \frac{b}{c} \right|^2, \tag{3.54}$$

$$= \left| \frac{\kappa_{12}}{1 - \alpha t_{11} e^{i\phi}} \right|^2, \tag{3.55}$$

$$T = \left| \frac{d}{c} \right|^2, \tag{3.56}$$

$$= \left| t_{22} + \frac{\alpha \kappa_{12} \kappa_{21} e^{i\phi}}{1 - \alpha t_{11} e^{i\phi}} \right|^2. \tag{3.57}$$

The resonance peak is located at the phase equals zero of the term $t_{11} e^{i\phi}$.

Optimal Coupling

The coupling constant related to the coupling loss is:

$$\kappa = \left|\kappa_{12}\kappa_{21}\right|. \tag{3.58}$$

and the associated quality factor (Q-factor) is:

$$Q_{\mathrm{c}} = \frac{2\pi}{\lambda_0}\frac{2\pi R n_{\mathrm{eff}}}{|\kappa|^2} \tag{3.59}$$

This source of loss will add up to the intrinsic loss related to Q_{int} to give the total quality factor Q_{tot} with [189]:

$$\frac{1}{Q_{\mathrm{tot}}} = \frac{1}{Q_{\mathrm{int}}} + \frac{1}{Q_{\mathrm{c}}}. \tag{3.60}$$

The final resonance peak on the spectrum will have a width related to the total quality factor. The coupling is noted optimal when Q_{c} is equal to Q_{int} [167].

3.3 Detection Principle

Coupled resonators can be employed for sensing applications due to their high quality factors, which amplify the light-medium interaction. By interrogating a resonator with a waveguide, for example, changes in the resonance peaks, such as shifts in wavelength, changes in intensity, changes in width, or mode splitting, can be detected, as illustrated in Figure 3.13.

The peak position is directly related to the optical path, as described by Equation (3.15). Consequently, changes in the radius or refractive index of either the surrounding medium or the resonator will result in a shift in the peak wavelength [190].

The peak intensity is primarily influenced by the optical coupling. Variations in the distance between the resonator and the waveguide or changes in their refractive indices will lead to corresponding changes in the peak intensity [191].

The width of the peak is associated with the optical loss within the resonator. Therefore, the addition of losses, such as a single particle on the resonator surface, can be detected [192].

Mode splitting occurs when light propagates in both clockwise and counterclockwise directions. The interference between these two resonances lifts the degeneracy. A particle on the resonator surface can scatter light into the opposite direction, resulting in the splitting of the optical resonance [193, 194].

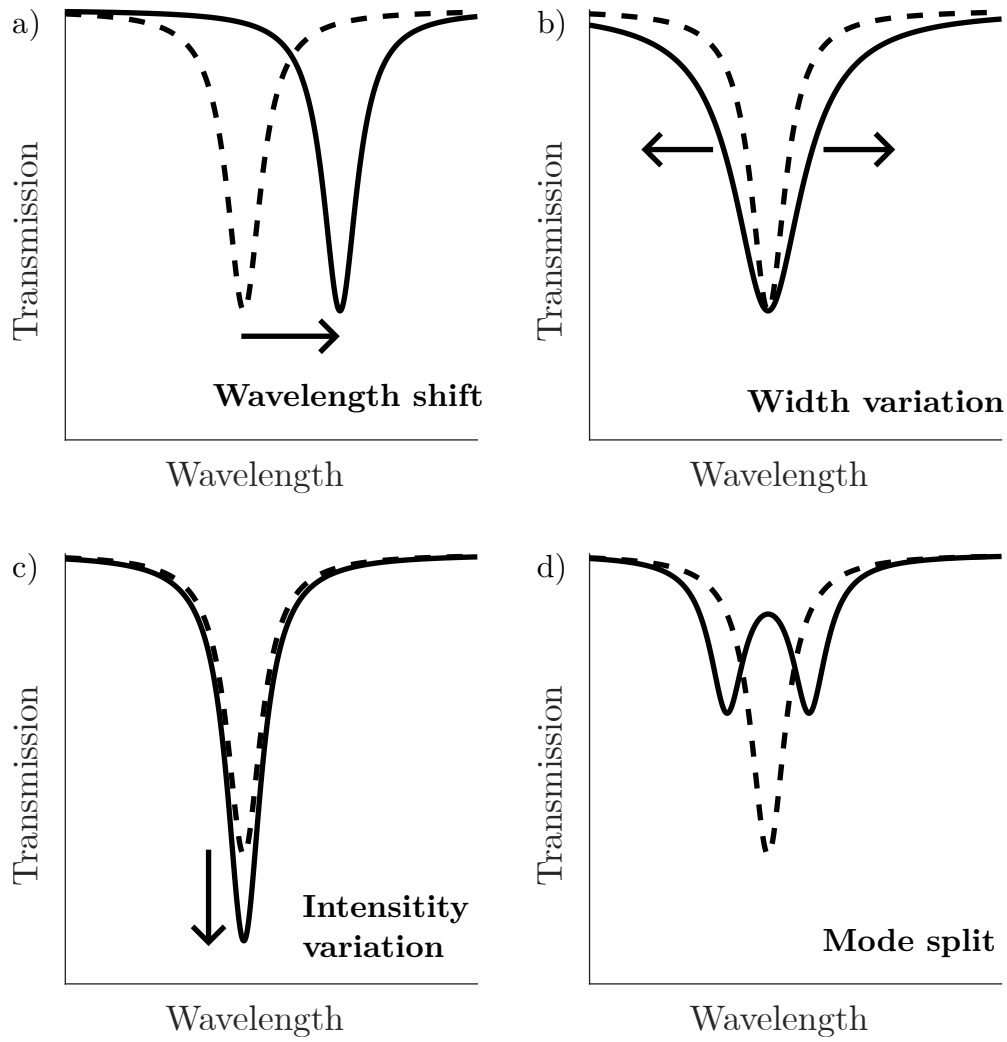

Figure 3.13 Detection principles of optical resonator sensors comprising a) wavelength shift, b) width variation, c) intensity variation and d) mode split.

Among these detection methods, wavelength shift ($\Delta\lambda$) is often preferred due to its linear relationship with changes in refractive index (Δn) and expansion (ΔR). This mechanism for temperature and concentration sensing can be expressed as:

$$\frac{\Delta\lambda}{\lambda} = \frac{\Delta R}{R} + \frac{\Delta n}{n} \tag{3.61}$$

$$= \left[\left(\frac{\partial R}{\partial T}\right)_{C_i}\frac{1}{R} + \left(\frac{\partial n}{\partial T}\right)_{C_i}\frac{1}{n}\right]\Delta T + \sum_{m=1}^{M}\left[\left(\frac{\partial R}{\partial C_m}\right)_{T,C_{i\neq m}}\frac{1}{R} + \left(\frac{\partial n}{\partial C_m}\right)_{T,C_{i\neq m}}\frac{1}{n}\right]\Delta C_m \tag{3.62}$$

where T is the temperature and C_m is the concentration of the analyte m. The terms $\left(\frac{\partial R}{\partial T}\right)_{C_i}$ and $\left(\frac{\partial n}{\partial T}\right)_{C_i}$ represent the thermal expansion and thermo-optic coefficient of the resonator material, respectively. Similarly, the terms $\left(\frac{\partial R}{\partial C_m}\right)_{T,C_{i\neq m}}$ and $\left(\frac{\partial n}{\partial C_m}\right)_{T,C_{i\neq m}}$ are the expansion and change in refractive index of the resonator per unit concentration of analyte m. This equation assumes linear independence between the temperature and analyte concentrations. The coefficients discussed in the first (Section 4.6) and second articles (Section 5.5.2), respectively, are analyzed to determine their corresponding sensitivities (S_T ans S_{C_m}) and limit of detections (LODs). These metrics are defined as follows:

$$S_T = \frac{\Delta\lambda}{\Delta T} \tag{3.63}$$

$$S_{C_m} = \frac{\Delta\lambda}{\Delta C_m} \tag{3.64}$$

$$LOD = \frac{3\sigma}{S} \tag{3.65}$$

The limit of detection is not only determined by sensitivity but also by the noise of the peak position, denoted as σ. It is experimentally calculated from mean noise of the peak position while in a nitrogen atmosphere and maintaining the temperature constant.

Theoretically, the noise of the peak position can be decomposed in three components [195]: the amplitude noise $\sigma_{\text{ampl-noise}}$, the cross-talked $\sigma_{\text{cross-talked}}$ and the spectral resolution $\sigma_{\text{spect-res}}$:

$$\sigma = \sqrt{\sigma^2_{\text{ampl-noise}} + \sigma^2_{\text{cross-talked}} + \sigma^2_{\text{spect-res}}} \tag{3.66}$$

First, based on a Monte Carlo simulation [195], the amplitude noise contribution is directly related to the signal-to-noise ratio (SNR) and the quality factor (Q) according to the equation:

$$\sigma_{\text{ampl-noise}} = \frac{\lambda}{4.5Q(\text{SNR})^{0.25}} \tag{3.67}$$

While high-Q factor resonators do not inherently guarantee high sensitivities, they do offer the advantage of lower limit of detections.

Second, due to the non-selective nature of polymers, which can be sensitive to multiple quantities simultaneously, noise contributions from these additional factors can influence the overall noise. To mitigate this effect, it is crucial to measure these quantities with greater precision.

Finally, the spectral resolution of the optical resonator interrogation apparatus can impose

limitations on the detection capabilities.

3.4 Gas Diffusion in a Polymer Matrix

The response time of the sensor is influenced by several factors, including the diffusion of the target gas through the air to the sensing polymer, the sorption process within the polymer, the diffusion of the gas within the polymer matrix, and the time required for property changes induced by the absorbed gas. Fick's first law of diffusion describes the gas flux (J) for a given gas gradient (∇C) using the diffusion coefficient (D):

$$J = -D\nabla C \tag{3.68}$$

By incorporating the mass conservation principle, Fick's second law of diffusion is expressed as:

$$\frac{\partial C}{\partial t} = D\nabla^2 C \tag{3.69}$$

For a suspended resonator, the diffusion scenario of a thin layer on a substrate can be adapted from temperature diffusion with modified interface conditions [196]. Figure 3.14 a) illustrates the diffusion case involving a semi-infinite thin polymer film in orange, with a thickness d in the y-direction. The concentrations on both sides of the film are denoted as $\phi_1(t)$ and $\phi_1(t)$, while the initial concentration is represented by $C(y, 0)$.

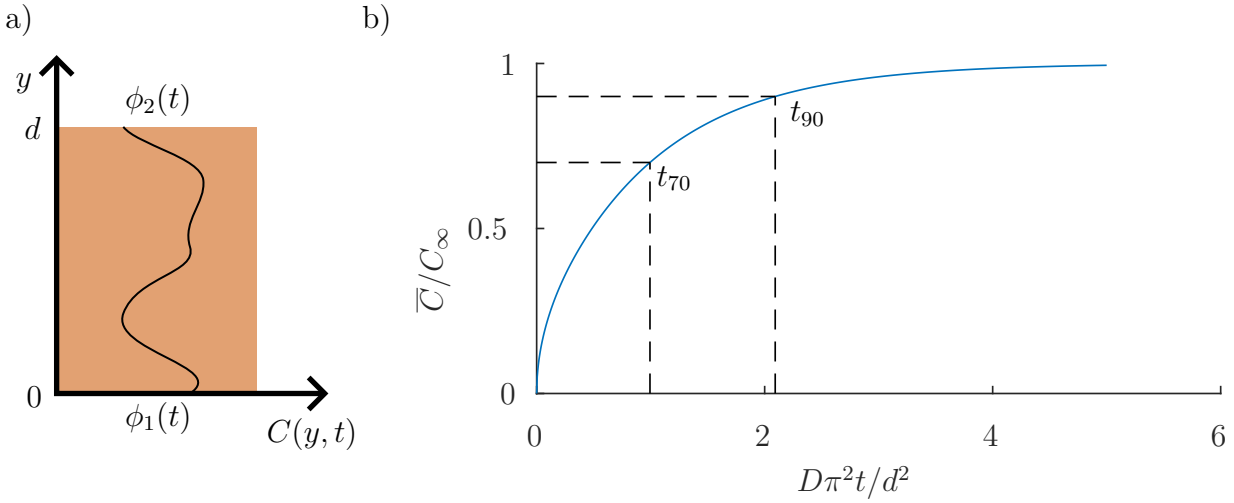

Figure 3.14 a) Gas diffusion in a semi-infinite thin polymer film and b) the resulting mean concentration with time.

To further simplify the problem, we assume a homogenous initial concentration within the

polymer film and equal concentrations at the interfaces. This scenario is described by the following equations:

$$\begin{aligned} \frac{\partial C}{\partial t} &= D\frac{\partial^2 C}{\partial y^2} \ (0 < y < d) \\ C(0,t) &= C(d,t) = \phi(t) \\ C(y,0) &= C_0 \end{aligned}$$

The detailed derivation is provided in the appendix (Appendix A). The evolution of the mean concentration ($\overline{C}$) is given by:

$$\overline{C} = 8\frac{C_0}{\pi^2}\sum_{m=0}^{\infty}\frac{e^{-\frac{D(2m+1)^2\pi^2}{d^2}t}}{(2m+1)^2} + 8\frac{D}{d^2}\sum_{m=0}^{\infty} e^{-\frac{D(2m+1)^2\pi^2}{d^2}t}\int_0^t e^{\frac{D(2m+1)^2\pi^2}{d^2}\lambda}\phi(\lambda)d\lambda$$

For a concentration step from 0 to C_∞ at $t = 0$, the equation simplifies to:

$$\overline{C}(t) = \frac{8}{\pi^2}C_\infty\sum_{m=0}^{\infty}\frac{1 - e^{-\frac{D(2m+1)^2\pi^2}{d^2}t}}{(2m+1)^2}$$

Although an analytical solution for this function is not feasible, it exhibits rapid convergence. Figure 3.14 b) illustrates the calculation of the first 1×10^5 terms, which yields a mean squared error (MSE) of 1.0×10^{-12} compared to the first 2×10^5 terms. Numerically, 70 % and 90 % of C_∞ are achieved after $D\pi^2/d^2t$ equals 1.00 and 2.09, respectively.

For SU-8 and water, a diffusion coefficient of 0.3 µm^2/s has been reported [197]. Given the resonator thickness of approximately 1.0 µm in this thesis, 70 % and 90 % of C_∞ are expected to be reached after 0.34 s and 0.71 s seconds, respectively. These calculated values are significantly lower than the experimentally observed response times of 36 s and 108 s (Section 5.7.4). This discrepancy suggests that either the reported diffusion coefficient is not applicable to this fabrication method or the response time is not solely limited by diffusion. Since this characterization setup is capable of measuring smaller response times (down to 12 s), another potential explanation could be a slow change in polymer properties, such as expansion.

3.4.1 Summary

The theoretical framework of the gas sensor, based on a WGM resonator, was explored. The disk resonator was analyzed by separating it into a slab waveguide and a 2D WGM

resonator. The optical losses associated with this structure were discussed, and the analysis was extended to arbitrary axisymmetric optical resonators through numerical calculations. Optical coupling was then explored, including effective coupling length, coupled mode theory, and resulting transmission spectra. Various detection principles were presented, with a focus on wavelength shift detection and key performance metrics such as sensitivity, LOD, and noise. Finally, the theory of gas diffusion in a polymer matrix was explored to understand the sensor's time response.

CHAPTER 4 ARTICLE 1 - TEMPERATURE SENSITIVITY CONTROL OF AN INKJET-PRINTED OPTICAL RESONATOR ON PILLAR

This chapter investigates the temperature sensitivity of suspended microresonators fabricated by inkjet printing. It is a published article titled "Temperature Sensitivity Control of an Inkjet-Printed Optical Resonator on Pillar" from the journal of ACS Applied Materials & Interfaces[1] and which the first author, Marc-Antoine Bianki did the majority of the work which includes the design, fabrication, experimental measurements, analysis and the redaction. The co-authors helped with discussion, the experimental setup and the revision. It is the first look into this micromanufacturing process of suspended polymer microdroplets on a silicon pillar combining inkjet printing and traditional microfabrication. The ink is SU-8, a photoresist commonly used in microfabrication. This process is also used in the second article with the addition of other polymers. It is followed by a geometric characterization which revealed a unique resonator shape coming from the coffee ring effect. These resonators are coupled with a tapered optical fiber to study their optical transmission spectra, more specifically, the wavelength shift of the resonance peaks with temperature. This is important because polymer sensors are notoriously sensitive to temperature fluctuations, which can compromise the accuracy of gas measurements. Thus, by systematically varying the undercut length of the microresonators, we demonstrate a tunable temperature sensitivity, enabling the achievement of temperature-insensitive devices. To understand the underlying mechanisms, extensive numerical simulations were conducted to analyze the effects of thermal expansion and thermo-optic effects on the optical mode. Our findings provide valuable insights into minimizing temperature crosstalk in these structures, paving the way for their application in gas sensing and other temperature-sensitive applications.

Published September 26, 2023

4.1 Authors and Affiliations

Marc-Antoine Bianki[a,*],Régis Guertin[a],Cédric Lemieux-Leduc[a],Yves-Alain Peter[a]

[a] *Department of Engineering Physics, Polytechnique Montréal, Montréal, QC, H3T 1J4, Canada*

[1]M.-A. Bianki, R. Guertin, C. Lemieux-Leduc, and Y.-A. Peter, "Temperature Sensitivity Control of an Inkjet-Printed Optical Resonator on Pillar", *ACS Applied Materials & Interfaces*, Jan. 2024, DOI: 10.1021/acsami.3c14406.

4.2 Abstract

We report a whispering gallery mode resonator on pillar using inkjet printing combined with traditional microfabrication techniques. This approach enables several different polymers on the same chip for sensing applications. However, polymers inherently exhibit sensitivity to multiple stimuli. To mitigate the temperature sensitivity, careful selection of design parameters is crucial. By precisely tuning the undercut-to-radius ratio of the resonator, a linear dependance in temperature sensitivity ranging from $-41.5\,\mathrm{pm/°C}$ to $23.4\,\mathrm{pm/°C}$, with a zero-crossing point at $47.6\,\%$ is achieved. Consequently, it is feasible to fabricate sensing devices based on undercut microdroplets with minimal temperature sensitivity. The lowest measured temperature sensitivity obtained was $5.9\,\mathrm{pm/°C}$, for a resonator with an undercut-to-radius ratio of $53\,\%$.

Keywords - Whispering gallery modes, Optical sensors, Microcavities, Temperature sensors, Thermal expansion, Thermo-optic effects, Inkjet printing, Microfabrication.

4.3 Introduction

Polymers, as stimuli-responsive materials, are widely studied for sensing various parameters [71]. Among these, gas concentration measurement, crucial in food industry, air quality, mining, and healthcare [127], could benefit from their cost-effective nature and reversible behavior. These sensors can be either electronic [198, 199] or optical [200].

Optical resonators exhibit exceptional suitability for polymer sensors due to their high sensitivity to small changes. They exist in diverse cavity configurations, including Fabry-Perot, microrings, microdisks, and microbottles [201]. The latter is known as whispering gallery mode resonators for which light undergoes total internal reflection at the circular boundary, resulting in high-quality factors and low mode volumes. PDMS microbottle [62] and in-fiber polymer microdisk [202] were used for sensing.

In our prior work, we investigated the gas concentration sensitivity of SU-8 disks on silicon pillars [24]. This configuration allows a section of the polymer to freely swell due to its hanging part, resulting in a tenfold increase in sensitivity to gas concentrations compared to Fabry-Perot resonators functionalized with the same polymer. However, two challenges persisted. The first challenge involves the lack of selectivity towards a single gas, as this particular polymer demonstrates sensitivity to at least six gases. The second challenge relates to temperature sensitivity, since to obtain the reported limits of detection, temperature fluctuations must be maintained below $80\,\mathrm{mK}$.

Since it was shown that the affinity of polymers are different for each gas, with the response of multiple polymers, it is possible to get the concentration of each gas from a mixture [22]. However, the current microfabrication process—comprising spin coating and photolithography—restricts the utilization of only one photosensitive polymer per microchip. Additive methods like drop-on-demand inkjet printing are well suited to deposit these different polymers on the same optical microchip.

Polymeric resonators were reported to be successfully fabricated using inkjet printing and investigated for low-threshold lasing [26] and biosensing [28]. This technique proves to be cost-effective, minimizes material waste, and enables the production of smooth surfaces with ease. This versatile technique allows for the printing of various materials, including different polymers [154, 155, 158]. Moreover, printing of multiple materials in close proximity is possible, which is advantageous to create a sensor matrix [72].

The second issue is related to the versatility of polymers since they are sensitive to other quantities than gas concentration [203]. They can be used, for example, as a temperature sensor [204] or a pH sensor [73]. This versatility is both an advantage and a disadvantage since it can lead to cross-sensitivity issues, resulting in erroneous readings of the measured values. In the case of temperature sensitivity, specifically, the high thermal expansion and thermo-optic coefficients of polymers which make them advantageous for optical temperature sensing applications [204], pose challenges when measuring other quantities [75, 110].

First, temperature can be decoupled by measuring it [22, 60, 77, 205]. By subtracting the contribution of the temperature, it becomes possible to extract the desired value accurately. However, since each measurement carries inherent errors, the device precision is decreased. Thus, it is still important to lower the sensitivity of the interfering quantity to some sensing elements.

Thus, another strategy would be treating the polymer matrix using high-temperature annealing [76] or incorporating materials with negative temperature coefficients [78] to mitigate the temperature sensitivity. However, it increases the material complexity. We propose an additional strategy to mitigate temperature cross-sensitivity by optimizing design parameters. Our objective revolves around minimizing sensitivity to temperature by modifying the resonator's undercut.

To address both these issues, we studied the temperature sensitivity of a polymer microdroplet on a pillar combining inkjet printing technology and microfabrication. Our main motivation is to mitigate the temperature crosstalk of inkjet-printed SU-8 resonator towards the development of a general multi-polymer sensing platform, targeting first gas sensing.

The temperature sensitivity mechanism is based on the change of the resonance condition of the microdroplet (Fig. 4.1a). A rise in temperature induces polymer expansion and alters the refractive index (Fig. 4.1b). These phenomena are denoted as thermal expansion and thermo-optic effect, respectively. These changes lead to a shift in the resonance wavelength.

SU-8 was selected for this study to follow our previous work with humidity sensitivity of SU-8 disks on a silicon pillar using photolithography [24]. Moreover, previous research has shown successful inkjet printing of this polymer [157, 206–208] and it has been employed in the fabrication of humidity sensors [23].

4.4 Microfabrication and Optical Characterization

The fabrication process (Fig. 4.2a) begins with a cleaned silicon wafer (100 mm, <100>, p-type, 1-20 Ω cm). The substrate is dehydrated, then primed with hexamethyldisilazane (HMDS) to enhance adhesion of polymers. Drop-on-demand inkjet printing is employed to deposit SU-8 droplets (Step 1) by using MicroChem's SU-8 2000.5 (14.3 % solid in cyclopentanone) as the ink. The solution possesses a viscosity of 2.49 cP and a density of 1.070 g/mL. Printing is carried out using an inkjet printer (Microdrop Technologies) equipped with a piezoelectric-driven printing head. The printing parameters, as specified in Table 4.1, were optimized to ensure optimal stability during the deposition of the viscoelastic polymer ink [145]. In-flight droplets with a radius of 60 µm are obtained (Fig. 4.2b). Subsequently, a softbake was conducted on a hotplate for 5 min at 95 °C (Step 2). The droplets are then exposed to UV light with a dose of 160 mJ cm^{-2} using a Karl Suss MA-6 followed by a post-exposure bake on a hotplate for 5 min at 95 °C (Step 3). To form the pillar and to release the droplet, the silicon substrate is etched with an SF_6 plasma (Step 4). An inductively coupled plasma (ICP) system (Oxford Instruments PlasmaLab ICP System 100) is used with 500 W of power employing ions acceleration, and operating at 25 mTorr. The etching time is adjusted to control the desired undercut length.

Table 4.1 Inkjet printing parameters

Parameter	Value
Voltage (V)	85
Pulse duration (µs)	25
Nozzle diameter (µm)	100
Back pressure (mbar)	−16
Nozzle temperature (°C)	25
Substrate temperature (°C)	30

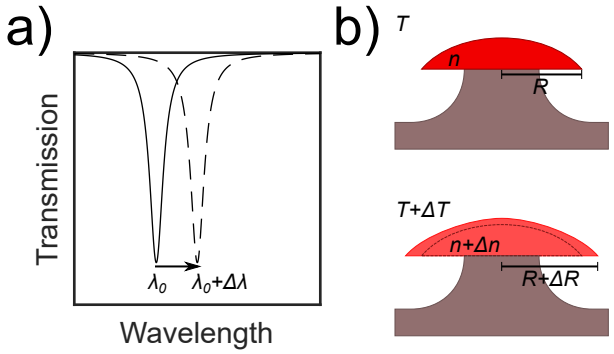

Figure 4.1 Temperature sensing mechanism of an all-polymer microdroplet on pillar. a) A peak shift ($\Delta\lambda$) is observed when the resonance condition varies with temperature (ΔT). b) This shift is attributed to thermal expansion (ΔR) and change of the refractive index (Δn).

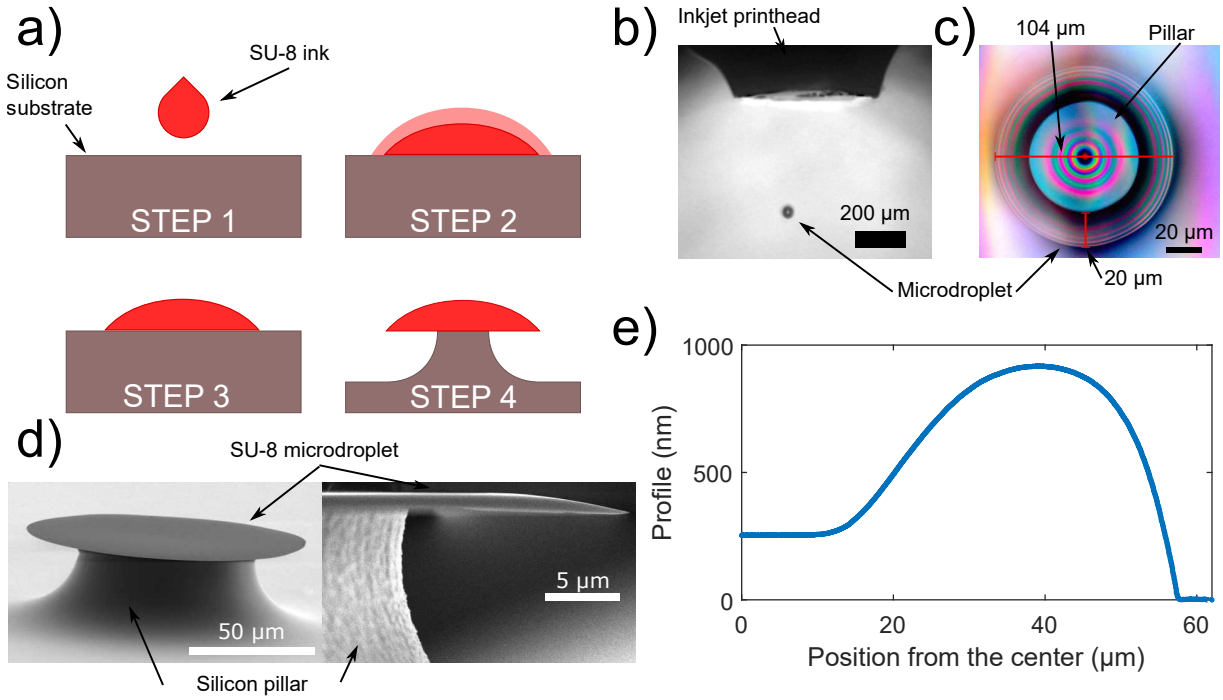

Figure 4.2 a) Fabrication process of a polymer microdroplet on pillar. b) In-flight inkjet-printed droplets ejected from the printhead. c) Top-down view of a microdroplet, revealing the underlying pillar. d) Scanning electron microscope images of the microdroplet on pillar. e) Radial height profile of the microdroplet.

Figure 4.2c shows a top view optical microscope image capturing an SU-8 microdroplet on pillar with a diameter of 104 µm and an undercut of 20 µm. Scanning electron microscopy (SEM) images (Fig. 4.2d) validate these values, providing both an overall and side view. The microdroplet's edge appears wedged. The profile of the droplet is further analyzed using profilometry, as depicted in Fig. 4.2e. The measurement begins at the center of the droplet and extends radially towards the edge, allowing for a comprehensive examination of its shape and dimensions. The resulting shape reveals a central plateau with a thickness of 254 nm. Additionally, a specific area positioned at a distance of 39.2 µm from the center exhibits a significantly higher thickness of 918 nm. This profile indicates the presence of the coffee ring effect [146], influenced by the rate of solvent evaporation and controllable with the substrate temperature.The surface morphology play also a role in the profile shape. The smooth, hydrophobic and homogeneous surface prior to the deposition ensures the circular symmetric structure essential for a whispering gallery mode resonator. Finally, the radial profile will impact slightly both the effective radius and the refractive index of the resonance optical mode where the edge wedge will push the mode inward [209]. This only affects temperature or gas concentration sensitivity minimally. Nevertheless, for consistency in the process, the substrate temperature was maintained at 30 °C.

Optical characterization was performed by taking the transmission spectrum of a tapered optical fiber (SMF-28e) with a diameter of about 1 µm coupled to the microdroplet. The optical fiber was positioned on the top surface and at the edge of the microdroplet using multi-axis precision stages. A tunable laser source is synchronized with an optical power meter to acquire the transmission spectrum. Resonances of both transverse electric (TE) and transverse magnetic (TM) modes were observed. To optimize the optical fiber mode to align with either of these resonant modes, a polarization controller was used.

Figure 4.3 shows an example of a transmission spectrum spanning over four free spectral ranges (FSR) which is 5 nm with six distinct modes represented by six minima. A closer examination around 1543.64 nm allows the measurement of the full width at half-maximum (FWHM) of the peak, which amounts to 106.1 pm. This measurement allows for the determination of the quality factor (Q-factor), yielding a value of 1.46×10^4. This value surpasses that of the photolithography SU-8 resonator [23] which has a Q-factor of 10^3. The surface tension of the droplet helps in smoothing the SU-8/air interface and decreases surface scattering loss. Moreover, it outperforms previous inkjeted microcavities [210] exhibiting a Q-factor of 10^4.

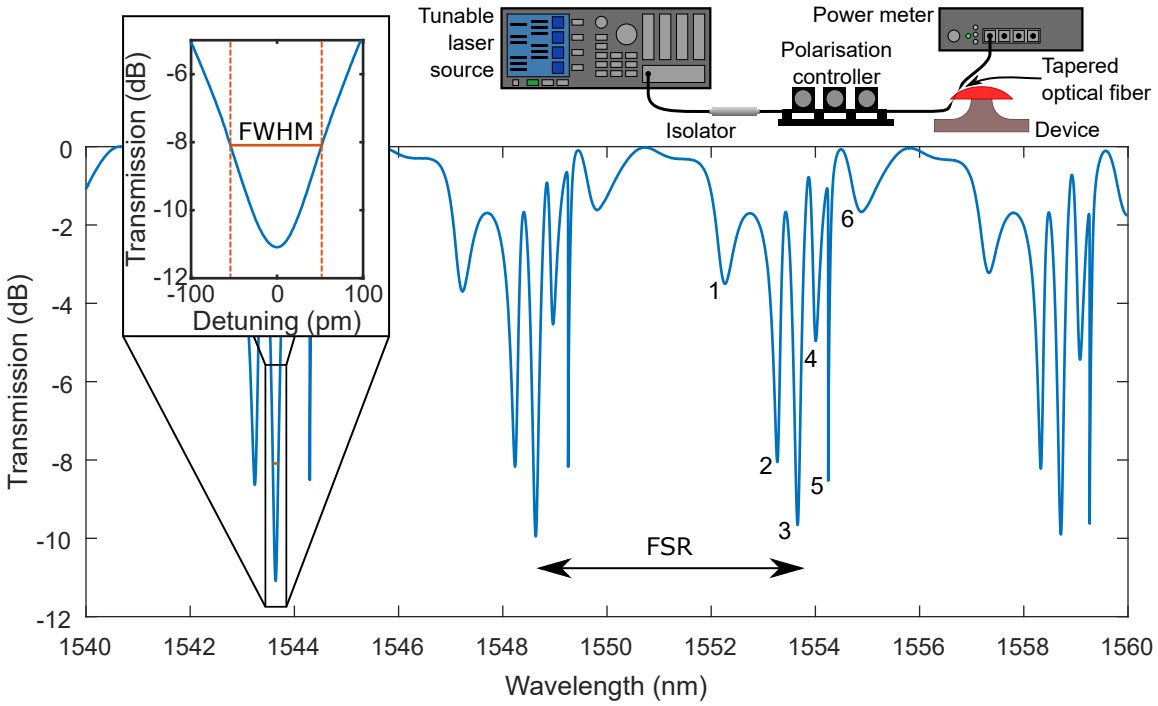

Figure 4.3 Optical transmission spectrum of a tapered optical fiber coupled to a microdroplet on pillar with a close-up view of a peak, along with a schematic representation of the experimental setup utilized.

4.5 Temperature Sensitivity Measurements

In order to assess the temperature sensitivity of the device, it is packaged within a compact enclosure and exposed to a controlled nitrogen flow with a flow rate of 5000 sccm regulated by a mass flow controller depicted in Fig. 4.4a. The temperature is controlled through a dual approach. Firstly, the chip is positioned on a thermoelectric module that is interfaced with a PID controller (MTD1020T). Secondly, the nitrogen flow passes troughs a heated copper block. The temperature of the nitrogen flow is measured immediately prior to its entry into the sample box. Both the temperature of the chip and the temperature of the nitrogen flow are adjusted in tandem, utilizing the same setpoint for precise temperature control.

The temperature range explored during the experiment spans from 30 °C to 44 °C which is significantly lower than the glass transition temperature of SU-8 of 210 °C. Two ramps are conducted where the initial ramp serves to condition the sensor. Transmission spectra are captured at intervals of 10 seconds. The position of each peak is recorded, as depicted in Fig. 4.4b. We observe a negative proportional response of the sensor as illustrated in Fig. 4.4c. The displacement of this peak amounts to approximately 0.6 nm for a temperature variation of 14 °C.

In order to quantify the temperature sensitivity, we conducted measurements by tracking the resonance peaks while systematically adjusting the temperature. Optical transmission spectra were acquired using the same setup employed for the initial optical characterization. At the end of each temperature plateau, the positions of the peaks were averaged over a duration of 90 seconds. By performing a linear regression analysis, the temperature sensitivity of the device was determined (Fig.4.4d). The control uncertainties, expressed as $3-\sigma$ errors, were found to be 7.6 m°C and 37.5 m°C for the chip and flow temperature measurements, respectively. Regarding the peak positions, the overall error was 8 pm.

These measurements were conducted on six different samples, each possessing a distinct undercut-to-radius ratio ranging from 22.5 % to 59.0 %. The corresponding sensitivities are presented in Table 4.2 along with the regression errors on the slope and the coefficients of determination R^2. The latter is minimal for the sample with the slightest sensitivity which gives peak displacement values near the noise level.

4.6 Modeling and Discussion

The temperature sensitivity was modeled by taking into account both the thermal expansion of the SU-8 material and its variation in refractive index with temperature, which is determined by the thermo-optic coefficient. Simulations were performed on the COMSOL

Table 4.2 Sensitivity measurements for six samples with different undercut-to-radius ratio

Ratio %	Undercut µm	Radius µm	Sensitivity pm/°C	Error pm/°C	R^2
22.5	12.8	57.1	−38.0	0.3	0.99
24.0	12.6	52.7	−41.5	0.4	0.99
32.6	17.0	52.2	−24.8	1.5	0.90
38.9	20.2	52.0	−18.3	0.6	0.84
53.3	27.4	51.4	5.9	0.6	0.62
59.1	30.9	52.3	23.4	1.6	0.92

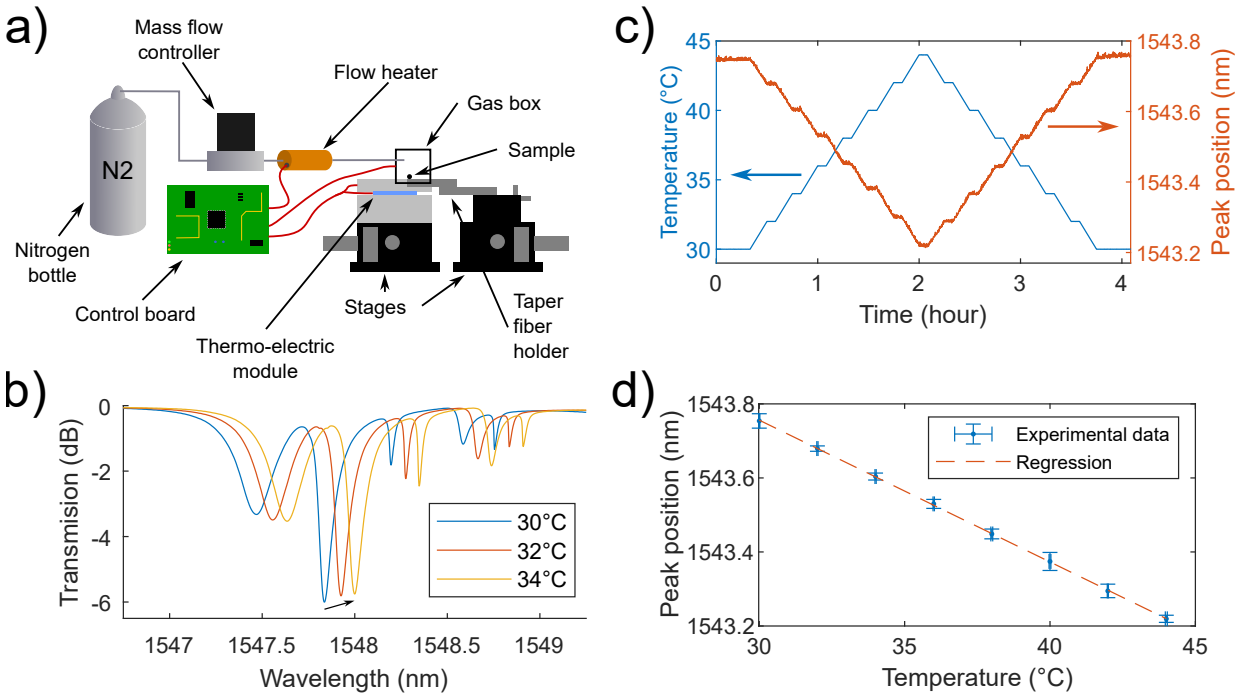

Figure 4.4 a) Experimental setup for the temperature sensitivity measurements. b) Spectra at different temperatures showing the peak displacement. c) Tracking of a single peak position while varying the temperature over time. d) Linear regression of the peak displacement versus temperature.

software employing finite element analysis over a 2.5D axis-symmetric model of the resonator on pillar. This modeling approach takes into account the inherent cylindrical symmetry of the problem, utilizing the radial coordinate r and the axial coordinate z. The origin of the coordinate system is positioned at the center of the droplet's base. The shape of the polymer resonator was obtained by extracting the measured profile (Fig. 4.2e). Mechanical properties utilized in the simulations were sourced from the photoresist datasheet, with values of 60 MPa for tensile strength and 2.0 GPa for Young's modulus.

The thermal expansion and thermo-optic coefficients were determined through ellipsometry measurements. The SU-8 was spin-coated on a silicon substrate, following the same treatment as the SU-8 microdroplets in terms of UV exposure and baking. Ellipsometry measurements were performed under a nitrogen atmosphere while varying the temperature from 25 °C to 90 °C. By analyzing the changes in refractive index and thickness with temperature, the thermal expansion coefficient and the thermo-optic coefficient were calculated. The obtained coefficient of thermal expansion was 150 ppm/K, which is three times higher than the value stated in the datasheet [211] (52 ppm/K). The thermo-optic coefficient was found to be −90 ppm/K, which is half of the values reported in the literature [212–214] at −180 ppm/K. To illustrate the effects of thermal expansion, the deformation of the material was simulated for a specific temperature change of 10 °C (Fig. 4.5a). In a second step, and using the thermo-optic coefficient to account for the change in refractive index, the optical resonance mode was then calculated based on the deformed shape (Fig.4.5b). The temperature was assumed to be uniform all across both the polymer and the pillar.

Upon observing the expansion resulting from a positive temperature change (Fig. 4.5c), it can be observed that the outer edge of the resonator expands outward by approximately 40 nm for a temperature increase of 10 °C, while also bending downward by around 20 nm for the same temperature change. This behavior is attributed to the difference in thermal expansion coefficients between the SU-8 material and the silicon substrate. Following the mode calculation, we extract both the effective refractive index and the change in the material's refractive index. They both exhibit a decrease with increasing temperature. Consequently, the resonance wavelength of the system will be influenced by both the change in refractive index and the geometric alterations resulting from the expansion.

In order to investigate the individual effects of the thermal expansion coefficient and the thermo-optic coefficient, simulations were conducted on the same device while setting one coefficient to zero at a time. Figure 4.6a presents a comparison of the resonance wavelength shift with temperature for these separate cases. It is observed that the thermal expansion coefficient and the thermo-optic coefficient exhibit opposite effects. By carefully designing the

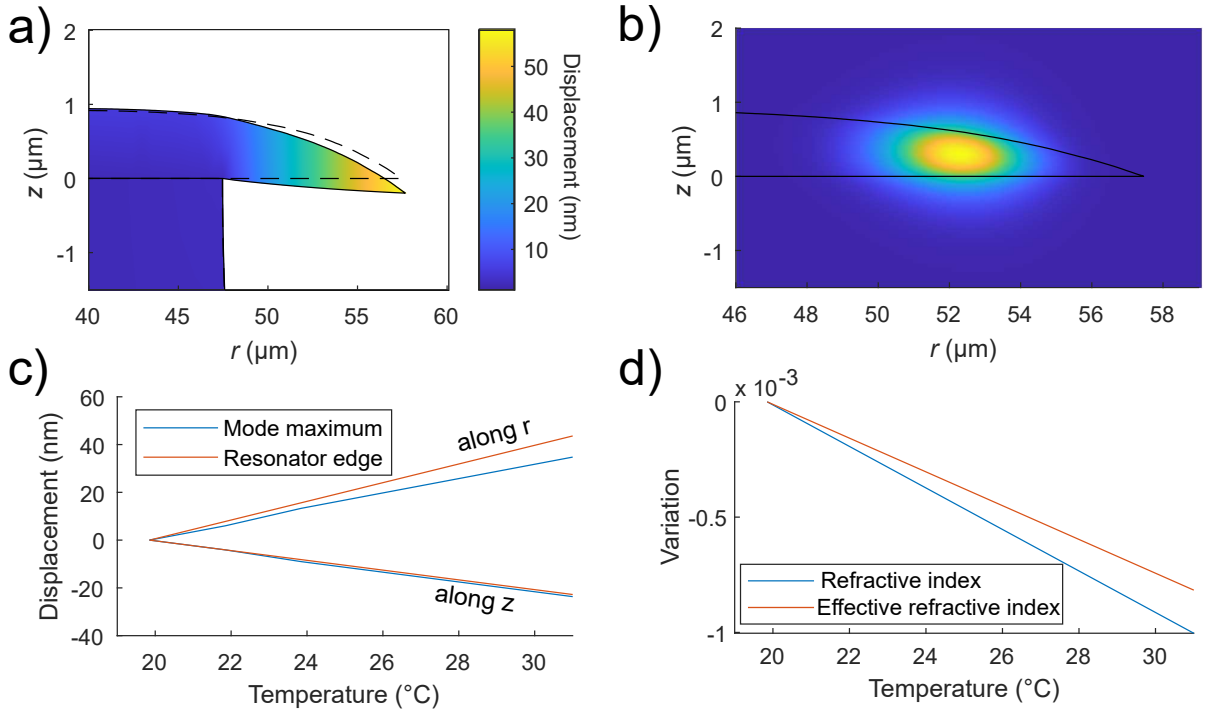

Figure 4.5 a) Simulated thermal expansion displacement field, with the displacement exaggerated by a factor of 5 for a temperature variation of 10 °C. b) Simulated optical mode, showcasing the electric field amplitude of the fundamental mode with the previous deformed resonator shape for a temperature variation of 10 °C. c) Displacement analysis of the mode maximum and drop edge along the r and z axes as temperature increases. d) Variation in refractive index change based on the thermo-optic coefficient and the effective refractive index with temperature.

device, these coefficients can counteract each other, resulting in a significantly reduced temperature sensitivity. However, when both effects are considered simultaneously, the combined contribution deviates from the simple summation of the effects obtained from individual simulations. This suggests that the two coefficients are not entirely linearly independent and may interact with each other in a more complex manner. For example, the expansion resulting from the thermal effects also impacts the effective refractive index of the system.

A previous study established a relationship between sensitivity to humidity for a rectangular disk [24] with a refractive index n, radius R, and undercut u. Drawing an analogy between humidity-related expansion $\left(\frac{\Delta\epsilon}{\Delta c}\right)$ and optical coefficients $\left(\frac{\Delta n}{\Delta c}\right)$ to thermal expansion $\left(\frac{\Delta\epsilon}{\Delta T}\right)$ and thermo-optic coefficients $\left(\frac{\Delta n}{\Delta T}\right)$, we can derive the thermal sensitivity (S) for the same disk as follows:

$$S = \lambda \left(\frac{\Delta\epsilon}{\Delta T} \frac{u}{R} + \frac{1}{n} \frac{\Delta n}{\Delta T} \right), \tag{4.1}$$

where λ represents the resonance wavelength. Notably, the thermal sensitivity exhibits a linear dependence with the ratio of the undercut to the radius (u/R). This relationship, however, may not hold true for drop-shape resonators due to their wedge profiles. Nevertheless, investigating the parameter u/R in our simulations provides valuable insights. Additionally, this relationship highlights the counteractive effects of the thermal expansion and thermo-optic coefficients. As the thermo-optic coefficient is negative, it is possible to choose an appropriate u/R value that cancels out both terms, resulting in a zero thermal sensitivity.

Such measurements were performed for various u/R ratios, and the wavelength shifts of different optical modes were tracked (Fig. 4.6b). It is observed that the sensitivity is more affected by the polarization than by mode numbers. Specifically, the transverse electric (TE) modes consistently exhibit a red shift, causing their resonance peaks to shift towards longer wavelengths for all investigated u/R ratios. On the other hand, the transverse magnetic (TM) modes demonstrate zero sensitivity at an u/R ratio of approximately 30 %. Below this threshold, their resonance peaks undergo a blue shift, indicating a shift towards shorter wavelengths as the temperature increases. Throughout the remainder of the simulation study, the fundamental TM mode is selected for analysis. This mode exhibits the highest quality factor, making it the preferred choice for tracking and analyzing the corresponding resonance peak with the experimental data.

Figure 4.6c presents a comparison between the simulation results and the experimental study. The sensitivities of the six fabricated devices, each with a different undercut, are reported with a linear regression. The trend observed in the experimental data aligns closely with the

simulation findings with a slightly different slope and a minor translation. The zero sensitivity point occurs around an u/R ratio of approximately 48 %. Several factors may contribute to the difference observed between the experimental and simulated results. These include potential errors in the measured thermal expansion and thermo-optic coefficients. Moreover, the microfabrication process itself can introduce variations in the polymer properties. Factors such as exposure to a vacuum chamber and plasma treatment during pillar etching can affect the mechanical properties of SU-8. Notably, the hardbake process of SU-8 has been identified as particularly influential in this regard [215, 216]. Despite these potential variations, the simulation used the values provided in the datasheet for the material properties. Additionally, measurements of the resonator profile, undercut, and pillar shape inherently involve uncertainties, which can contribute to deviations in the observed sensitivities. Nevertheless, both the experimental and simulated data demonstrate positive slopes and pass through a point of zero temperature sensitivity, indicating the presence of a critical u/R ratio.

An empirical linear relationship between the thermal expansion and thermo-optic coefficients has been observed in polymers [217]. The coefficients obtained through ellipsometry measurements in this study closely align with this relationship. Specifically, for a thermal expansion coefficient of 150 ppm/K, the measured thermo-optic coefficient is −90 ppm/K, which deviates slightly from the expected value of −84 ppm/K. However, the thermo-optic coefficient value reported in the literature does not follow this trend when compared to the thermal expansion coefficient provided in the datasheet, which should be −29 ppm/K instead of −180 ppm/K.

The undercut parameter plays a crucial role in engineering the thermal sensitivity of a polymer resonator on pillar. Due to the complex geometry of the structure, determining the optimal undercut value for achieving minimal temperature sensitivity through simulation alone becomes challenging. Furthermore, the polymer properties are influenced by the intricacies of the fabrication process, making it difficult to precisely extract the properties of a microdroplet deposited by inkjet. Therefore, employing an empirical characterization approach to study the thermal sensitivity of devices with varying the u/R ratio proves to be an effective method for identifying an undercut value that exhibits insensitivity to temperature. This approach significantly reduces the impact of thermal noise crosstalk and enhances the overall performance of the sensor.

This study focus on a resonator with a drop shape to explore the possibility to use inkjet printing to fabricate an optical sensor made of polymer. Previous work with a polymer disk made with photolithography [24] did explore the temperature sensitivity for a unique u/R ratio of 16.7 % with a radius of 60 µm. The measured temperature sensitivity is reported to

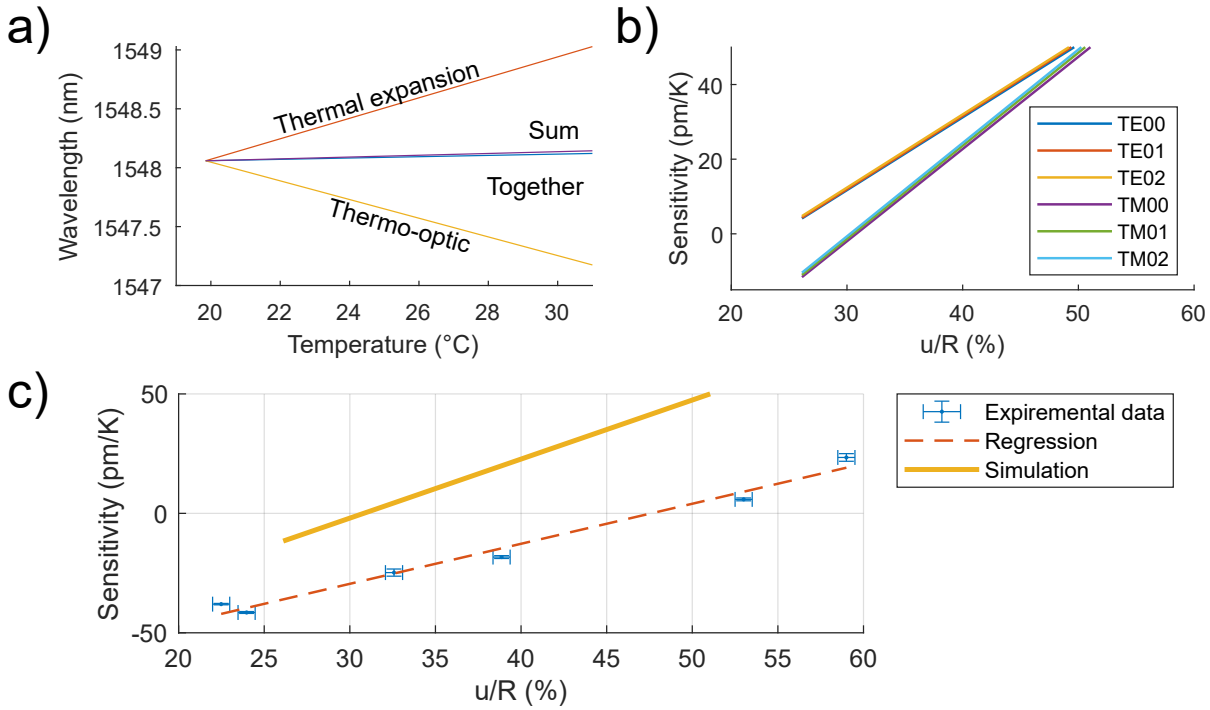

Figure 4.6 a) Study of the effect of both thermo-optic and thermal expansion coefficients on the resonance shift with temperature. b) Temperature sensitivity variation across u/R ratios for different modes of both TE and TM polarization. c) Comparative analysis between experimental results and simulation using measured coefficients.

be $-169.7\,\mathrm{pm/°C}$ which is much higher than what was reported for this study. It is closer to the simulation done with the literature values for the thermal expansion and thermo-optic coefficients. It is believed that the shape of the resonator impact the temperature sensitivity.

Although theoretically feasible to achieve complete temperature insensitivity with the suspended SU-8 resonator, uncertainties within the microfabrication process impose constraints on attaining the lowest possible temperature sensitivity. Experimentally, we managed to achieve a minimum temperature sensitivity of only $5.9\,\mathrm{pm/°C}$, representing over 28 times less sensitivity than the rectangular suspended SU-8 resonator [24]. In comparison, an SU-8 microcavity produced via inkjet printing and coated in PDMS [210] displays a temperature sensitivity of $-120\,\mathrm{pm/°C}$. For the latter case, given its attachment to the substrate, only the thermo-optic coefficient contributes to the sensitivity. In contrast to other polymer-based optical temperature sensors, our less sensitive resonator demonstrates sensitivity three orders of magnitude lower [218]. For instance, a silk fibroin microtoroid [219] showcases a temperature sensitivity of $1.17\,\mathrm{nm/°C}$.

Another approach previously reported to reduce the temperature sensitivity of a polymer-based optical resonator involves polymer annealing [76], resulting in a decrease of one order of magnitude (from $0.793\,\mathrm{nm/°C}$ to $0.068\,\mathrm{nm/°C}$). Through meticulous adjustment of design parameters, our approach achieves a comparable reduction in magnitude. Continued improvements in our technique hold the promise of achieving an even lower temperature sensitivity by enhancing control over the fabrication process.

Through the manipulation of the u/R ratio, precise control over the temperature sensitivity of the inkjet-printed optical resonator on pillar was achieved. This parameter allowed an insensitive sensor to temperature to be fabricated, as evidenced by the crossing of the temperature sensitivity through zero. By effectively mitigating the crosstalk between temperature fluctuations and the desired measured stimulus, the limitations imposed by the inherent temperature sensitivity of polymers were addressed. This ability to restrict and modulate temperature sensitivity is of great significance in the design of highly accurate and precise sensors.

4.7 Conclusion

The design approach employed in this study offers a convenient means of adjusting the temperature sensitivity of an optical resonator on pillar fabricated by combining inkjet printing technology and microfabrication. By adjusting the undercut, it becomes possible to achieve extremely low sensitivity to temperature fluctuations. Such insensitivity to temperature

minimizes crosstalk and enhances the sensor's precision in detecting other stimuli.

While this study primarily focused on investigating the influence of the u/R ratio on temperature sensitivity, other parameters can also be varied. For instance, the shape of the inkjet-printed droplet can impact the position of the resonant optical mode and, consequently, the effective refractive index. It is hypothesized that altering the shape, either by adjusting surface tension or by modifying the substrate and ink temperature during inkjet deposition, can affect the temperature sensitivity. Further research is required to explore these possibilities in more detail.

The u/R ratio is hypothesized to influence the sensitivity to various stimuli. This parameter, in conjunction with others, establishes a design space that necessitates exploration for effectively modulating the sensitivity to each stimulus. In cases where both the change in refractive index and thermal expansion exhibit an impact on sensitivity in the same trend, adjusting the u/R ratio can potentially enhance the sensitivity to that specific stimulus. A greater undercut allows for a larger region of the disk to undergo unconstrained expansion.

Finally, we have effectively addressed two key concerns associated with the polymeric whispering gallery mode resonator gas sensor. Employing drop-on-demand inkjet printing proved successful in fabricating the device, paving the way for the application of this fabrication technique to other polymers within the same microchip. Additionally, we propose a strategy to mitigate temperature cross-sensitivity through the optimization of a design parameter. This study systematically examines the dependence of temperature sensitivity on the u/R ratio, utilizing both experimental techniques and numerical simulations. By mitigating temperature sensitivity, we enhance the precision and expand the detection limits of our gas sensor.

This work represents an initial step towards a new sensing platform that combines polymer science with high-quality-factor optical resonators. The utilization of inkjet printing as an additive fabrication technique enables the integration of multiple polymers on a single chip, offering the potential for developing multiplex sensors. To fully realize this goal, further investigations into different polymer materials and the integration of resonators through coupling to optical waveguides are necessary. It is believed that this platform holds significant promise for various sensing applications, such as gas sensing.

CHAPTER 5 ARTICLE 2 - SUSPENDED WHISPERING GALLERY MODE RESONATORS MADE OF DIFFERENT POLYMERS AND FABRICATED USING DROP-ON-DEMAND INKJET PRINTING FOR GAS SENSING APPLICATIONS

The following chapter presents a comprehensive study on the application of inkjet-printed suspended polymer microresonators for gas sensing. This research published in Sensors and Actuators B: Chemical and titled "Suspended whispering gallery mode resonators made of different polymers and fabricated using drop-on-demand inkjet printing for gas sensing applications"[1] explores the potential of utilizing multiple resonators made from different polymers to achieve selectivity in gas detection. The majority of the work were done by the first author, Marc-Antoine Bianki which includes the design, fabrication, experimental measurements, analysis and the redaction. The co-authors helped with discussion, the experimental setup and the revision. Three distinct polymers – SU-8, polystyrene (PS), and polyhexamethylene biguanide (PHMB) – were employed to fabricate suspended whispering gallery mode resonators. These resonators were then exposed to various analytes, including isopropanol (IPA), water (H_2O), and carbon dioxide (CO_2), to evaluate their sensitivity and selectivity. The three devices are compared together and with the literature. The successful fabrication by inkjet printing and interrogation of these resonators is an important milestone in the conception of an optical nose. This work shows the feasibility of having resonators made of different polymers on the same optical chip. The article itself span over the sections 5.1 to 5.6. The section 5.7 contains the supplementary information that comes with this article.

Published April 26, 2024

5.1 Authors and Affiliations

Marc-Antoine Bianki[a,*],Régis Guertin[a],Cédric Lemieux-Leduc[a],Yves-Alain Peter[a]

[a] *Department of Engineering Physics, Polytechnique Montréal, Montréal, QC, H3T 1J4, Canada*

[1] M.-A. Bianki, R. Guertin, C. Lemieux-Leduc, and Y.-A. Peter, "Suspended whispering gallery mode resonators made of different polymers and fabricated using drop-on-demand inkjet printing for gas sensing applications", *Sensors and Actuators B: Chemical*, Dec. 2024, DOI: 10.1016/j.snb.2024.136460.

5.2 Abstract

Investigation of drop-on-demand inkjet printing as a fabrication method for an optical gas sensor reveals its potential to incorporate multiple sensing materials on a single microchip. Through this additive method, three distinct polymers—SU-8, polystyrene (PS), and polyhexamethylene biguanide (PHMB)—were deposited onto a silicon substrate and suspended, allowing the polymer microdroplets to expand freely. The coupling to these whispering gallery mode resonators with a tapered optical fiber allows measuring high quality factors exceeding 10^6. The gas sensing capabilities of all three polymers were studied for three different gases: isopropanol, water, and carbon dioxide. Sensitivities of up to 0.25 pm/ppmv and limits of detection as low as 14 ppmv were achieved.

Keywords - Gas sensor, Whispering gallery mode resonator, Drop-on-demand inkjet printing, Polymer.

5.3 Introduction

Today's microphones and cameras have surpassed human sight and hearing capabilities. In contrary, the human sense of smell remains unmatched by artificial counterparts. The human nose distinguishes between an astounding one trillion different odors [1] and detects small gas concentrations [220]. However, it falls short in quantifying gas concentrations due to its subjective nature and limitations in detecting certain harmful gases like carbon monoxide. Artificial gas sensors are imperative across various sectors including chemical industry, food production, healthcare, smart city, defense, and air quality monitoring [7, 17, 127].

Portable gas sensors stand as the most useful for their low cost and ease of use. They typically consist of a transducer and a sensing material. The electrical transducer methods encompass chemiresistors [49, 72], field-effect transistors [45], and capacitors [133]. Additionally, other transducers include acoustic [6] and optic [221] which are insensitive to electronic interference.

Sensing materials categorically encompass metal oxides, carbon nanotubes, and polymers [46, 48]. Polymers offer a distinct advantage due to their extensive variety, spanning thousands of synthesized variants [222], and they operate efficiently at lower temperatures. However, since they all absorb different gases, their selectivity towards one specific gas is limited. One approach to address this limitation involves utilizing an array of sensors, each incorporating distinct polymers [22, 44, 223].

Additive manufacturing methods present an excellent approach for integrating a variety of distinct sensing materials. For gas sensing applications, matrix-assisted pulsed laser evapora-

tion was employed to functionalize surface acoustic wave sensors with distinct polymers [54]. More specifically, printing techniques have been utilized to deposit a wide array of polymers to make gas sensors [127]. For instance, drop-on-demand inkjet printing has been effectively employed to functionalize chemiresistors with polystyrene [72] to measure ethanol and acetone vapor concentration.

The proposed design depicted in Fig. 5.1 a) involves the deposition of polymer microdroplets onto a silicon substrate, followed by curing and underetching to create a free-hanging edge for the microdroplet. This structure forms an optical resonator known as a whispering gallery mode (WGM) resonator. Here, the light becomes confined at the resonator's edge through total internal reflection. The sensing mechanism is based on the change of refractive index (Δn) and the change in the radius (ΔR) of the suspended polymer resonator when exposed to a gas as shown in Fig. 5.1 b). This causes the resonance peak to shift ($\Delta\lambda$) (Fig. 5.1 c)).

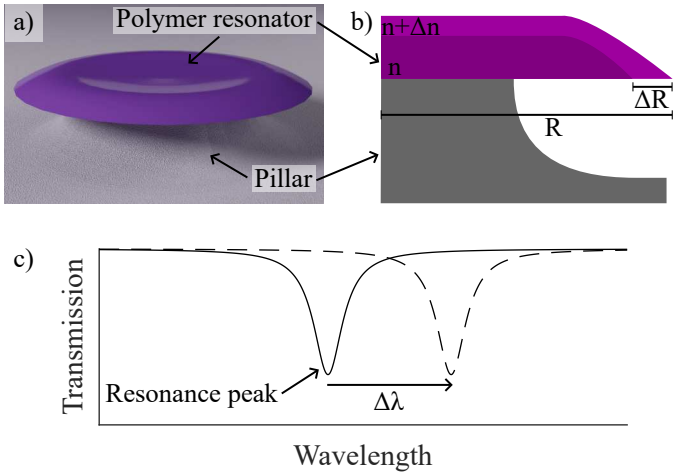

Figure 5.1 Working principle of a WGM-based gas resonator. a) Side-view model of a polymer resonator (purple) onto a silicon pillar. b) Sectional view of the resonator and the optical mode with representation of the changes in the refractive index (Δn) and in the resonator's radius (ΔR). c) Optical transmission spectrum illustrating the displacement of the resonance peak when exposed to a gas.

As an optical sensor, it can operate in environments prone to fire hazard and explosion such as in mines and in the petroleum industry. These sensors also offer the advantage of multiplexing. Additionally, the use of a polymer sensing material in optical sensors isn't confined solely to conducting polymers, unlike in electronic polymer-based sensors.

It has been shown that a suspended WGM resonator outperforms the Fabry-Perot interferometer (FPI) [24]. It is attributed to the unrestrained expansion of the WGM resonator's hanging section which differs from the limitations imposed by the FPI mirrors.

The selected additive method is drop-on-demand inkjet printing, known for its cost effectiveness, minimal material requirement, low ink volume, and energy efficiency [127]. Lasers and functionalized WGM resonators were made by this technique [25, 28, 224].

In this work, distinct polymers are used for the fabrication of optical resonators using inkjet printing such as SU-8, polystyrene (PS), and polyhexamethylene biguanide (PHMB). Previous demonstrations have established the printability of SU-8 [157] and PS [72]. Moreover, all three polymers have been utilized as sensing materials in gas detection studies [23,59,111]. A characterization of the devices is presented, and their gas sensing capabilities are thoroughly investigated. The performance of these devices is then evaluated in comparison to existing literature.

5.4 Material and Methods

5.4.1 Polymer Inks

Three different types of inks were employed for this study. SU-8 2000.5, obtained directly from Microchem, was used in its original state in cyclopentanone. Polystyrene, with a molecular weight of 35 000 was diluted in PGMEA (manufactured grade) both sourced from Sigma-Aldrich. PHMB, with a molecular weight of 213.33 from Matrix Scientific, was diluted in deionized water. Both were dissolved in their respective solvents and stirred magnetically for 30 min. Before printing, all three inks underwent filtration using a 13 mm syringe filter equipped with a 0.45 µm PTFE membrane.

Table 5.1 provides an overview of the general properties of the inks. Surface tension and viscosity information were obtained from literature for SU-8 ink [157] and were measured for PS and PHMB using contact angle and rheology measurement with details in the supplementary material sections S1 and S2 respectively.

5.4.2 Microfabrication

The fabrication process illustrated in Fig. 5.2 a) starts with a 4-inch silicon wafer ($\langle 100 \rangle$, p-type, 0-20 Ω). The surface undergoes dehydration and priming using hexamethyldisilazane (HMDS). Microdroplets of various polymer inks are deposited using an inkjet printer from Microdrop Technologies (MD-P-XYZ-C-E-12-09) (step 1). The printer employs a drop-on-demand piezoelectric head (MD-K-140) with a nozzle diameter of 100 µm. Inkjet printing parameters shown in Table 5.2 are adjusted accordingly for the three inks. Fig. 5.2 b) depicts a microdroplet of SU-8 being ejected from the Microdrop nozzle. Subsequently, the

Table 5.1 Polymer ink properties

Polymer	SU-8	PS	PHMB
Refractive index at 1550 nm	1.58	1.56	1.55
Solvant	Cyclopentanone	PGMEA	Water
Concentration (% w/w)	14.3	9.9	14.37
Density (g/mL)	1.07	0.98	1.01
Viscosity (mPa s)	2.664	5.14	2.7
Surface tension (mN/m)	37.7	33.4	61.5

SU-8 microdroplets undergo a softbake at 95 °C for 5 minutes, then UV flood exposure of 160 mJ cm^{-2}, and finally a hardbake at 95 °C for 5 minutes (steps 2 and 3). For PS and PHMB, the microdroplets were left to dry at room temperature for 3 hours (only step 2).

The underetching of the microdroplets is achieved using an inductively coupled plasma reactive ion etching (RIE-ICP) system with SF_6-chemistry (Oxford Instruments PlasmaLab ICP System 100). Fig. 5.2 c) shows a scanning electron microscopy (SEM) micrograph of the SU-8 resonator highlighted in purple on a silicon pillar.

5.4.3 Analytes

The three selected analytes are isopropanol (IPA), deionized water (H_2O), and carbon dioxide (CO_2). Their selection is based on their accessibility and distinctive traits, exhibiting the versatility of the approach.

Table 5.2 Inkjet printing parameters used for the three polymer inks

Polymer	SU-8	PS	PHMB
Voltage (V)	85	100	73
Pulse duration (µs)	25	20	28
Back pressure (mbar)	-16	-10	-45
Nozzle temperature (°C)	25	25	23
Substrate temperature (°C)	30	25	24

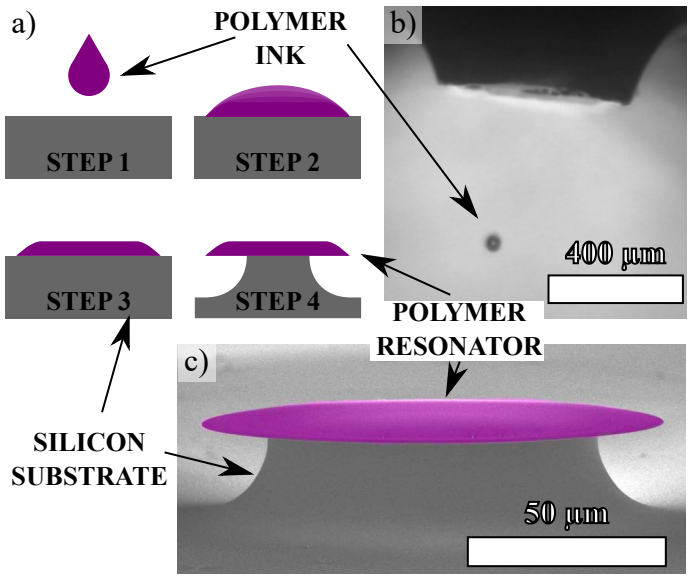

Figure 5.2 Microfabrication of a suspended microdroplet resonator a) Overview of the fabrication steps: Deposition of a polymer ink by inkjet printing on a cleaned silicon substrate (step 1). Solvent evaporation (steps 2) and optional UV curing (steps 3). Plasma etching of the substrate to underetch the microdroplet (step 4). b) An SU-8 microdroplet ejected from the inkjet nozzle. c) Scanning electron microscope micrograph of a final SU-8 resonator (highlighted in purple) on a pillar.

5.4.4 Gas Measurements

For the gas concentration sensitivity assessment of each polymer resonator, a gas setup (depicted in Fig. 5.3 a)) is employed. A 5-axis micro-stage precisely places the tapered optical fiber (TOF) utilized for coupling with the resonator.

The optical acquisition system is composed a tunable laser source (TLS - Keysight N7776C), a polarization controller (PC), and a photodetector (PD - Keysight N7745C). The TLS and the photodetector (PD) are synchronized to capture the optical transmission spectrum of the tapered optical fiber.

For the introduction of gases, nitrogen serves as the base of the gas mixture. To generate water and isopropanol alcohol vapors, nitrogen is passed through a bubbler containing these liquids maintained at constant temperature (18 °C). Carbon dioxide is sourced from a gas cylinder. Massflow controllers (MFCs) are employed to regulate both the gas sample's concentration and its total flow.

To ensure accuracy in measurements, temperature control is critical as these polymer resonators exhibit sensitivity to temperature variations [24]. Therefore, temperature regulation from previous work is used [225]. Both the thermoelectric controller (TEC) and the gas flow

are kept at 30 °C.

A gas measurement involves initial conditioning at the operational temperature and in a nitrogen environment for two hours. This step is crucial to purge the sensor from water and other unwanted species that might impact the sensor signal due to desorption. Following this, a sequence begins, alternating between blanks and gas samples of varying concentrations, each lasting one hour. Blanks of only nitrogen are used to correct for potential baseline deviation. One spectrum is recorded every 10 seconds, allowing for the tracking of each resonance peak over time. Fig. 5.3 b) depicts an example of gas measurement for an SU-8 microresonator and water vapors. The recorded shift of a resonance peak around 1554 nm is overlapped by the sequence of different concentrations in blue.

The mean peak position for each step is computed from the last 30 spectra collected within a 5-minute window. A peak shift indicates the disparity between the mean peak position of a gas sample step at a particular concentration and the mean peak position of the preceding blank step. Sensitivity is established through a linear regression correlating the peak shift against the gas concentration, as shown in Fig. 5.3 c). The limit of detection is computed as three times the signal noise relative to the sensitivity. Signal noise is obtained by calculating the mean noise across the blank samples.

5.5 Results and Discussion

5.5.1 Device Characterization

The optical microscope micrographs presented in Fig. 5.4 a) display the three fabricated resonators viewed from the top. In each image, two discernible circular edges are visible: the outer edge represents the resonator itself, while the inner edge delineates the pillar viewed through the polymer. They are denoted as r_r and r_p respectively on the figure. The resonator's radii measure approximately 50 µm (51.7 µm, 55.5 µm, and 48.0 µm for SU-8, PS, and PHMB respectively in Fig. 5.4 a)), corresponding to the nozzle opening radius, as expected. Depending on the ink properties and the printer parameters, radii from 48.0 µm to 83.3 µm is obtained through the different samples.

The undercut measures approximately 18.7 µm, 14.7 µm, and 15.0 µm in the same order of polymers. The undercut corresponds to the hanging part of the resonator that is free to swell and its value is controlled by the substrate etching time.

The profiles were obtained using a stylus profilometer before the pillar etching process. The radial profiles, extending from the center towards the outer edge, are depicted in Fig. 5.4 b). These profiles corroborate the observed radius values. Discrepancies between the optical mi-

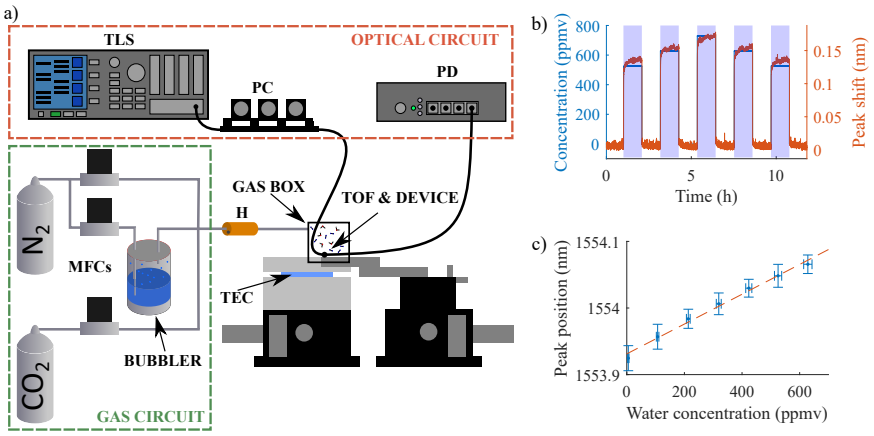

Figure 5.3 Gas measurement methodology. a) Measurement setup incorporating the optical circuit (tunable laser source TLS, polarization controller PC and photodetector PD), the gas circuit (gas cylinders, mass flow controllers (MFCs) and bubbler), temperature controllers (copper heater H, thermoelectric controller TEC) and the gas box (device and tapered optical fiber TOF). b) Measurement example demonstrating the tracking of a resonance peak around 1554 nm as concentration varies with time. c) Example of sensitivity regression for a humidity measurement. Both examples are from the suspended SU-8 microdroplet exposed to varying humidity concentration.

croscope images and the profiles result from uncertainties in the profile position and variations in microdroplet size during printing. Furthermore, the profile shape exhibits characteristics typical of the coffee ring effect, with a thinner profile at the center of the resonator and maximal thickness of approximately 1 µm near the resonator's edge [146]. By subtracting a fitted 6th order polynomial from the resonator edge, we can estimate the root-mean-square roughness near the optical mode to be 2.8 nm, 1.0 nm and 4.5 nm for SU-8, PS and PHMB respectively.

Figure 5.5 exhibits optical transmission spectra corresponding to each polymer's optical resonator. Polarization adjustments were optimized to attain the highest achievable quality factor for a particular resonance peak. This means to excite only one of the two polarization. Among these, PHMB demonstrates the lowest quality factor while PS presents the highest with 2.2×10^6. A discernible periodic pattern is evident across all spectra, allowing estimation of the free spectral range (FSR) by computing the average difference between peak positions within these patterns, specifically focusing on the highest quality factor resonance peak. Notably, the spectra showcase varying numbers of modes inside a single FSR: PS reveals more than 21 distinguishable resonance peaks, while PHMB presents no more than 5 resonance peaks. This disparity is influenced by two primary factors. Firstly, the superior quality factor of PS enables more modes with sufficiently high quality factors to be discerned. Secondly,

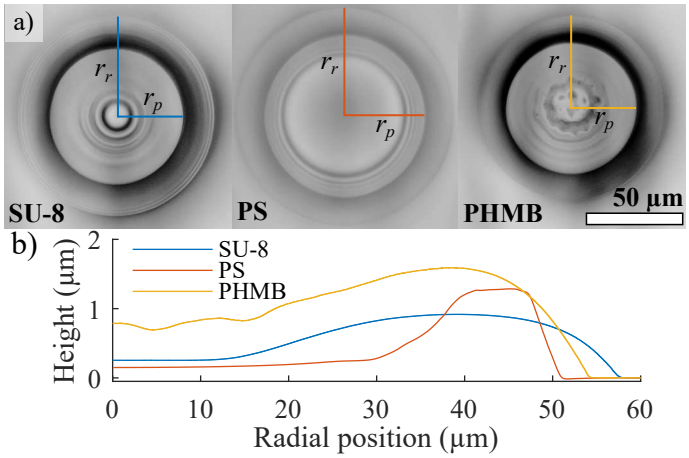

Figure 5.4 Geometric characterization of the resonators from the three polymers. a) Optical microscope micrographs indicating the resonator radius r_r and the pillar radius r_p. b) Radial profilometry of the polymer microdroplets from the center to the edge before the underetch step.

the drop profile and coupling dynamics impact the number of coupled modes. Adjusting the tapered optical fiber along the resonator's radius influences the coupling efficiency with each individual modes.

5.5.2 Gas Sensitivity

Gas sensitivity measurements were conducted for all polymer-gas pairs and the resulting peak shift versus concentration are presented with Fig. 5.6. The regression is found linear with a mean of regression residual error of less than 2 pm. The measured sensitivities are reported in Table 5.3 and are expressed as wavelength shift of a selected resonance peak (pm) per unit of analyte concentration (ppmv). Sensitivities display a range spanning two orders of magnitude, notably lower for carbon dioxide. This observation aligns with its saturated vapor pressure, which is three orders of magnitude higher than that of water and isopropanol. Across all three gases and among the polymers, SU-8 consistently exhibits the highest sensitivity, while PS consistently displays the lowest.

The sensing mechanism is based on the wavelength shift of a resonance peak when the resonator is exposed to an analyte [20, 24]. In steady state, the absorbed volume fraction of an analyte ϕ_a in a polymer will be in equilibrium through sorption process with the gas concentration (volume/volume) in air C_{air}. This equilibrium is described by the ideal gas law

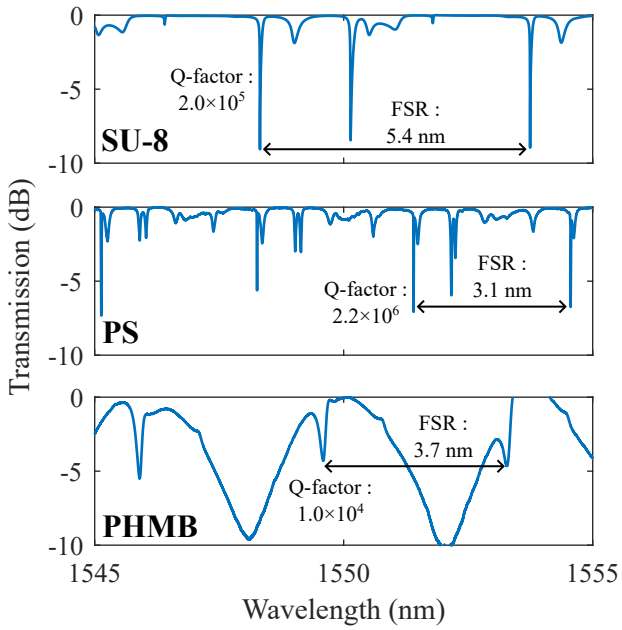

Figure 5.5 Examples of spectra obtained for the suspended microdroplets of the three distinct polymers, namely SU-8, PS and PHMB, along with the free spectral range (FSR) and the corresponding peak's highest Q-factor.

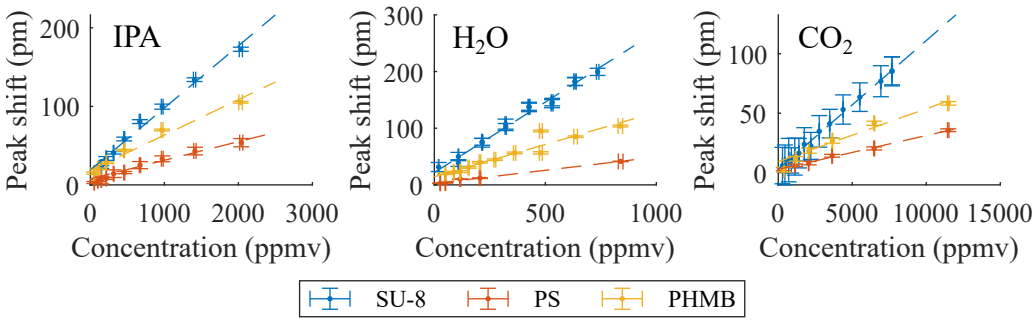

Figure 5.6 Resonance peak wavelength shifts versus analyte concentrations for every analyte-polymer pairs. Each graph is for a different analyte and contains three sets of measurements, one for each polymer. The dashed lines indicate the linear regressions used to obtain the sensitivities.

Table 5.3 Comparison among optical gas sensors utilizing polymer sensing materials. This study is highlighted in gray alongside three sensor types: whispering gallery mode (WGM) resonator, Fabry-Perot interferometer (FPI), and photonic crystal (PhC), all utilizing SU-8, PS, and PHMB polymers. Details include the wavelength range λ, sensitivity S, limit of detection (LOD), and the reached maximum concentration $C_{\max}$.

Analyte	Polymer	Sensor type	λ (nm)	S (pm/ppmv)	LOD (ppmv)	$C_{\max}$ (ppmv)	Source
IPA	SU-8	WGM	1545-1555	0.08	46	2000	This work
		FPI	1570-1610	0.07	-	-	[22]
		WGM	1559-1579	0.07	64	1577	[24]
	PS	WGM	1545-1555	0.03	217	2000	This work
		PhC	300-800	0.99	-	-	[59]
	PHMB	WGM	1545-1555	0.04	19	2000	This work
		FPI	1500-1600	0.55	-	-	[226]
H_2O	SU-8	WGM	1545-1555	0.25	44	840	This work
		FPI	1570-1610	0.20	-	-	[22]
		WGM	1530-1550	0.39	11	3530	[24]
		WGM	1529-1530	0.35	9	2189	[23]
	PS	WGM	1545-1555	0.05	25	840	This work
		PhC	300-800	0.33	-	-	[59]
	PHMB	WGM	1545-1555	0.11	14	840	This work
		FPI	1500-1600	0.44	-	-	[226]
CO_2	SU-8	WGM	1545-1555	0.01	1878	1350	This work
	PS	WGM	1545-1555	0.003	643	1350	This work
	PHMB	WGM	1545-1555	0.005	606	1350	This work
		WGM	1552-1554	0.46	-	700	[111]
		PhC	946-956	17.32	17	524	[61]
		FPI	1560-1570	12.20	-	700	[227]

and the partition coefficient $K_{p\text{–}a}$:

$$\phi_a = K_{p-a}\frac{PV_m}{RT}C_{air} \tag{5.1}$$

where P and T are the pressure and temperature of the gas, R is the ideal gas constant and V_m is the liquid analyte molar volume. The partition coefficient of the polymer-analyte pair is described by different models like the boiling point model, the solubility parameter model and the Linear Solvation–Energy Relationships (LSER) model [228].

The adsorbed gas induces an expansion of the resonator and a change in the resonator refractive index. For the case of a drop-shape resonator with a radius R, the wavelength λ_m of the m-th resonance with an effective refractive index n_{eff} can be approximated by the whispering gallery mode resonance condition $m\lambda_m = 2\pi R n_{\text{eff}}$. In the linear approximation, the wavelength shift $\Delta\lambda$ is related to the change in the resonator radius ΔR and the change in refractive index Δn:

$$\Delta\lambda = \lambda_m\left(\frac{\Delta n}{n_{\text{eff}}} + \frac{\Delta R}{R}\right) \tag{5.2}$$

Similarly to thermal expansion, the change in refractive index and volume expansion of polymer resonator will not necessarily be linear since the resonator has a complex geometry [225]. Moreover, the resonator is attached to the silicon pillar. It was shown that the sensitivity is proportional to the ratio between the resonator undercut and its radius [24].

The difference in sensitivities is then attributed to, among those things, the partition coefficient which is related to the difference in solubility parameters between polymers and analytes and the saturation vapor pressure and can be described by LSER model, the sensor geometry and the polymer mechanical properties like the Young's modulus and the Poisson's ratio [20, 24, 225, 229]. For glassy polymers, excess free volume needs also to be taken into account [230].

Another critical aspect of sensors is the limit of detection (LOD) reported in Table 5.3. Among the studied polymer sensors, a pattern similar to sensitivity emerges across the various analytes. Carbon dioxide consistently displays a higher limit of detection for all polymers, attributable to its lower sensitivity. However, an intriguing observation is the relationship between different polymer sensors measuring the same analyte, particularly concerning sensitivity. Polystyrene demonstrated lower sensitivity, while SU-8 exhibited the highest. Interestingly, the limit of detection for SU-8 isn't necessarily lower than that of PS. The distinction between sensitivity and the limit of detection arises from noise in the peak position over time. This noise may come from variation in temperature, pressure and coupling.

This highlights the importance of temperature control during these measurements, as well as the challenge in packaging due to the coupling with a tapered optical fiber.

For every step of concentration, a steady state is reached for the upward and downward transitions which indicates a reversible sensor for the total length of the measurements. The transient response of the sensor is presented in the supplementary material section S4.

5.5.3 Comparison and Discussion

The performance evaluation of the proposed design is contextualized alongside existing gas sensors based on optical resonators documented in the literature, employing similar polymer sensing materials like SU-8, PS, and PHMB (Table 5.3). These sensors can be categorized into three types: whispering gallery mode (WGM) resonators [23,24,111], Fabry-Perot interferometers (FPIs) [226,227], and photonic crystals (PhCs) [59,61].

Understanding the sensing mechanisms of these sensors is crucial. Many rely primarily on the alteration in refractive index, such as all the photonic crystal sensors and two of the whispering gallery mode sensors [23, 111]. In these instances, polymer swelling is significantly restricted. Regarding the FPI sensors, one allows free expansion [227], while the other is partially confined by flexible mirrors [226]. Finally, only the third whispering gallery mode resonator-based sensor features a similar underetch as the present work and allows swelling [24].

Another thing to consider is the wavelength range λ. Since these are all based on an optical wavelength shift, they scale with the resonance wavelength (eq. (5.2)). For instance, a sensor operating at 1500 nm would exhibit approximately 60 % greater sensitivity at 960 nm and about 145 % greater sensitivity at 632 nm. However, it does not significantly alter sensitivity comparisons across multiple orders of magnitude.

The performance achieved in this study is compared in Table 5.3 with other works using similar materials and analytes. The SU-8 resonator of this work exhibits sensitivity in the same order of magnitude as the literature to isopropanol (IPA) and water. In contrast, the PS resonator shows sensitivity approximately one order of magnitude lower compared to a photonic crystal sensor when detecting IPA and water [59]. Concerning the PHMB resonator, its sensitivity to water is similar to another study, yet, about one order of magnitude less sensitive to IPA when compared to the same FPI sensor [226]. For PHMB and CO_2, the present work exhibits two to four orders of magnitude lower sensitivity with other devices. However, the limit of detection is higher by only one order of magnitude instead of four. This suggests a more precise measurement of the peak position in this work. This is likely due to

varying environmental conditions. The other limit of detection values are all comparable to those reported in the literature. Another similar parameter is the maximum concentration obtained in each experiment, all within the same order of magnitude, without any observed saturation for any of them.

The unexpected low sensitivity of the PHMB resonator to CO_2 is intriguing. In this study and after inkjet deposition, a plasma etching of the substrate is required to suspend the edges of the devices. Prior studies on polycarbonate treated with SF_6 plasma exhibited decreased CO_2 permeability, potentially explaining the variance in sensitivity for PHMB and CO_2 [231]. Additionally, thermal baking of SU-8 on capacitive chemical sensors altered sensitivity [216] which is inevitable in the current process. An alternative explanation might lie in the detection mechanism. WGM and PhC sensors attribute wavelength shifts to refractive index changes. However, polymer swelling might also contribute, as noted in previous studies [20]. For PhC, since crystal dimensions are fixed, this effect is likely negligible. In the FPI sensor employing PHMB, the polymer is constrained by both mirrors. Conversely, in the present work, a significant portion of the PHMB can swell, potentially altering the resonator radius. For some polymers, this concurrent mechanism might enhance sensitivity if both radius and refractive index changes align. If CO_2 absorption by PHMB decreases the refractive index while the polymer expands, these two effects could counterbalance each other (eq. (5.2)). This implies that optimizing the resonator undercut could enhance sensitivity.

In this comparison, only two devices incorporate multiple polymers, both being manually filled FPIs. The drop-on-demand inkjet method employed in this study could potentially be adapted for use in functionalized photonic crystal sensors [59, 61] and one on-chip FPI [22]. Furthermore, the WGM microbubble and the optical fiber-based FPI are not chip-based devices and the other two WGM sensors rely on lithography and utilize spin coating, limiting them to photosensitive polymers. This fabrication method is restricted to one sensing material per chip. In contrast, the chip-based device developed in this work is fabricated using an automated additive manufacturing method, allowing the use of non-photosensitive polymers.

However, drop-on-demand inkjet printing requires polymers to be specifically suitable for this process. Drop-on-demand inkjet printing has particular demands regarding ink formulation [232]. Fortunately, various parameters can be adjusted to achieve a printable ink. For a particular polymer, modifications can be made to the polymer's molar mass and the solvent used. Additives such as surfactants can be introduced, and heating the ink can help fine-tune its viscosity.

For this specific application, not all the typical requirements are necessary. Higher surface tension, which might be required for other applications to ensure precise microdroplet forma-

tion, isn't as critical here since microdroplets don't need to form distinct lines. Moreover, the coffee ring effect, usually a concern in similar scenarios, doesn't pose a significant issue for the sensor since the optical mode resides at the resonator edge only. If needed, it can still be adjusted by controlling substrate temperature and ink composition [146]. Additionally, the microdroplet's contact angle with the substrate influences the optical resonance by shifting the mode radially [209]. In managing this phenomenon, the primary focus is adjusting the coupling position, achieved by manipulating the tapered optical fiber. Optimization can also occur through ink formulation adjustments and surface modifications [233].

One notable advantage of employing drop-on-demand inkjet printing lies in the resulting surface quality of the final resonator. During the drying process, surface tension works to smooth the resonator's surface, significantly minimizing one of the major optical losses affecting the quality factor in a resonator. We have successfully demonstrated a high-quality factor of 2.2×10^6 for the PS resonator.

All the polymers studied in this research exhibit sensitivity to every analyte investigated, indicating a lack of selectivity in this device which is described in the supplementary material section S3. However, as explored in a previous study involving a polymer-filled FPI resonator [22], by strategically combining polymers tailored for specific analytes, it becomes feasible to discern gas concentrations. This capacity can potentially extend to factors like temperature, pressure, and other variables. Consequently, an essential criterion for an effective sensor utilizing polymers as sensing materials is the existence of a multiplexing platform. The capability to deposit numerous distinct polymers onto a single chip becomes imperative. Through the integration of drop-on-demand inkjet printing of polymers and optical microdroplet resonators, this study presents a promising foundation for an efficient optical nose.

The current design requires full integration of the resonators to become a genuine multiplexing platform. Presently, light coupling with the microdroplet resonators relies on a delicate tapered optical fiber. Conducting experiments with individual polymers becomes intricate due to the need for positioning two multi-axis stages equipped with differential micrometers. This setup poses challenges for seamless integration. One potential solution involves vertically coupling the microdroplet with a photonic integrated circuit using standard microfabrication techniques, akin to the approach used for wedge disk resonators [234]. The primary challenge lies in precisely positioning the microdroplet above the underlying waveguide to ensure efficient coupling. By adopting this design, resonators crafted from different polymers could be integrated onto the same optical chip, facilitated by the additive fabrication technique of drop-on-demand inkjet printing.

5.6 Conclusions

This study serves as a proof of concept for an optical gas sensor employing polymer whispering gallery mode resonators created through drop-on-demand inkjet printing. The versatility of this manufacturing method was demonstrated by successfully fabricating resonators from three distinct polymers: SU-8, a photosensitive polymer, PHMB and PS, a soluble and an insoluble polymer in water respectively. The fabrication process was detailed, accompanied by a comprehensive optical characterization. Investigating this concept as a gas sensor involved assessing sensitivity and the limit of detection for three different analytes: IPA, water, and CO_2. Reported sensitivities reached as high as 0.25 pm/ppmv, with limits of detection as low as 14 ppmv, and these findings were compared to existing literature.

The suggested design appears promising in meeting the criteria for an artificial olfactory system, capable of detecting and discerning various gases. The vast array of printable polymers offers the potential for a versatile gas measurement platform with multiplexing capabilities.

The fabrication process utilizing drop-on-demand inkjet printing enables a diverse selection of sensing materials while ensuring the creation of resonators with high quality factors (10^6).

Further exploration into the sensing mechanisms is crucial, particularly focusing on the sensitivity of polymers to gases, understanding diffusion dynamics, swelling behaviors, and alterations in refractive indices. This exploration could aim to identify the most suitable polymers for specific applications and to fine-tune the optimal undercut with the goal to maximize the resonator performance.

Integrating the platform with a photonic integrated circuit is essential for transitioning this technology beyond the lab. Other areas requiring investigation include plasma treatment, thermal baking, and understanding the impact of the undercut on sensitivity. Beyond the gas sensor application outlined in this paper, this platform holds promise for measuring diverse parameters such as temperature and pressure. Additionally, leveraging functionalized polymers opens up opportunities for printing lasers and biosensors.

5.7 Supplementary Information

5.7.1 Surface Tension

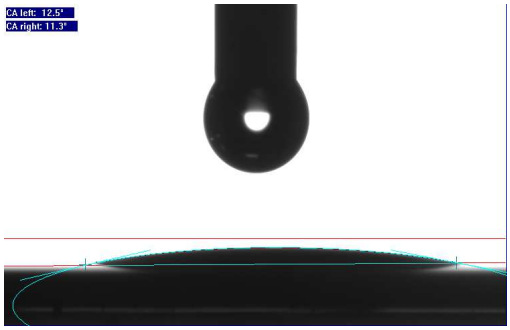

(a) PS on Si ⟨100⟩ substrate treated with a Piranha



(b) PS on Si ⟨100⟩ substrate coated with HMDS

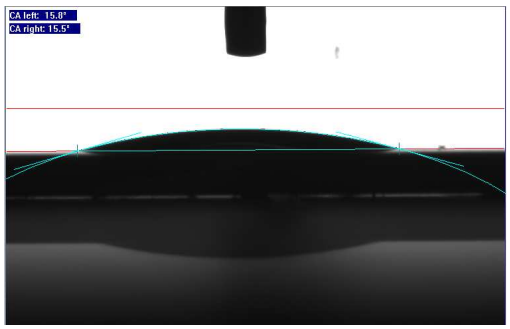

(c) PHMB on Si ⟨100⟩ substrate treated with a Piranha

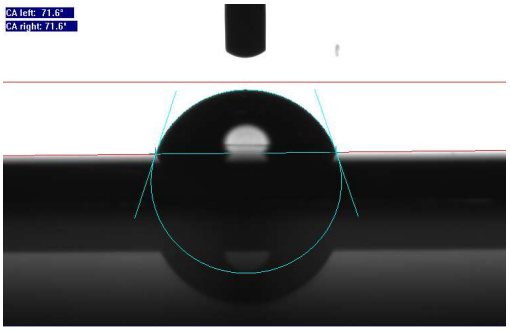

(d) PHMB on Si ⟨100⟩ substrate coated with HMDS

Figure 5.7 Optical contact angle measurements with instrument OCA-20 from Data Physics

Table 5.4 Measured contact angles for the determination of static surface tension of silicon ⟨100⟩ with a Piranha treatment or an HMDS coating as well as PS and PHMB inks

Liquid	Solid	Contact angle (°)
Water	Si ⟨100⟩, Piranha	27.7
	Si ⟨100⟩, HMDS	78.0
Ethylene Glycol	Si ⟨100⟩, Piranha	14.8
	Si ⟨100⟩, HMDS	48.9
Diiodomethane	Si ⟨100⟩, Piranha	42.5
	Si ⟨100⟩, HMDS	53.3
PS in PGMEA (9.9% w/w)	Si ⟨100⟩, Piranha	12.0
	Si ⟨100⟩, HMDS	12.6
PHMB in water (14.3% w/w)	Si ⟨100⟩, Piranha	15.0
	Si ⟨100⟩, HMDS	71.7

Table 5.5 Total static surface tension (SFT) of different liquids and solids with their dispersion (d) and polar (p) components. Values for water, ethylene glycol and diiodomethane are reported from the literature. Both silicon ⟨100⟩ solids with a piranha treatment and an HMDS coating were measured with the help of the three liquids. Both inks with PS and PHMB were obtained with the measured solids. The static surface tensions were calculated from the contact angles with the Owens, Wendt, Rabel and Kaelble method.

Material	State	SFT (mN/m)		
		total	d	p
Water	Liquid	72.1	19.9	52.2
Ethylene Glycol	Liquid	48.0	29.0	19.0
Diiodomethane	Liquid	50.0	47.4	2.6
Si ⟨100⟩, Piranha	Solid	59.5	15.7	43.8
Si ⟨100⟩, HMDS	Solid	34.1	26.1	8.0
PS in PGMEA (9.9% w/w)	Liquid	33.4	30.6	2.8
PHMB in water (14.3% w/w)	Liquid	61.5	18.3	43.2

5.7.2 Viscosity

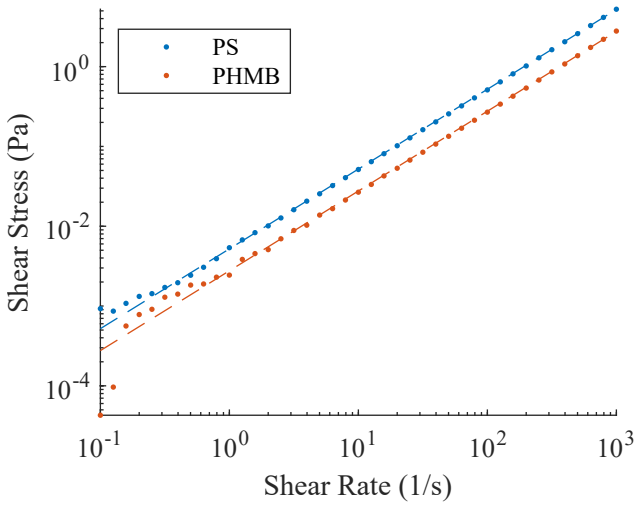

Figure 5.8 Viscosity measurement of PS and PHMB inks with linear regressions. The slope of the shear stress by the shear rate is the dynamic viscosity. The rotational viscometry measurements were made with the rheometer MCR 501 of Anton Paar with a double-gap spindle DG 26.7 at 25 °C.

5.7.3 Selectivity

Empirical selectivity assessment can be made by computing the selectivity angle between each polymer-analyte pair, calculated as:

$$R_{n,m} = \arccos\left(\frac{\left\langle \vec{S_n}, \vec{S_m} \right\rangle}{\left\|\vec{S_n}\right\| \left\|\vec{S_m}\right\|}\right) \tag{5.3}$$

where $\vec{S_n}$ and $\vec{S_m}$ are the selectivity vectors of the analytes n and m with the component of the vectors being the sensitivity of these analytes with each polymer.

The resulting angles serve as a measure of selectivity between two analytes. A measurement of $0°$ indicates that the two polymers are linearly dependent, rendering the selectivity null, while a measurement of $90°$ indicates that the two polymers are linearly independent, indicating perfect selectivity. These angles are detailed in Table 5.6 and fall within a range of a few degrees, indicating low selectivity for these three polymers.

Table 5.6 Selectivity angles for each pair of gases.

Gas pair	$R_{n,m}$ (°)
IPA - H_2O	7.83
IPA - CO_2	6.22
H_2O - CO_2	3.81

5.7.4 Response Time

Response times were evaluated for each polymer-analyte pair, measuring the normalized peak positions over time during a single transition from the nitrogen blank to the maximum analyte concentration. In Fig. 5.9, the normalized peak positions are depicted over time, with the change in gas concentration beginning at 0 min. Both the upward transition (from blank to maximum concentration) and the downward transition (from maximum concentration to blank) are illustrated. Two criteria, namely 70 % and 90 % of the total wavelength shift over 60 min, are marked by dashed and dash-dotted vertical lines, respectively, in colors corresponding to the analyte. The overall trend in response time predominantly aligns with the specific polymer and remains similar to the same polymer with different analytes. Consequently, the t_{70} lines closely cluster together, while the t_{90} lines exhibit slightly more spread. Details of the response times are presented in Table 5.7, revealing that SU-8 exhibits the quickest response time, achieving less than a minute for t_{70}.

The different order of magnitude between the two response time definitions, t_{70} and t_{90} suggests the presence of multiple response regimes. Previous research on the response time of polymer swelling to gas concentration changes has indicated an empirical relationship resembling the summation of two exponential functions, each with different time constants. This model has been applied in the study of materials like polydimethylsiloxane (PDMS) [82] and has been fitted to SU-8 as well [24] and might explain the initial rapid response of PHMB to water vapors, surpassing that of PS (2.5 min>11.8 min), followed by a slower response thereafter (33.5 min<24.7 min).

Since both the downward and upward response times are below 40 minutes, it is confirmed that the sensor has a reversible response at room temperature.

The wavelength shift in time $\Delta\lambda(t)$ can be fit with a two-exponential model where there is a fast and a slow response time with constant τ_1 and τ_2 respectively and $\tau_1 < \tau_2$. The fit equation is:

$$\Delta\lambda(t) = C_0 \pm H(t - t_0)\left(C_1\left(1 - e^{-\frac{t-t_0}{\tau_1}}\right) + C_2\left(1 - e^{-\frac{t-t_0}{\tau_2}}\right)\right) \tag{5.4}$$

for upward (plus sign) and downward (minus sign) where $H(t)$ is the Heaviside function, C_1, C_2 and C_0 are proportionality constants and t_0 is the time when the change in concentration occurs. The relative importance of each exponential is given by the ratio between C_1 and C_2.

The three polymers were analyzed with the three analytes. The model fits all experiments well for both upward and downward transitions ($R^2 > 0.977$).

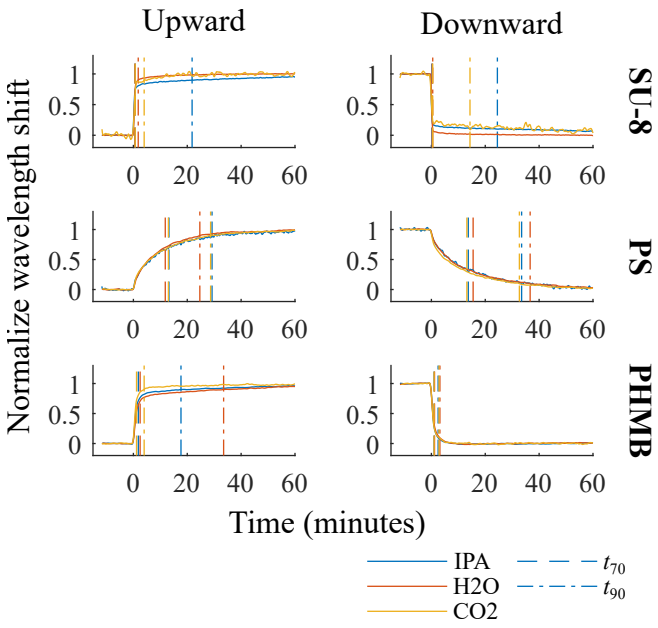

Figure 5.9 Transient response curves for each polymer-analyte combination, displaying both upward and downward transitions. The response times at 70 % and 90 % of the overall wavelength shifts are indicated by dashed and dash-dotted vertical lines respectively, matching the color code of the corresponding analyte.

Table 5.7 Response times in minutes for both upward and downward transitions, representing 70 % and 90 % of the maximum wavelength shift for each combination of polymer-analyte pairs.

		t_{70} (minute)			t_{90} (minute)		
		IPA	H2O	CO2	IPA	H2O	CO2
UP	SU-8	0.6	0.6	0.7	21.8	1.8	4.0
	PS	13.2	11.8	13.0	29.2	24.7	28.7
	PHMB	1.8	2.5	1.2	17.7	33.5	4.0
		IPA	H2O	CO2	IPA	H2O	CO2
DOWN	SU-8	0.2	0.3	0.5	24.5	0.5	14.3
	PS	13.7	15.5	13.2	33.5	36.7	32.7
	PHMB	1.0	1.2	1.0	2.5	3.2	2.8

Table 5.8 Fit results of the sum of two exponential terms for upward and downward transition of each polymer-analyte pair. τ_1 and τ_2 are the fast and slow time constants, R^2 is the coefficient of determination of the fit, and ratio is defined as C_1 divided by C_2.

Polymer	Analyte	Upward				Downward			
		τ_1 (s)	τ_2 (s)	ratio	R^2	τ_1 (s)	τ_2 (s)	ratio	R^2
SU-8	H_2O	10.3	560.8	7.88	1.000	6.0	935.2	19.92	0.999
	IPA	9.5	2550.9	4.67	0.999	6.0	4664.6	5.94	0.999
	CO_2	10.0	521.9	5.30	0.977	10.0	3760.8	4.16	0.975
PS	H_2O	202.8	827.5	0.48	0.999	168.8	1179.1	0.52	0.999
	IPA	167.9	1018.2	0.52	0.991	83.9	1019.5	0.32	0.991
	CO_2	71.1	871.1	0.34	0.999	64.1	977.9	0.44	0.999
PHMB	H_2O	53.1	2353.3	3.33	0.999	19.0	111.1	0.97	0.999
	IPA	44.3	2282.5	4.67	0.999	17.6	102.0	1.35	0.999
	CO_2	33.0	1344.7	8.75	0.997	16.0	118.9	1.56	0.998

CHAPTER 6 ON-CHIP VERTICAL INTEGRATION OF POLYMER RESONATORS FABRICATED BY INKJET PRINTING

6.1 Introduction

In preceding chapters, the potential of inkjet-printed suspended polymer microresonators as gas sensors was established. The unique fabrication method enables the integration of resonators composed of various polymers onto a single optical chip, offering enhanced selectivity. Nevertheless, the current approach of utilizing a tapered optical fiber for coupling presents several limitations. The delicate nature of the tapered fiber, with a diameter of only 2 micrometers, necessitates the use of complex 5-axis stages with micropositioners, rendering it impractical for field-based applications. While the coupling factor can be readily adjusted, the fragility of the tapered fiber remains a significant obstacle to widespread deployment. Furthermore, this approach for coupling and packaging the resonators is complex and not well-suited for mass production, especially when integrating multiple polymer resonators onto a single chip. This limitation significantly impedes the development of devices with improved selectivity.

Thus, it is proposed to use vertical coupling with a waveguide from a photonic integrated circuit (PIC). In this chapter, the integration of suspended polymer resonators made by combining inkjet printing and microfabrication is investigated.

6.1.1 Problematic

Bottom Cladding

As part of this work, the optical resonators are fabricated from polymers, which generally exhibit lower refractive indices than silicon nitride commonly used in PICs. Figure 6.1 illustrates the distribution of refractive indices for polymers at a wavelength of 632 nm, based on data from the "Physical Properties of Polymers Handbook" by J.E. Mark [235]. Since there is typically no optical absorption mechanisms in dielectric polymers in-between 632 nm and 1550 nm, we can assume that the refractive index will only be a slight amount lower than what is shown due to the dispersion. The majority of polymers in this distribution has a refractive index between 1.46 and 1.56, with some as low as 1.34.

By considering the refractive index of the polymer and the resonator's droplet shape, we can calculate the effective refractive index of the optical resonance mode. This analysis

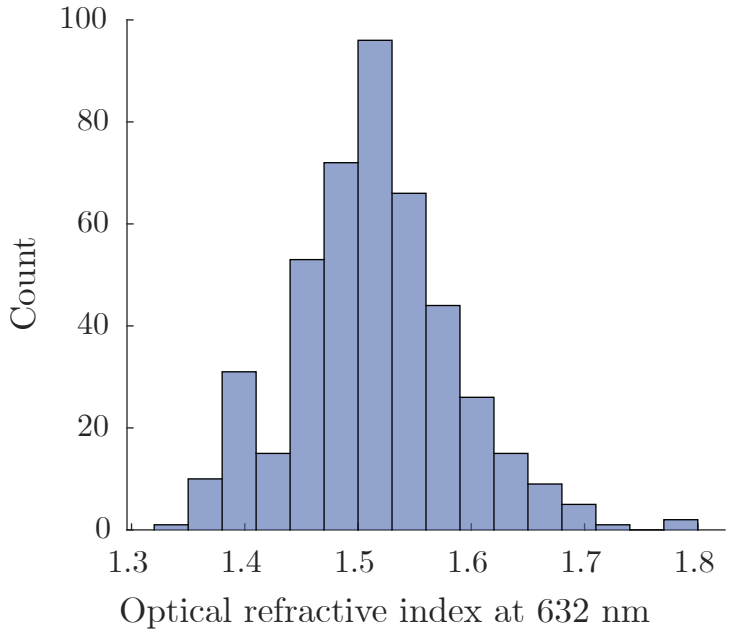

Figure 6.1 Refractive index distribution of polymers at 632 nm (data from [235])

was performed for the three polymers investigated in the second article: SU-8, polystyrene (PS), and polyhexamethylene biguanide (PHMB). Given that the other modes exhibited comparable sensitivity but lower effective refractive indices and quality factors (as reported in the first article), we focused on the TE0 mode for further analysis. The calculated modes are depicted in Figure 6.2, with effective refractive indices of 1.39, 1.42, and 1.42 for SU-8, PS, and PHMB, respectively. Since these values are all lower than the refractive index of silica (1.45), placing the resonator in close proximity to a silica substrate can lead to optical mode leakage, resulting in a decrease in the quality factor. It is important to note that the three examined polymers in this study have refractive indices (1.56) higher than the average refractive index (1.51) in the previously presented distribution.

Figure 6.3 illustrates this phenomenon for an SU-8 resonator. The optical resonance mode was calculated for varying distances from a silica substrate and the effective refractive index and the quality factor were extracted (Fig. 6.3(a)). When the resonator is far from the substrate, the simulated quality factor is significantly higher than experimental expectations (1×10^7). This discrepancy can be attributed to the exclusion of absorption and scattering in the simulations, which only considered radiation. Notably, the effective refractive index plateaued at 1.38, similar to the case without a substrate. However, as the resonator approaches the substrate, the optical mode begins to leak into it, as depicted in Figure 6.3(b). This leakage results in a significant decrease in the quality factor, which correlates with the reduction in

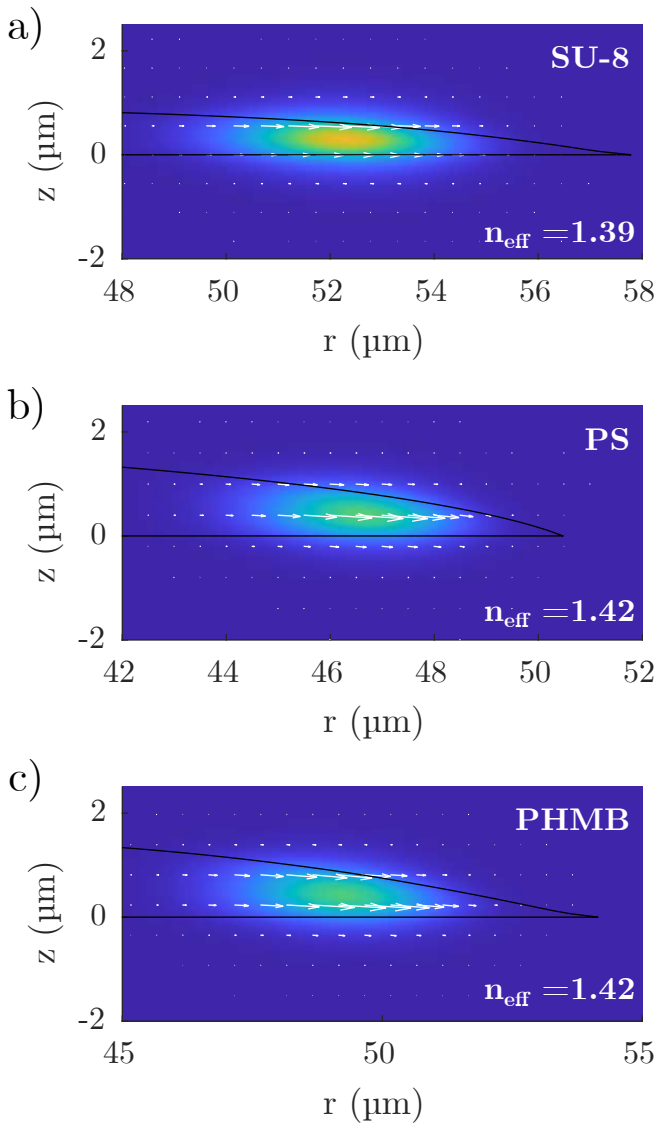

Figure 6.2 TE0 optical resonance modes of polymeric droplet resonators fabricated from a) SU-8, b) PS, and c) PHMB, with calculated effective refractive indices (n_{eff}). The color scale represents the electric field amplitude, and the white arrows indicate the radial and axial components.

effective refractive index.

6.1.2 Possible Solutions

The on-chip optical coupling design must be compatible with a suspended resonator to allow for the polymer expansion.

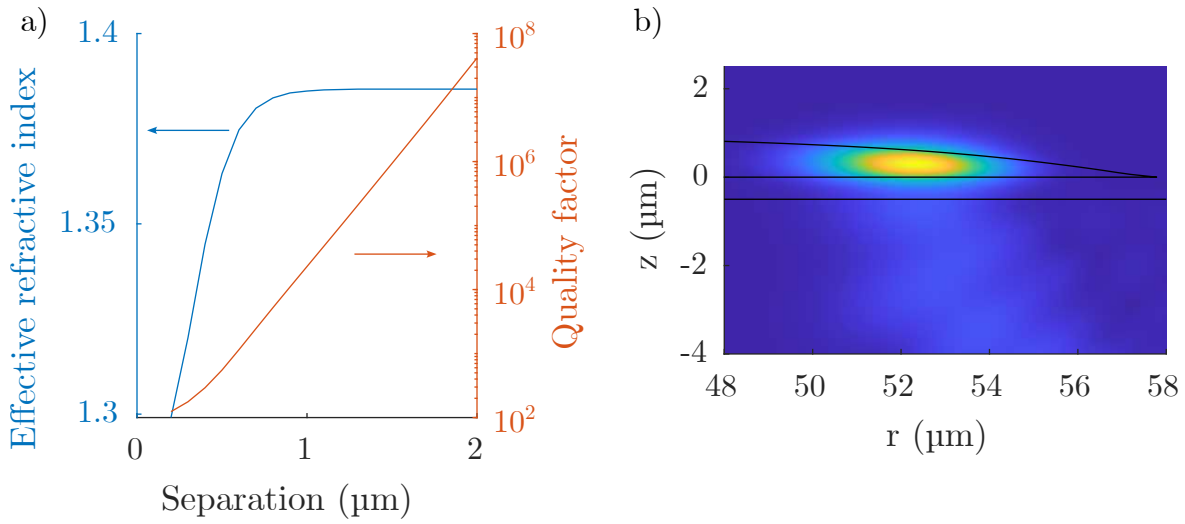

Figure 6.3 a) Effective refractive index and quality factor of an SU-8 resonator as a function of its distance from a glass substrate. b) Visualization of optical mode leakage from the SU-8 resonator into the glass substrate for a separation of 0.5 µm.

Glass can still be employed as a bottom cladding for high-refractive-index polymers. We determined the fraction of suitable polymers by calculating the effective refractive index for a resonator with the same geometry as the SU-8 resonator but with varying polymer refractive indices. The results and a linear regression are presented in Figure 6.4 a). For a glass substrate, the effective refractive index must exceed 1.45. This value can be achieved, for this specific resonator shape, with a polymer refractive index of 1.65. Referring to Figure 6.1, this corresponds to approximately 3 % of the polymers.

To ensure compatibility with the glass substrate, the resonator shape can be engineered to minimize the difference between the effective refractive index and the polymer refractive index. In the absence of drying effects like the coffee ring effect, a sessile drop assumes a shape governed by the Young-Laplace equation. For small resonators (less than a millimeter), the Bond number, a dimensionless parameter comparing gravitational forces to surface tension, is low ($Bo = \Delta\rho g L^2/\gamma << 1$). This results in a spherical cap shape for the drop. Numerical calculations of the effective refractive index for droplet resonators with a spherical cap shape and various polymer refractive indices (n_p) were conducted. Figure 6.4 b) illustrates the difference between the effective refractive index (n_{eff}) and the polymer refractive index (n_p) as a function of the contact angle. The effective refractive index is consistently lower than the polymer refractive index, with this difference being more pronounced at smaller contact angles. While the polymer refractive index influences the final effective refractive index, it does not affect the dependence on the contact angle.

Glass substrates can still be used with polymers having refractive indices greater than 1.5 for large contact angles (>45°), which represents over half of the polymers (57 %) in Figure 6.1. However, this proportion may be lower in the infrared (1550 nm) due to the fact that the refractive index distribution in Figure 6.1 is based on visible light (632 nm). The contact angle can be engineered by modifying the surface tension of either the ink or the substrate. For the ink, the solvent can be replaced with a compatible alternative, the concentration can be adjusted, or a surfactant can be added. For the substrate, surface modification treatments can be applied. Additionally, the coffee ring effect can be controlled by adjusting the substrate temperature during printing [146].

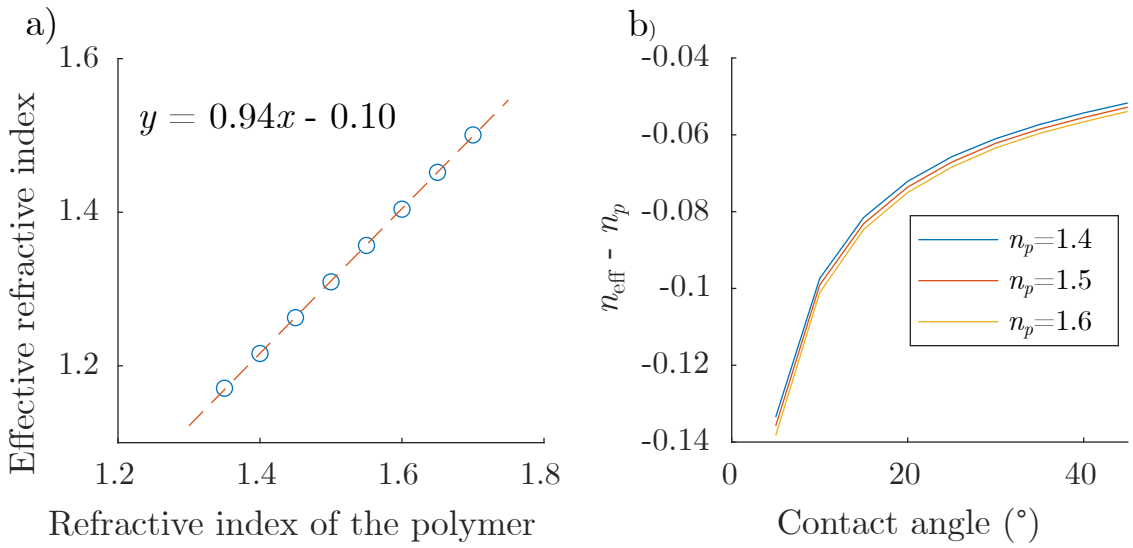

Figure 6.4 a) Effective refractive index of a suspended polymer resonator similar in shape to the SU-8 resonator as a function of the polymer's refractive index. b) Difference between the effective refractive index and the polymer refractive index for a spherical cap resonator plotted against the contact angle for three different polymer refractive indices. Both graphs were obtained by numerical calculation.

However, this last solution may still limit the range of suitable polymers for sensor applications. Therefore, exploring alternative substrates is essential. Table 6.1 presents the refractive indices of several candidate materials. For comparison, the table also includes common materials used in silicon photonics (Si, SiN, SiO_2) and the polymers (SU-8, PS, PHMB) used to fabricate suspended resonators presented in this thesis. Beside the refractive index, the bottom cladding must be compatible with the subsequent steps of the fabrication process.

Given that the resonator is already suspended, air could be considered as a potential waveguide cladding. Air has a refractive index of 1.00. The use of air as a cladding has been

Table 6.1 Refractive indices at a wavelength of 1550 nm for various materials

Material	Refractive index	Note	Source
α-Si	3.48		[236]
SiN	1.9904	PECVD	[237]
Al_2O_3	1.6214	Reactive sputtering	[238]
SiO_2	1.4657	Magnetron sputtering	[239]
CaF_2	1.4261		[240]
MgF_2	1.4172	Evaporation	[241]
SU-8	1.58		[211]
PS	1.5646		[242]
PHMB	1.56		[63]
PMMA	1.4717		[243]
PDMS	1.3892	5:1 ratio	[243]
CYTOP	1.34	Fluoro polymer	[244]
Teflon AF	1.29	Fluoro polymer	[245]
Porous silica	1.002-1.46		[246, 247]
Air	1.00		

demonstrated with SU-8 waveguides [248] which were used to couple with whispering gallery mode resonators [249]. Additionally, a gas sensor based on mid-infrared absorption was fabricated using a suspended silicon waveguide. However, this type of structure is prone to buckling [186]. Mechanical robustness can be enhanced by employing a suspended slot waveguide [250].

Alternative inorganic materials could be considered as a substrate to replace glass. The lowest refractive index available materials are MgF_2 and CaF_2 with refractive index of 1.42 and 1.43 respectively. While these values are significantly higher than air, they are not substantially lower than the refractive index of silicon dioxide.

Polymers offer a diverse range of refractive indices, making them suitable for various applications. Polydimethylsiloxane (PDMS), with a refractive index of 1.39, is a commonly used polymer cladding material for SU-8 waveguides [251]. Polymethylmethacrylate (PMMA) is another transparent polymer with a low refractive index of 1.47 [243]. Fluoropolymers, such as commercially available CYTOP and Teflon AF, exhibit the lowest refractive indices among polymers, with values of 1.34 and 1.29, respectively. A PMMA-core waveguide fabricated on a CYTOP cladding has been demonstrated [252].

Porous materials, characterized by their porosity P (the volumetric percentage of air), offer a promising avenue for achieving low refractive indices due to their air-material composition. By employing an effective medium approximation such as the Bruggeman formula, the effec-

tive refractive index can be expressed as a function of porosity and the refractive indices of air (n_1) and the bulk material (n_2):

$$P\frac{n_1^2 - n^2}{n_1^2 + 2n^2} + (1 - P)\frac{n_2^2 - n^2}{n_2^2 + 2n^2} = 0 \tag{6.1}$$

Thus, the effective refractive index of porous materials can vary between the refractive indices of the constituent material and air.

Another important parameter is pore size which can be classified between macropore (larger than 50 nm), mesopore (between 2 nm and 50 nm) and micropore (pores smaller than 2 nm). The pore size can also be a distribution of sizes.

Porosity in materials can be achieved through various fabrication techniques [247]. For porous silicon, common methods include anodization etching, galvanic etching, metal nanoparticle-assisted etching, photoetching and vapor etching. Porous silica, on the other hand, can be synthesized by either oxidizing porous silicon or employing aerogel or xerogel processes.

Porous silicon and porous silica waveguides, fabricated through anodization etching and subsequent oxidation, have potential applications in photonics. By adjusting the porosity of the cladding to be higher than the core, a refractive index difference is achieved, resulting in losses of 0.5 dB/cm for porous silicon [253] and 20.4 dB/cm for porous silica [254]. The effective refractive index of the waveguide mode in both materials is significantly lower than that of bulk silicon dioxide, at 1.238.

Aerogels and xerogels are porous silica materials synthesized through chemical reactions involving silicon-containing precursors. These precursors, such as sodium metasilicate (Na_2SiO_3) also called waterglass, tetraethoxysilane (TEOS), tetramethoxysilane (TMOS), methyltrimethoxysilane (MTMS) undergo hydrolysis and polycondensations to form a 3D silica network [246]. The choice of precursors, catalysts, and processing conditions influences the final properties of the material. Aging and drying processes are crucial steps in determining the porosity and structure of the resulting aerogel, xerogel, or cryogel. Aerogels, synthesized using supercritical drying, exhibit the highest porosity due to the avoidance of capillary stress. Xerogels are obtained through evaporation drying, while cryogels are produced using freeze-drying. These techniques can be adapted for microfabrication by spin-coating sol-gel solutions onto substrates, yielding thin films of porous silica with exceptionally low refractive indices (e.g., 1.8 µm, $n = 1.05$) [255].

In photonics, aerogel has been employed as the core of optical fibers, demonstrating losses below 0.3 dB/cm [256]. Additionally, silica xerogels have been micromachined using femtosecond lasers to create optical waveguides with losses of 2.9 dB/cm [257]. Furthermore,

xerogels have been utilized as the bottom cladding in plasma-enhanced chemical vapor deposition (PECVD) silicon dioxide planar waveguides, achieving losses of 1.4 dB/cm at 830 nm [258].

Mechanical properties like stiffness and hardness of porous materials are reduced compared to the bulk. This could cause problems during the microfabrication process. However, it has been shown that aerogel is structurally resistant by making a suspended cantilever [259].

While porous materials offer the potential for low-loss optical waveguides, understanding the impact of porosity on optical performance is essential. Optical losses in waveguides arise from various sources, including bulk absorption and surface scattering. Porosity will add a source of volume scattering α_{vscat} since each pore will scatter the incoming light. A mathematical model based on Rayleigh scattering has been developed to estimate this scattering coefficient in silicon dioxide on xerogel waveguides [260]. The model considers the porosity P, the pore radius r, the wavelength λ and the effective refractive index of the porous material n :

$$\alpha_{\text{vscat}} = 17.36\pi^4 \frac{(2r)^3}{\lambda^4} \left(\frac{n^2-1}{n^2+2}\right)^2 P \tag{6.2}$$

In this equation, the term $((n^2-1)/(n^2+2)))^2$ varies between 0.44 to 0.57 for materials with refractive indices ranging from air to silicon dioxide. Since the porosity P is bound between 0 and 1, the dominant factor influencing scattering loss is the ratio of the pore radius (r) cubed to the wavelength (λ) to the fourth power ($(2r)^3/\lambda^4$). Thus, for a fixed working wavelength (e.g., 1550 nm), minimizing pore size is crucial to reduce scattering losses.

6.2 Proposed Designs

All proposed designs incorporate a fixed, low-refractive-index bottom cladding ($n = 1.3$) spin-coated on a silicon substrate that only serves as a support. Over this layer is the waveguide. For the structure, ridge and rib waveguides are investigated. The latter has the advantages of protecting the bottom layer from subsequent steps. Since an air gap is necessary between the resonator and the polymer to allow for expansion, the upper cladding is air.

To fabricate the waveguide, we explore several materials commonly used in silicon photonics: silicon ($n = 3.45$) and silicon nitride ($n = 2.1$). We also consider silicon dioxide ($n = 1.45$) and SU-8 ($n = 1.58$) due to their easier fabrication, transparency, and lower refractive index. All designs are optimized for a working wavelength of 1500 nm.

To support the resonator, a sacrificial material is deposited atop the waveguide before the resonator is printed. This material is then isotropically etched to form a pillar and release the

resonator's edge. This etching process must selectively target the sacrificial material while preserving the waveguide, resonator, slab (if applicable), and bottom cladding. Depending on the waveguide thickness and sacrificial material deposition method, a planarization step may be required. Potential sacrificial materials include silicon (deposited by sputtering and etched with a SF_6 plasma), silicon dioxide (deposited by sputtering or spin-on-glass (SOG) and etched with vapor HF), and a polymeric material like LOR 5A resist (deposited by spin coating and wet etched).

A significant challenge in vertically stacking photonic structures is achieving a flat surface before depositing subsequent layers. Planarization techniques, such as chemical-mechanical polishing (CMP), spin coating (including SOG), and reflow, can be employed to address this issue. The choice of technique depends on the specific materials involved and the desired surface roughness.

For some designs, a liquid-based etch process is considered for the sacrificial layer. However, this approach can lead to the resonator collapsing onto the waveguide and substrate due to surface tension during the drying of the wet etchant. Since the separation between the resonator and waveguide should be only a few hundred nanometers, critical point drying is necessary for these designs. This may limit the compatibility of certain polymers with the platform. It's worth noting that other sacrificial layer etching techniques can also potentially damage the polymer resonators. Currently, we know that SU-8, PS, and PHMB are compatible with SF_6 plasma etching.

To resume the proposed design, a general process flow is illustrated with Fig. 6.5. The process begins with a clean silicon wafer, selected for its mechanical properties and familiarity in microfabrication (Step 0). The bottom cladding material is then deposited using a suitable technique to ensure sufficient thickness for confining the waveguide optical mode away from the silicon substrate. Next, the waveguide material is deposited and patterned to create the photonic integrated circuit. A sacrificial material is subsequently deposited and planarized. The polymer microdrop is then inkjet-printed, aligning with the photonic integrated circuit. Finally, the sacrificial layer is etched to form pillars and suspend the resonator's edge.

6.3 Methodology

To compare the various designs, we numerically optimized coupling and the quality factor using coupled-mode theory. Due to the weak coupling and its computational efficiency, coupled-mode theory was a suitable choice [188]. The coupling between the resonator and waveguide was modeled as two straight waveguides with an effective coupling length, L_{eff}.

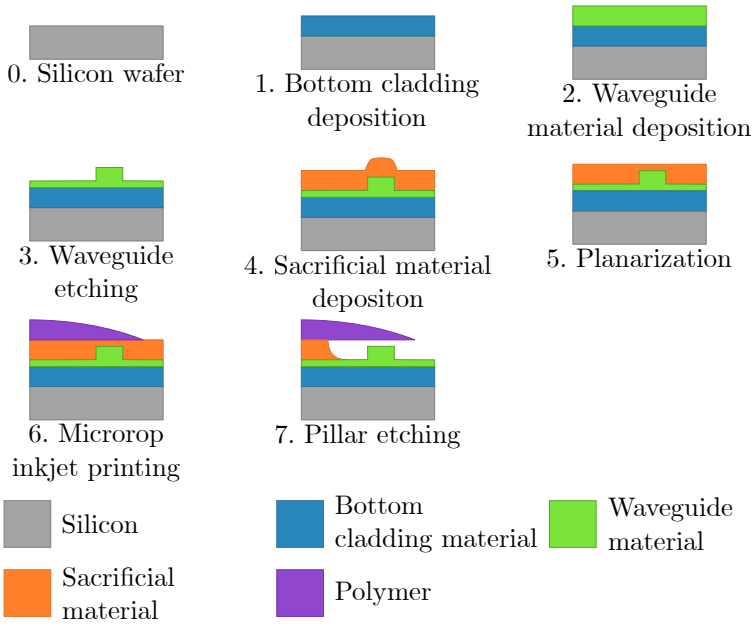

Figure 6.5 A general process flow illustrating the microfabrication of an integrated microdrop resonator over a photonic integrated circuit. This versatile process accommodates a wide range of materials and microfabrication techniques.

Given the structural differences between the resonator and waveguide, the coupling was inherently asymmetric.

First, we calculated the optical modes supported by both structures using COMSOL. For the waveguide, a mode analysis was conducted at a wavelength of 1550 nm, retaining only the TE0 mode, which has the highest effective refractive index. The resonator's resonance mode was calculated using an axis-symmetric domain, assuming a SU-8 material with a refractive index of 1.58. The resonator shape from the first article was reused, and the M-number was selected to ensure the TE0 mode was closest to a wavelength of 1550 nm. The complete complex fields from both COMSOL simulations were subsequently extracted for use in the coupled-mode theory calculations.

Due to its large radius relative to the wavelength (50 µm>1.55 µm), the resonator can be approximated as a straight waveguide in the coupling region. However, it is still necessary to define the effective coupling length between the two structures. This effective coupling length corresponds to the region where the separation between the two optical modes remains relatively constant during propagation [180]. Notably, a planar coupling would not be suitable for this approach. In this study, the flat zone was defined as the distance between the first two zeros of the second derivative of the distance between the optical modes.

From the optical mode overlap integral, we calculate the coupling propagation constant. Subsequently, we solve the coupling matrix system for the effective coupling distance to obtain the transmission spectrum.

The simulation geometry is illustrated in Fig. 6.6 with a top-down and a cross-section view. The parameters varied include the thickness t_w and width w_w of the waveguide, and the separation s in-between the waveguide and the resonator. Initially, we ensure that the waveguide supports an optical ($n_{\text{eff}} > n_b$). Then, for each thickness and width combination, we optimize the separation to achieve the highest transmission peak. The detailed results of these simulations are presented in Appendix B, where the relationship between waveguide dimensions, effective refractive index, and peak transmission are presented.

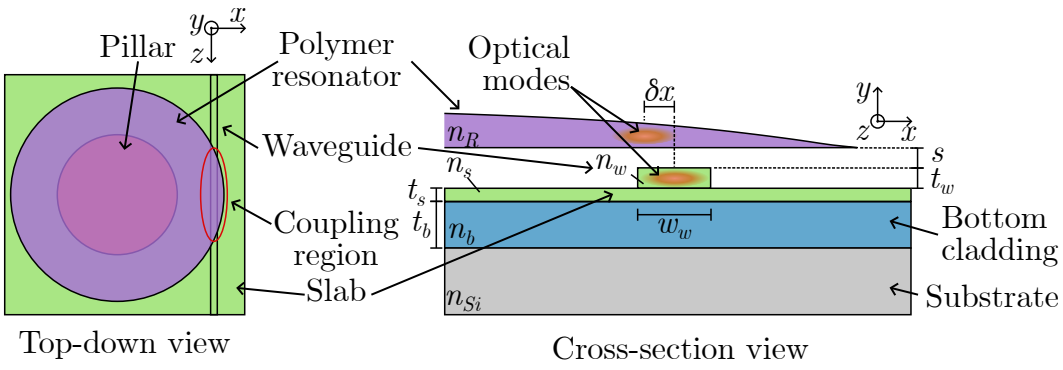

Figure 6.6 Top-down and cross-section views of the simulation geometry of a suspended polymer resonator coupled to a slab waveguide.

To ensure adequate optical performance, we optimized the bottom cladding thickness (t_b) for each selected configuration. This optimization was based on a minimum loss coefficient of 0.5 dB/mm, which corresponds to a loss of 10 dB for a 20-mm.

Lastly, to assess the system's sensitivity to misalignment, we simulated the transmission peak height for various lateral displacements in the x-direction (δx). The misalignment tolerance was defined as the maximum allowable displacement that resulted in a peak height reduction of no more than 3 dB.

6.4 Simulation Results and Discussion

Table 6.2 summarizes the optimized configurations for each proposed design, considering various waveguide core materials and types (ridge (A) and rib (B)). Rib waveguides with SU-8 cores utilize a silicon dioxide slab, while others have a core-matching slab. All rib designs feature a slab thickness of 100 nm. For each platform, the configuration with the

tallest transmission peak ($T_{\min}$) is reported with its waveguide width and thickness along with the optimal separation s between the waveguide and the resonator. And for these configurations, the minimal bottom cladding thickness t_b and the misalignment tolerance δx are calculated. Complete numerical results are given in appendix B.

To ensure manufacturability, we imposed constraints on the minimum waveguide thickness and separation between the resonator and waveguide, setting both to 100 nm.

Three designs exhibited peak heights below 3 dB, indicating poor coupling. This was attributed to a significant mismatch in the effective refractive indices between the waveguide and resonator. Consequently, we eliminated the silicon core waveguides (both ridge and rib) and the silicon nitride core rib waveguide from further consideration.

Table 6.2 Optimal performance of the proposed designs

Design	Core	Type	t_w (nm)	w_w (µm)	s (nm)	$T_{\min}$ (dB)	t_b (µm)	δx (µm)
1-A	SiN	Ridge	150	6	300	-48.8	1.84	5.3
1-B	SiN	Rib			No coupling			
2-A	SiO2	Ridge	800	6	100	-5.7	2.23	4.3
2-B	SiO2	Rib	800	6	100	-5.2	2.24	4.4
3-A	SU-8	Ridge	400	6	100	-15.8	2.31	6.0
3-B	SU-8	Rib	500	6	100	-12.7	2.04	7.6
4-A	Si	Ridge			No coupling			
4-B	Si	Rib			No coupling			

6.4.1 Minimum Thickness of the Bottom Cladding

To prevent optical mode leakage into the silicon substrate, the minimum bottom cladding thickness must exceed 2.31 µm for all designs. This constraint does not favor any particular design, as the required thicknesses are relatively similar. Moreover, this is only the minimum thickness. Any increase of this value will significantly lower the loss since the evanescence part of the optical mode decreases exponentially with the distance (see equation (3.7)). This is the case for both the waveguide and the resonator.

This additional constraint on the cladding thickness will limit some material candidates. However, this study was performed with a refractive index of 1.3 for the bottom cladding. Since porous silica can have a lower refractive index, a thinner layer is possible.

6.4.2 Misalignment Tolerance

The misalignment tolerance is important since inkjet printing is not as precise as photographically. On this matter, the design comprising the SU-8 rib waveguide with a silicon dioxide slab encompasses the largest tolerance with 7.6 µm. However, the worst misalignment tolerance of 4.3 µm could still be sufficient.

6.4.3 Alignment

To assess the Microdrop printer's potential for precise alignment with waveguides, trials were conducted to evaluate its microdroplet placement accuracy.

Calibration

A reference chip, featuring a known rectangular pattern, was fabricated by etching silicon nitride on a silicon substrate. After applying an hexamethyldisilazane (HMDS) layer, the goal was to accurately align microdroplets of SU-8 2000.5 photoresist with the center of the rectangle. The printer head and reference chip were maintained at 25 °C and 33 °C, respectively. Prior to each trial, printer parameters were optimized to ensure stable, satellite-free droplet formation.

To verify alignment accuracy, an image recognition algorithm was employed to determine the positions of both the microdroplet and the rectangular pattern. The Microdrop printer's integrated CS8630Ci camera (Toshiba Teli Corp) has a resolution of 0.47 pixels/micrometer. The camera and nozzle are positioned approximately 24 millimeters apart on the printer head. Camera and algorithm settings were optimized to detect the three edges of the rectangle. A Hough circle transform algorithm was used to identify the microdroplet.

The line connecting the camera and nozzle was aligned parallel to the x-axis of the motorized stage coordinate system. To calibrate the camera's position relative to the nozzle, a droplet was deposited. The reference chip was then moved from the nozzle to the camera position using previously calibrated coordinates. The droplet's position within the camera's field of view was determined, and the calibration was adjusted to ensure subsequent droplets were deposited at the camera's center. This process was repeated 10 times both before and after the calibration.

The error on the calibration is (1.4 ± 0.2) µm and (9.0 ± 0.4) µm for the x-axis and y-axis respectively.

To simulate variations in printing conditions that may occur during long prints or between

campaigns, the procedure was repeated after making minor adjustments to the printer parameters. Initially, the positional error increased significantly (10.24 µm). However, after a second calibration, the same error was observed, confirming the method's repeatability.

Despite calibration, the y-axis alignment error remains too large for optimal coupling (9 µm>7.6 µm). In contrast, the x-axis alignment is well within the smallest tolerance of the simulated platforms (2 µm<4.3 µm). Therefore, the waveguide should be oriented perpendicular to the x-axis.

Droplet Self-migration

To improve droplet alignment, surface modifications were explored. By creating surface energy gradients through physical etching (e.g. dents [261]) or chemical treatments [262–264], the microdroplets could be encouraged to self-migrate to their desired positions. This approach leverages the principle of wetting gradients, where droplets deposited in incorrect locations would be naturally drawn towards areas with more compatible surface properties.

To evaluate the chemical approach, silicon substrates (100 mm, p-doped Si <100>) were modified with HMDS (hydrophobic) or O_2-plasma (hydrophilic) treatments and then exposed to SU-8 2000.5 microdroplets (cyclopentanone solvent). While standard microfabrication cleaning procedures typically use HF and piranha solutions to create hydrophobic and hydrophilic surfaces, respectively, HF treatment is less stable over time, and piranha treatment is incompatible with standard photolithography.

A circular pattern with a different surface energy inside than outside was created. Microdroplets deposited within this circle would self-migrate towards the most compatible surface energy. The circle could be either hydrophobic inside and hydrophilic outside, or vice versa, depending on the ink's hydrophobicity to promote alignment.

The surface modification process begins with a silicon substrate that is cleaned in a piranha solution (3:1 of sulfuric acid and hydrogen peroxide) for 10 minutes followed by two dionized (DI) water baths for 2 minutes each to rinse the samples. The samples were then submerged for 3 minutes in a solution of 1 % HF and rinse with two baths of DI water for 5 minutes each. The first surface modification step is the HMDS treatment. The circle patterns are defined by standard photolithography either in the form of holes or disks. The next surface modification on the exposed surface of the substrate is performed with an O_2-plasma of 100 W for 3 minutes. The resist is striped with remover 1165 for 1 hour at 70 °C and cleaned with DI water.

To characterize the surface tension of the different chemical treatments, contact angle mea-

surements were performed on unpatterned samples that had undergone all process steps, including photolithography with either a flowed exposure or no exposure depending on the surface treatment. This approach ensured the measurements were representative of the surface energy in the final patterns.

Contact angle measurements were performed using DI water, ethylene glycol, and diiodomethane (CH_2I_2) as the liquid phase. Total surface tensions were obtained from the DSA100 equipment's software database from KRUSS. Three 3 µL droplets were deposited for each liquid-solid combination, and the average and standard deviation are presented in Tab. 6.3. The OWRK method was used to calculate total, dispersive, and polar surface tension components (Tab. 6.4). The polar component, which differs for HMDS (9.0 mN/m) and O_2-plasma (48.4 mN/m) treatments, determines hydrophobicity. SU-8 has a total surface tension of 31.8 mN/m, with dispersive and polar components of 22.3 mN/m and 9.5 mN/m, respectively. This photoresist is hydrophobic due to its low polar component, and the calculated contact angles for HMDS and O_2-plasma treatments are 67° and 103°, respectively. An SU-8 droplet at the boundary of these two treatments will migrate towards the HMDS-treated area.

To validate this hypothesis, a test chip was fabricated (Fig. 6.7 a). Silicon dioxide circles were patterned onto a silicon substrate and subsequently coated with a thin layer of evaporated silicon. The silicon dioxide circles remained visible through the thin silicon layer, which was then surface treated. The entire silicon layer was then treated with HMDS, followed by photolithography using the same mask aligned with the silicon dioxide circles. The exposed areas within the circles were then modified with an O_2-plasma treatment.

Following fabrication, SU-8 microdroplets were deposited onto the circular patterns with a control offset ranging from 30 to 150 µm. The circular patterns had a radius of 175 µm. To ensure clear visibility of the final droplet positions, the droplets were smaller than the circular patterns. Top-view camera images captured the droplets' final positions (Fig. 6.7 b). Self-migration was successful for offsets up to 45 µm. A microdroplet with a 150-µm offset

Table 6.3 Measured contact angles (θ_c) of HMDS and O_2-plasma surface treatments with three liquid phases

θ_c (°)	Liquid phase		
	Deionized water	Ethylene Glycol	CH_2I_2
HMDS treatment	69.9 ± 0.7	25.7 ± 1.4	32.5 ± 2.5
O_2-plasma treatment	13.5 ± 0.1	-	31.9 ± 0.6

Table 6.4 Total surface tensions and the dispersive and polar components for the three liquid phases taken from the software database and the two calculated surface treatments

	Phase	Surface tension (mN/m)		
		Total	Dispersive	Polar
Deionized water	Liquid	72.1	19.9	52.2
Ethylene glycol	Liquid	48	29	19
CH_2I_2	Liquid	50	47.4	2.6
HMDS treatment	Solid	45.2 ± 1.2	36.2 ± 1.4	9.0 ± 0.6
O_2-plasma treatment	Solid	67.9 ± 0.1	19.5 ± 0.1	48.4 ± 0.1

partially migrated towards the interior of the circle.

Given that the misalignment is less than 30 µm after calibration, self-migration should effectively align and confine microdroplets to within the resolution of UV lithography, which is approximately 1 µm in our facilities.

To fully validate this method, a comprehensive test involving a waveguide is required.

6.4.4 Platform Comparison

Only the silicon (ridge and rib) and silicon nitride (rib) platforms failed to achieve coupling. The minimum bottom cladding thickness is comparable for the other platforms. With the newly presented alignment technique, all remaining platforms have sufficient misalignment tolerance. The choice of the platform will primarily depend on microfabrication constraints and compatibility rather than optical performance.

The optimal waveguide width for all platforms is 6 µm, easily achievable using UV lithography. Silicon nitride waveguides (ridge) have the thinnest cross-section at 150 nm, while silicon dioxide waveguides (rib and ridge) are the thickest at 800 nm. These thicknesses can be achieved through physical or chemical vapor deposition methods. Additionally, SU-8 thicknesses of 400-500 nm are attainable using spin-coating.

The separation between the waveguide and resonator was 100 nm for all remaining platforms except for the silicon nitride waveguide (ridge), which had a separation of 300 nm. The silicon nitride waveguide was near overcoupling, and a smaller separation could result in an effective coupling length exceeding the physical coupling length, leading to mode beating between the waveguide and resonator. Both separations are achievable with all sacrificial materials. Moreover, the largest separation for the silicon nitride waveguide may help prevent structural collapse.

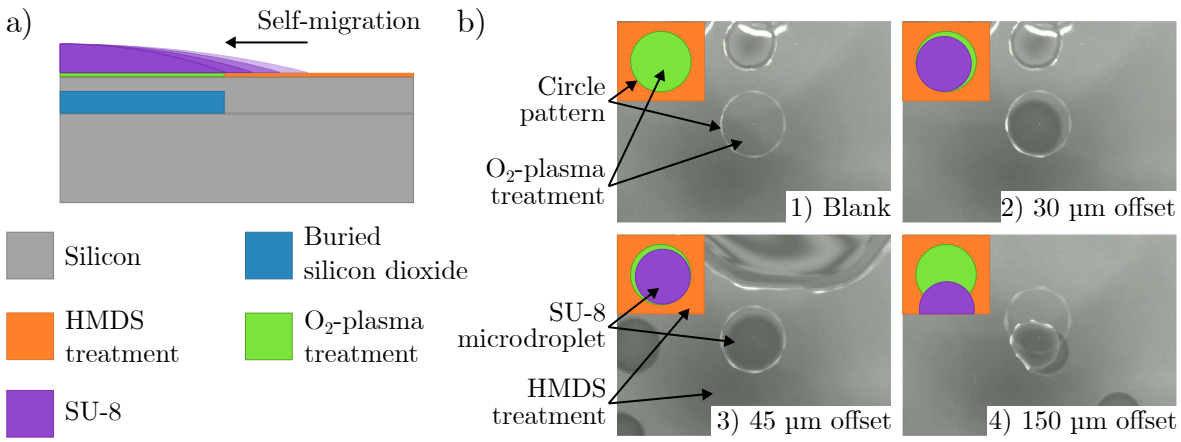

Figure 6.7 Alignment tests with surface modification. a) Schematic of the test chip and the self-migration of the SU-8 droplets. b) Optical micrographs of the test chip without microdroplet (1), and with microdroplets where an offset is used (2-4).

The choice of the sacrificial layer depends heavily on selectivity. Silicon, etched with an SF_6 plasma, is compatible with SiO_2 and SU-8 waveguides (rib and ridge). However, selectivity with the SiN waveguide may be insufficient. An undercut of at least 10 µm requires a selectivity of at least 1000:1, which can vary based on material quality. Literature reports a selectivity of 92:1 [265], but others [179] claimed that it is possible. A silicon dioxide sacrificial layer is incompatible with silicon dioxide waveguides. While SU-8 waveguides are resistant to vapor HF, porous silica will be etched. The selectivity between SiO_2 and SiN for vapor HF is 105:1, which is too low. LOR-5A, as a sacrificial layer, is compatible with all platforms but can limit the choice of resonator polymers. LOR-5A can dissolve certain polymers, and its wet etching process necessitates critical point drying to prevent structural collapse, further restricting polymer options.

For this last reason, the SiO_2 waveguide with a silicon sacrificial layer is selected as the best platform. It can couple to the resonators, and the sacrificial layer is compatible with the developed alignment procedure. The rib is preferred to protect the bottom cladding from the sacrificial layer etching.

6.5 Conclusion

The integration of the inkjet printed polymer resonator on a single photonic integrated circuit allows for a robust and versatile photonic platform. Specifically for gas sensing, the selectivity to different gases is possible by having a sensor matrix.

To accommodate the low effective refractive index of suspended polymer resonators, care must be taken in the selection of the photonic platform. Different materials and methods were compared for their optical performances and their manufacturability. More specifically, etching selectivity and alignment tolerance were discussed.

The greatest challenge lies in the bottom cladding. If its refractive index exceeds the low effective refractive index of the resonator, optical mode leakage and significant loss can occur. Various solutions have been proposed, with porous silica (obtained through oxidation or xerogel methods) being a promising option due to its tunable refractive index between air and silica and its compatibility with microfabrication. Furthermore, porous silica is the only solution that does not limit the range of compatible polymers.

The silicon dioxide rib waveguide with a silicon sacrificial layer is a promising platform for coupling with polymer resonators, offering a feasible fabrication process.

This work paves the way for a fully integrated system of suspended polymer resonators. While initially designed for gas sensing, this platform has potential applications in nonlinear photonics, integrated lasers, and biosensing.

CHAPTER 7 GENERAL DISCUSSION

7.1 Achieved Objectives

The first two sub-objectives have been achieved. The fabrication of the first suspended polymer microresonator was realized by combining inkjet printing with standard micromachining techniques. Additionally, this work represents the first instance of inkjet-printed microresonators being coupled to a tapered optical fiber. Previous research on inkjet-printed microresonators relied on photoluminescence setups and active media [25–28].

The versatility of the proposed manufacturing process was demonstrated by the successful fabrication of microresonators from three different polymers: SU-8, polystyrene (PS), and polyhexamethylene biguanide (PHMB). This versatility is evident in the use of diverse ink types, including photosensitive materials like SU-8 and water-soluble materials like PHMB.

A proof-of-concept demonstration of the device's utility for gas sensing applications was achieved by characterizing its sensitivity to three different analytes: carbon dioxide (CO_2), water (H_2O) vapor, and isopropanol (IPA). Additionally, the temperature dependence of the SU-8 microresonator was assessed, and a method to mitigate temperature effects was proposed.

The ability of inkjet printing to deposit multiple polymers on a single chip enables selective polymer-based gas sensing. Combined with temperature insensitivity, this approach can significantly minimize cross-sensitivity of the device.

The third sub-objective was not fully realized. While the proposed platform was not successfully integrated, a realistic platform for integrating inkjet-printed suspended polymer microresonators on a single optical chip has been proposed and analyzed in detail. The challenges associated with integrating suspended polymer microresonators, particularly the low effective refractive index of the resonant optical mode, have been investigated.

This work paves the way for a novel platform combining polymers and photonics. Beyond gas sensing, this technology holds potential for measuring various other quantities. Additionally, integrated polymer microresonators could serve as actuators or active device elements, expanding their applications. This project has advanced the state-of-the-art in additive fabrication techniques for microfabrication, polymer-based optical sensing, and integrated suspended optical resonators with low effective refractive indices.

7.2 Limitations

This technology presents certain limitations and challenges that warrant further investigation. Firstly, the fabrication process is complex due to the requirement of printing multiple inks with precise control. To date, the integration of the microresonators has not been demonstrated, necessitating the alignment of polymer droplets with micrometer-level precision. Following the integration, this device will require encapsulation to enable its use outside of a laboratory setting.

To achieve selectivity for numerous gases, a wide range of polymers must be printed. However, the fabrication process imposes constraints on the printable ink formulations. Additionally, the final polymer droplets must withstand the plasma etching process that defines the silicon pillars. Polymers such as polymethylmethacrylate (PMMA), poly(ethylene-vinyl acetate) (PEVA), polyallylamine hydrochloride (PAHCl), and polyethylene glycol (PEG) were unsuccessful due to various factors, including excessively high molecular weight or insufficient fusion temperature.

While selectivity and sensitivity have been discussed, significant challenges remain. Complex gas mixtures necessitate the ability to distinguish between different gases with high sensitivity. Furthermore, the fabrication process concludes with a plasma etching step, which may potentially impact the sensing performance of the polymers [266].

Polymers are excellent transducer materials for various quantities, but they also exhibit sensitivity crosstalk and environmental instability to factors such as temperature, pressure, and humidity. This added noise can limit performance. Noise contributions can be estimated from Eq. (3.66). For amplitude noise, the signal-to-noise ratio (SNR) is approximately 14 000, as observed in the spectra of the PS resonator (Fig. 5.5). From Eq. (3.67), with a wavelength of 1550 nm and a quality factor of 1×10^6, the amplitude noise is around 0.03 pm. The spectral resolution noise, as specified in the tunable laser source (TLS) data sheet, is 1 pm. Quantifying crosstalk noise is challenging. However, given the total measured noise range of 1 pm to 20 pm, crosstalk appears to be the dominant limiting factor. A high quality factor does not necessarily improve the limit of detections (LODs), as even with a quality factor of 1×10^4, the amplitude noise remains relatively low at 3 pm.

Since the sensing mechanism relies on absorption and solubility, no chemical reactions occur, ensuring complete sensor reversibility. However, polymers are susceptible to degradation over time, limiting their long-term stability. Exposure to UV light and high temperatures can induce chain scission, cross-linking, thermal oxidation, and volatilization. Additionally, exposure to gases may still lead to chemical reactions such as hydrolysis and oxidation. In

polymer blends, migration can further degrade performance. For instance, UV exposure is known to cause photochemical degradation in organic solar cells [267]. Additives such as antioxidants, UV stabilizers, and plasticizers can help improve the long-term stability of polymer sensors.

Inkjet printing requires the deposition of droplets individually, limiting its scalability and cost-effectiveness compared to techniques like UV lithography and roll-to-roll printing, which can achieve significantly higher throughput. Additionally, the required interrogation setup increases the overall cost and power consumption of the system. Nonetheless, inkjet printing remains relatively fast, with a typical rate of over 15 droplets per second, and multiple sensing devices can be connected to a single interrogation unit, reducing the impact of the interrogating setup.

CHAPTER 8 CONCLUSION

This thesis has successfully developed an optical platform of suspended microresonators for gas sensing. Polymer materials, fabricated using inkjet printing, have been demonstrated as effective transducer materials for gas detection. However, it's important to note that a single polymer is not inherently selective. To achieve selective gas sensing, the integration of multiple distinct polymers onto a single chip is necessary. While the vertical coupling of these microresonators with a photonic integrated circuit was a long term objective, this aspect remains a focus for future work. The foundational work presented in this thesis lays the groundwork for the realization of a fully integrated, highly sensitive, and selective multi-gas sensing platform.

The research was subdivided into three subobjectives. The first subobjective was to investigate the temperature dependence of the suggested devices and demonstrate the feasibility of this fabrication method for high-quality factor microresonators. The second subobjective was to fabricate microresonators from different polymers using the previous fabrication process, showcasing its versatility and measuring the performance of the fabricated devices for gas sensing. The final subobjective was to integrate these microresonators onto a single photonic integrated circuit (PIC).

Before presenting the work undertaken to achieve these objectives, an introduction to the importance of gas sensing, its diverse applications, and specific requirements (Ch. 1) is followed by a comprehensive literature review of the various components of this project (Ch. 2). Gas sensing methods, the critical role of selectivity in physical-chemical sensing, optical resonator principles, additive fabrication techniques, and photonic integration are explored to elucidate the reason behind the choice of the proposed technologies: physical-chemical sensing with multiple polymer transducers, suspended whispering gallery mode (WGM) resonators, inkjet printing, and vertical coupling. To facilitate a deeper understanding of the sensing phenomenon, a theoretical framework is provided on optical waveguides, whispering gallery mode resonators, detection mechanisms, and gas diffusion in a suspended polymer slab (Ch. 3).

The three subobjectives are each explored in depth within the three main themes of this thesis. The first article delves into the fabrication method of an SU-8 suspended microresonator and investigates its temperature dependence (Ch. 4). The second article expands upon the fabrication method, applying it to two additional polymers. The gas sensing performance of all three polymer microresonators is subsequently studied (Ch. 5). The third theme focuses

on exploring potential solutions for integrating these sensing devices onto a PIC (Ch. 6).

8.1 Summary of Works

The fabrication of suspended polymer resonators, combining inkjet printing and traditional microfabrication techniques, was demonstrated for three distinct polymers. These WGM resonators, supported by silicon pillars, were coupled to tapered optical fibers. Prior to exploring their environmental sensing capabilities, the resonators were characterized by their shapes and optical transmission spectra. The spectra revealed a unique profile attributed to the coffee ring effect, as well as resonance peaks exhibiting high quality factors.

The temperature sensitivity of SU-8 microresonators was studied, demonstrating that, for a specific undercut-to-radius ratio, the polymer resonators exhibited negligible temperature sensitivity. This finding holds significant potential for enhancing the precision of gas sensing applications. The platform's suitability for gas sensing was validated by evaluating the performance of suspended microresonators fabricated from three distinct polymers. This proof-of-concept study revealed high sensitivity and low detection limits for three different gases. Finally, various photonic platforms were explored to integrate these sensing devices with a PIC. Challenges such as mode leakage and resonator misalignment were investigated, and potential solutions were proposed.

This work advances several research areas, including the combination of microfabrication and inkjet printing as an additive fabrication technique. Additionally, it pushes the boundaries of integrated photonics, polymer science, and gas sensing by integrating diverse technologies. Potential applications include industries where traditional electric gas sensors pose challenges, such as mining, petroleum, smart cities, and industrial plants. The advantages of this approach include the elimination of fire and explosion hazards and the potential for integrating these gas sensors into optical networks connected by long optical fibers. Ongoing efforts are focused on methane detection in dairy barns, aiming to quantify greenhouse gas emissions from ruminants, which contribute significantly to carbon dioxide equivalent emissions. A preliminary polymer-functionalized Fabry-Perot interferometer (FPI) has been utilized, but the transition to WGM resonators is considered due to their higher quality factors and the absence of constraints imposed by resonator walls, as found in FPI devices.

8.2 Future Research

This project presents numerous avenues for future research. As the integration phase remains incomplete, it represents the next logical step toward achieving the long term objective. As

outlined in Sec. 6, the proposed photonic platform consists of silicon dioxide rib waveguides on a porous silicon dioxide bottom cladding. This material combination enables the integration of very low refractive index polymers. Furthermore, the rib configuration ensures the protection of the porous bottom cladding. Given the demonstrated compatibility of silicon, used as the sacrificial layer for pillar formation, with certain polymers, it emerges as a promising initial candidate. This layer can be planarized using chemical-mechanical polishing (CMP). To ensure accurate alignment between the inkjet-printed resonator and the waveguide, surface modifications to facilitate droplet self-migration can be readily incorporated into the fabrication process, as this technique has been successfully applied to silicon substrates.

Additional investigations into the fabrication process are necessary. For instance, the selectivity of polymers with respect to the sacrificial layer etching process must be assessed. The proposed fabrication process employs reaction ion etching (RIE) etching with an SF_6 plasma. Similar to traditional microfabrication materials [265], a database of etch rates is crucial to ensure selectivity and design the fabrication process effectively.

After developing a robust fabrication process, the performance of the microresonators as gas sensors can be explored across a range of geometric parameters, including radius, thickness, and undercut. These parameters form a design space that can be systematically investigated. As demonstrated for temperature sensitivity with SU-8, the sensitivity may be a function of the undercut-to-radius ratio of the resonator, as this ratio influences the relative contributions of expansion and refractive index change.

The inkjet printing employed in this thesis is relatively straightforward, utilizing inks composed solely of a polymer and a solvent. By modifying the ink formulation through the incorporation of different polymers, surfactants, nanoparticles, graphene, or active photochemical for fluorescence and lasing [152], the gas-sensing capabilities can be further expanded. Additionally, adjusting printing parameters can influence droplet shape, such as altering substrate temperature to impact the coffee ring effect [146] or fabricating resonators from multiple droplets. These modifications can subsequently alter the dispersion and optical mode shapes of the resonators. This opens up the possibility of exploring multi-variable detection to enhance selectivity by combining the responses of multiple resonance modes [103, 121]. Following deposition, the droplets can be functionalized with biomolecules [28]. Another potential modification involves printing porous droplets [268, 269], which can increase surface interaction, enhance gas diffusion within the resonator, and amplify gas-light interaction. However, it's important to consider that porous structures may also reduce resonator expansion.

A deeper understanding of the interactions between gases and polymers is essential. The

complex interplay of adsorption, absorption, diffusion, swelling, and refractive index changes requires more refined modeling. While research has been conducted on polymer diffusion and swelling [82, 230, 270], particularly in glassy polymers with free volume [271], further investigation is needed. Moreover, the applicability of the research on polymeric membrane permeability at high pressure differences [272] needs to be investigated for absorption at equilibrium pressures. Another crucial aspect of gas sensing performance is selectivity, which relies on the affinity between the gas and the polymer. Experimental work is required to establish a comprehensive database of these affinities and assess the validity of models like COSMO-RS [273]. This data, combined with etching selectivity information, can aid in the selection of suitable polymers.

To directly study affinity, methods that can separate the contributions of expansion, refractive index change, and absorbed gas fractions in the polymer are necessary. Techniques such as interferometric refractometry [229] and ellipsometry [274, 275] can simultaneously measure the thickness and refractive index of a polymer thin film and their changes. When combined with quartz crystal microbalance (QCM), which measures mass changes [9], these techniques can provide valuable insights into polymer-gas interactions. This experimental data can be integrated with existing literature on other polymer-based gas sensors, such as surface acoustic wave (SAW), QCM, capacitive micromachined ultrasonic transducer (CMUT), and electronic gas sensors.

At this stage, the technology readiness level (TRL) of this technology is 3[1]. To advance to higher TRL levels, the device must be fully integrated, encapsulated (TRL 4[2]), and tested outside a laboratory environment (TRL 5[3]). This requires robust fiber-to-chip coupling and a protective enclosure to safeguard the sensor from harsh environmental conditions.

With a robust fabrication process, a deep understanding of the sensing mechanism and a well-encapsulated device, this technology would be ready to target various applications. While the proof-of-concept focused on readily available polymers and common gases and volatile organic compounds (VOCs), prioritizing sensor application was not the primary concern. However, the selection of polymers should be informed by the specific analytes present in the target gas mixture and an understanding of polymer-gas affinities. This enables applications such as environmental monitoring, where precise detection of pollutants and greenhouse gases is crucial, and healthcare, where the detection of biomarkers in breath can aid in disease diagnosis.

[1] "Analytical and experimental critical function and/or proof of concept" [276]
[2] "Component and/or validation in a laboratory environment" [276]
[3] "Component and/or validation in a simulated environment " [276]

To ensure reliability, the sensors' performance must be rigorously evaluated through extensive testing, including assessing reversibility, repeatability, and long-term stability with repeated measurements over weeks, months, and years. To facilitate widespread adoption, the technology's scalability must be considered, including investigations into cost and power consumption.

To measure the wavelength shift, a tunable laser source (TLS) and a photodetector (PD) were used to scan and acquire the transmission spectrum. While this setup offers high precision, it is bulky and costly. Although it can interrogate multiple sensors and be deployed in remote and safe locations, alternative interrogation methods should be explored. A simpler approach involves fixing a narrow laser peak slightly detuned from the resonance peak, placing it on the peak's slope [277] and record the amplitude over time. This technique requires only a fixed laser and a photodiode, but it is susceptible to amplitude noise and presents a trade-off between the sensitivity and the sensing range. To record the spectrum, a broadband source and an optical spectrum analyzer can be used [76]. However, this method is slow and costly. A more cost-effective approach involves scanning the spectrum with a tunable filter, such as a thermally tuned ring resonator [278]. One drawback of using a broadband source is the significant power coupled to the resonator. An alternative approach utilizes a mode-locked laser to track the resonance peak [279]. This method offers high speed and precise information on the position of a single resonance peak. At the resonance peak, an abrupt phase shift occurs. By interfering two laser beams coupled to the resonator, one tuned to the resonance wavelength and the other detuned, the phase difference can be recorded [280].

The focus of this work was to develop a sensing platform for the detection of gases and VOCs. However, this technology is not limited to these applications. Polymer-based optical sensors have been used to measure temperature [226], humidity [226], pressure [75], pH [73] and biomolecules [28]. Polymer resonators can also be used as passive and active elements of a photonic integrated circuit (PIC) by integrating them with other photonic elements and electronics.This approach offers significant versatility.

8.3 Conclusion

This thesis presented a novel platform of integrated high-quality factor resonators fabricated from various polymers, combining inkjet printing and microfabrication techniques. These devices were shown to exhibit temperature insensitivity and the ability to distinguish and quantify multiple gases. Beyond temperature and gas sensing, integrated polymer resonators have the potential to measure numerous other quantities, leveraging the diversity of polymers and their potential for functionalization. While full integration was not experimentally

demonstrated, a comprehensive analysis of various platforms and alignment solutions was provided.

This work explores the intersection of high-quality optical resonators, inkjet printing, polymer-based gas sensing, and on-chip optical integration. This integration of technologies holds the potential to create an optical nose capable of addressing various gas sensing challenges.

REFERENCES

[1] C. Bushdid, M. O. Magnasco, L. B. Vosshall, and A. Keller, "Humans can discriminate more than 1 trillion olfactory stimuli," *Science*, vol. 343, no. 6177, pp. 1370–1372, Mar. 2014. doi: 10.1126/science.1249168 .

[2] J. K. Olofsson, "Time to smell: a cascade model of human olfactory perception based on response-time (RT) measurement," *Front. Psychol.*, vol. 5, 2014. doi: 10.3389/fpsyg.2014.00033 .

[3] Y. Gilad, "Population differences in the human functional olfactory repertoire," *Mol. Biol. Evol.*, vol. 20, no. 3, pp. 307–314, Mar. 2003. doi: 10.1093/molbev/msg013 .

[4] P. M. Wise, "Quantification of odor quality," *Chem. Senses*, vol. 25, no. 4, pp. 429–443, Aug. 2000. doi: 10.1093/chemse/25.4.429 .

[5] N. M. Shaalan, F. Ahmed, O. Saber, and S. Kumar, "Gases in food production and monitoring: Recent advances in target chemiresistive gas sensors," *Chemosensors*, vol. 10, no. 8, p. 338, Aug. 2022. doi: 10.3390/chemosensors10080338 .

[6] T.-Y. Yen and D.-J. Yao, "Detection of the freshness of kiwifruit with a TD-GC-MS and a gas-sensing array based on the surface-acoustic-wave technique," *IEEE Transactions on NanoBioscience*, vol. 21, no. 3, pp. 363–369, Jul. 2022. doi: 10.1109/tnb.2021.3094505 .

[7] S. Matindoust, M. Baghaei-Nejad, M. H. S. Abadi, Z. Zou, and L.-R. Zheng, "Food quality and safety monitoring using gas sensor array in intelligent packaging," *Sensor Rev.*, vol. 36, no. 2, pp. 169–183, Mar. 2016. doi: 10.1108/sr-07-2015-0115 .

[8] Z. Li and K. S. Suslick, "Portable optoelectronic nose for monitoring meat freshness," *ACS Sensors*, vol. 1, no. 11, pp. 1330–1335, Nov. 2016. doi: 10.1021/acssensors.6b00492 .

[9] K. Liu and C. Zhang, "Volatile organic compounds gas sensor based on quartz crystal microbalance for fruit freshness detection: A review," *Food Chem.*, vol. 334, p. 127615, Jan. 2021. doi: 10.1016/j.foodchem.2020.127615 .

[10] A. R. Ferdous, S. N. A. Shah, S. S. Shah, and M. A. Aziz, "Advancements in nanotechnology applications: Transforming catalysts, sensors, and coatings in petrochemical industries," *Fuel*, vol. 371, p. 132020, Sep. 2024. doi: 10.1016/j.fuel.2024.132020 .

[11] K. Calvin *et al.*, *IPCC, 2023: Climate Change 2023: Synthesis Report. Contribution of Working Groups I, II and III to the Sixth Assessment Report of the Intergovernmental Panel on Climate Change [Core Writing Team, H. Lee and J. Romero (eds.)]. IPCC, Geneva, Switzerland.*, P. Arias *et al.*, Eds., Jul. 2023. doi: 10.59327/ipcc/ar6-9789291691647 .

[12] Y. de Haas, M. Pszczola, H. Soyeurt, E. Wall, and J. Lassen, "Invited review: Phenotypes to genetically reduce greenhouse gas emissions in dairying," *J. Dairy Sci.*, vol. 100, no. 2, pp. 855–870, Feb. 2017. doi: 10.3168/jds.2016-11246 .

[13] *Niveaux de référence dans l'air intérieur liés à l'exposition chronique aux composés organiques volatils : document de synthèse.* Ottawa (Ontario): Santé Canada, 2017.

[14] Z. Zhang, T. Xue, and X. Jin, "Effects of meteorological conditions and air pollution on COVID-19 transmission: Evidence from 219 Chinese cities," *Sci. Total Environ.*, vol. 741, p. 140244, Nov. 2020. doi: 10.1016/j.scitotenv.2020.140244 .

[15] S. Vucinic, B. Antonijevic, A. M. Tsatsakis, L. Vassilopoulou, A. O. Docea, A. E. Nosyrev, B. N. Izotov, H. Thiermann, N. Drakoulis, and D. Brkic, "Environmental exposure to organophosphorus nerve agents," *Environ. Toxicol. Phar.*, vol. 56, pp. 163–171, Dec. 2017. doi: 10.1016/j.etap.2017.09.004 .

[16] Z. Song *et al.*, "Wireless self-powered high-performance integrated nanostructured-gas-sensor network for future smart homes," *ACS Nano*, vol. 15, no. 4, pp. 7659–7667, Apr. 2021. doi: 10.1021/acsnano.1c01256 .

[17] B. Buszewski, J. Rudnicka, T. Ligor, M. Walczak, T. Jezierski, and A. Amann, "Analytical and unconventional methods of cancer detection using odor," *TrAC Trends in Analytical Chemistry*, vol. 38, pp. 1–12, Sep. 2012. doi: 10.1016/j.trac.2012.03.019 .

[18] Y. Saalberg and M. Wolff, "VOC breath biomarkers in lung cancer," *Clin. Chim. Acta*, vol. 459, pp. 5–9, Aug. 2016. doi: 10.1016/j.cca.2016.05.013 .

[19] "Gas sensor market," Jul. 2024. [Online]. Available: https://www.gminsights.com/industry-analysis/gas-sensors-market-size

[20] R. St-Gelais, G. Mackey, J. Saunders, J. Zhou, A. Leblanc-Hotte, A. Poulin, J. A. Barnes, H.-P. Loock, R. S. Brown, and Y.-A. Peter, "Gas sensing using polymer-functionalized deformable Fabry-Perot interferometers," *Sens. Actuators, B*, vol. 182, pp. 45–52, Jun. 2013. doi: 10.1016/j.snb.2013.02.016 .

[21] P. Jubinville, R. Guertin, L. Erbilgin, W. Skene, and Y.-A. Peter, "Selective in-plane Fabry-Pérot gas sensor functionalized with polymer," in *Proc. Int. Conf. Optical MEMS and Nanophotonics (OMN)*, Aug. 2017, pp. 1–2. doi: 10.1109/OMN.2017.8051493 .

[22] R. Guertin, M.-A. Bianki, C. Lemieux-Leduc, and Y.-A. Peter, "Multi-gas detection using Fabry-Perot interferometers on silicon chip," *Sens. Actuators, B*, p. 129655, Feb. 2021. doi: 10.1016/j.snb.2021.129655 .

[23] M. Eryürek, Z. Tasdemir, Y. Karadag, S. Anand, N. Kilinc, B. Alaca, and A. Kiraz, "Integrated humidity sensor based on SU-8 polymer microdisk microresonator," *Sens. Actuators, B*, vol. 242, pp. 1115–1120, Apr. 2017. doi: 10.1016/j.snb.2016.09.136 .

[24] C. Lemieux-Leduc, R. Guertin, M.-A. Bianki, and Y.-A. Peter, "All-polymer whispering gallery mode resonators for gas sensing," *Opt. Express*, vol. 29, no. 6, p. 8685, Mar. 2021. doi: 10.1364/oe.417703 .

[25] K. T. A. Nasir, C. Chen, Y. Mikami, T. Takagishi, H. Yoshioka, M. Matsuyama, N. Nishimura, N. J. Vasa, and Y. Oki, "Lasing characteristics of a pyrromethene597-doped microdisk laser fabricated by the ink-jet printing method," *Jpn. J. Appl. Phys.*, vol. 58, no. SJ, p. SJJC05, Jul. 2019. doi: 10.7567/1347-4065/ab1e3c .

[26] H. Yoshioka, T. Ota, C. Chen, S. Ryu, K. Yasui, and Y. Oki, "Extreme ultra-low lasing threshold of full-polymeric fundamental microdisk printed with room-temperature atmospheric ink-jet technique," *Sci. Rep.*, vol. 5, no. 1, May 2015. doi: 10.1038/srep10623 .

[27] C. Chen, S. Ryu, H. Yoshioka, K. Yasui, and Y. Oki, "Low-threshold lasing from organic and polymeric microdisk printed by room temperature atmosphere ink-jet technique," in *Organic Photonic Materials and Devices XVII*, C. E. Tabor, F. Kajzar, T. Kaino, and Y. Koike, Eds. SPIE, Mar. 2015. doi: 10.1117/12.2078965 .

[28] A. Nasir, R. Yatabe, Y. Mikami, H. Yoshioka, N. Vasa, and Y. Oki, "Ink-jet printed, blended polymer-based microdisk resonators for controlling non-specific adsorption of biomolecules," *Opt. Lett.*, vol. 46, no. 2, pp. 262–265, Jan. 2021. doi: 10.1364/OL.412993 .

[29] P. F. Dunn, *Fundamentals of Sensors for Engineering and Science*. CRC Press, Apr. 2011. doi: 10.1201/9781439895252 .

[30] G. Wiegleb, *Gas Measurement Technology in Theory and Practice: Measuring Instruments, Sensors, Applications*. Springer Fachmedien Wiesbaden, 2023. doi: 10.1007/978-3-658-37232-3 .

[31] A. Gupta, M. Kumar, R. K. Singh, and S. Bhattacharya, *Gas Sensors: Manufacturing, Materials, and Technologies*. CRC Press, Sep. 2022. doi: 10.1201/9781003278047 .

[32] B. P. Regmi and M. Agah, "Micro gas chromatography: An overview of critical components and their integration," *Anal. Chem.*, vol. 90, no. 22, pp. 13 133–13 150, Oct. 2018. doi: 10.1021/acs.analchem.8b01461 .

[33] K. Scholten, W. R. Collin, X. Fan, and E. T. Zellers, "Nanoparticle-coated microoptofluidic ring resonator as a detector for microscale gas chromatographic vapor analysis," *Nanoscale*, vol. 7, no. 20, pp. 9282–9289, 2015. doi: 10.1039/c5nr01780g .

[34] F. Haghighi, Z. Talebpour, and A. Sanati-Nezhad, "Through the years with on-a-chip gas chromatography: A review," *Lab Chip*, vol. 15, no. 12, pp. 2559–2575, 2015. doi: 10.1039/c5lc00283d .

[35] K. Jasek, M. Pasternak, and M. Grabka, "Paramagnetic sensors for the determination of oxygen concentration in gas mixtures," *ACS Sens.*, vol. 7, no. 11, pp. 3228–3242, Oct. 2022. doi: 10.1021/acssensors.2c00938 .

[36] D. Berndt, J. Muggli, F. Wittwer, C. Langer, S. Heinrich, T. Knittel, and R. Schreiner, "MEMS-based thermal conductivity sensor for hydrogen gas detection in automotive applications," *Sens. Actuators, A*, vol. 305, p. 111670, Apr. 2020. doi: 10.1016/j.sna.2019.111670 .

[37] T. Liu, J. Cui, Y. Zheng, S. Bai, C. Hao, and C. Xue, "A self-powered inert-gas sensor based on gas ionization driven by a triboelectric nanogenerator," *Nano Energy*, vol. 106, p. 108083, Feb. 2023. doi: 10.1016/j.nanoen.2022.108083 .

[38] M. Zou, Z. Yang, L. Sun, and X. Ming, "Acetylene sensing system based on wavelength modulation spectroscopy using a triple-row circular multi-pass cell," *Opt. Express*, vol. 28, no. 8, p. 11573, Apr. 2020. doi: 10.1364/oe.388343 .

[39] "NSRDS-NBS: National standard reference data series, national bureau of standards," U.S. Government Printing Office, Tech. Rep., Jun. 1972.

[40] H. Zhou, D. Li, X. Hui, and X. Mu, "Infrared metamaterial for surface-enhanced infrared absorption spectroscopy: pushing the frontier of ultrasensitive on-chip

sensing," *Int. J. Optomechatroni.*, vol. 15, no. 1, pp. 97–119, Jan. 2021. doi: 10.1080/15599612.2021.1953199 .

[41] S. Khan, D. Newport, and S. Le Calvé, "Gas detection using portable deep-UV absorption spectrophotometry: A review," *Sensors-basel.*, vol. 19, no. 23, p. 5210, Nov. 2019. doi: 10.3390/s19235210 .

[42] M. Moayedi, H. R. Ansari, and Z. Kordrostami, "Highly sensitive isopropanol gas sensor based on SnO_2 nano-flowers on gold, silver, and aluminum interdigitated electrodes," *ECS J. Solid State Sci. Technol.*, vol. 12, no. 5, p. 057011, May 2023. doi: 10.1149/2162-8777/acd3ad .

[43] C. Zhang, Y. Huan, Y. Li, Y. Luo, and M. Debliquy, "Low concentration isopropanol gas sensing properties of Ag nanoparticles decorated In_2O_3 hollow spheres," *J. Adv. Ceram.*, vol. 11, no. 3, pp. 379–391, Mar. 2022. doi: 10.1007/s40145-021-0530-x .

[44] J. Sweelssen, H. Blokland, T. Rajamäki, R. Sarjonen, and A. Boersma, "A versatile capacitive sensing platform for the assessment of the composition in gas mixtures," *Micromachines*, vol. 11, no. 2, p. 116, Jan. 2020. doi: 10.3390/mi11020116 .

[45] B. Nketia-Yawson and Y.-Y. Noh, "Organic thin film transistor with conjugated polymers for highly sensitive gas sensors," *Macromol. Res.*, vol. 25, no. 6, pp. 489–495, Jun. 2017. doi: 10.1007/s13233-017-5108-7 .

[46] M. N. Padvi, A. V. Moholkar, S. R. Prasad, and N. R. Prasad, "A critical review on design and development of gas sensing materials," *Engineered Science*, vol. 15, no. 0, pp. 20–37, Mar. 2021. doi: 10.30919/es8d431 .

[47] C. O. Park, J. W. Fergus, N. Miura, J. Park, and A. Choi, "Solid-state electrochemical gas sensors," *Ionics*, vol. 15, no. 3, pp. 261–284, Jan. 2009. doi: 10.1007/s11581-008-0300-6 .

[48] Y. C. Wong, B. C. Ang, A. S. M. A. Haseeb, A. A. Baharuddin, and Y. H. Wong, "Review—conducting polymers as chemiresistive gas sensing materials: A review," *J. Electrochem. Soc.*, vol. 167, no. 3, p. 037503, Sep. 2019. doi: 10.1149/2.0032003JES .

[49] S. Park, C. Park, and H. Yoon, "Chemo-electrical gas sensors based on conducting polymer hybrids," *Polymers*, vol. 9, no. 12, p. 155, Apr. 2017. doi: 10.3390/polym9050155 .

[50] K. Singh, "An investigation of Na_2CO_3-ABO_3 (A=Li/K/Ba and B=Nb/Ti) heterogeneous solid electrolyte systems for electrochemical CO_2 gas sensor application,"

Solid State Ionics, vol. 122, no. 1–4, pp. 191–196, Jul. 1999. doi: 10.1016/s0167-2738(99)00033-8 .

[51] P. Shinde and C. S. Rout, "Magnetic gas sensing: Working principles and recent developments," *Nanoscale Adv.*, vol. 3, no. 6, pp. 1551–1568, 2021. doi: 10.1039/d0na00826e .

[52] S. Park, I. Yoon, S. Lee, H. Kim, J.-W. Seo, Y. Chung, A. Unger, M. Kupnik, and H. J. Lee, "CMUT-based resonant gas sensor array for VOC detection with low operating voltage," *Sens. Actuators, B*, vol. 273, pp. 1556–1563, Nov. 2018. doi: 10.1016/j.snb.2018.07.043 .

[53] D. Then, A. Vidic, and C. Ziegler, "A highly sensitive self-oscillating cantilever array for the quantitative and qualitative analysis of organic vapor mixtures," *Sens. Actuators, B*, vol. 117, no. 1, pp. 1–9, Sep. 2006. doi: 10.1016/j.snb.2005.07.069 .

[54] M. Benetti, D. Cannatà, E. Verona, A. P. Papavlu, V. C. Dinca, T. Lippert, M. Dinescu, and F. D. Pietrantonio, "Highly selective surface acoustic wave e-nose implemented by laser direct writing," *Sens. Actuators, B*, vol. 283, pp. 154–162, Mar. 2019. doi: 10.1016/j.snb.2018.12.005 .

[55] A. Marcu, I. Nicolae, and C. Viespe, "Active surface geometrical control of noise in nanowire-SAW sensors," *Sens. Actuators, B*, vol. 231, pp. 469–473, Aug. 2016. doi: 10.1016/j.snb.2016.03.015 .

[56] S. H. Cho, J. M. Suh, T. H. Eom, T. Kim, and H. W. Jang, "Colorimetric sensors for toxic and hazardous gas detection: A review," *Electron. Mater. Lett.*, vol. 17, no. 1, pp. 1–17, Nov. 2020. doi: 10.1007/s13391-020-00254-9 .

[57] C. Deleau, H. C. Seat, F. Surre, F. Carcenac, P.-F. Calmon, and O. Bernal, "Gas sensor based on silicon nitride integrated long period grating," in *2022 IEEE Sensors*. IEEE, Oct. 2022, pp. 1–4. doi: 10.1109/SENSORS52175.2022.9967080 ., iSSN: 2168-9229.

[58] S. H. Badri, "Transmission resonances in silicon subwavelength grating slot waveguide with functional host material for sensing applications," *Opt. Laser Technol.*, vol. 136, p. 106776, Apr. 2021. doi: 10.1016/j.optlastec.2020.106776 .

[59] L. Burratti, F. D. Matteis, M. Casalboni, R. Francini, R. Pizzoferrato, and P. Prosposito, "Polystyrene photonic crystals as optical sensors for volatile organic compounds," *Mater. Chem. Phys.*, vol. 212, pp. 274–281, Jun. 2018. doi: 10.1016/j.matchemphys.2018.03.039 .

[60] R. Tong, Y. Wang, K.-j. Zhao, X. Li, and Y. Zhao, "Surface plasmon resonance optical fiber sensor for relative humidity detection without temperature crosstalk," *Opt. Laser Technol.*, vol. 150, p. 107951, Jun. 2022. doi: 10.1016/j.optlastec.2022.107951 .

[61] M. Irfan, Y. Khan, A. U. Rehman, N. Ullah, S. N. Khonina, N. L. Kazanskiy, and M. A. Butt, "Plasmonic perfect absorber utilizing polyhexamethylene biguanide polymer for carbon dioxide gas sensing application," *Materials*, vol. 16, no. 7, p. 2629, Jan. 2023. doi: 10.3390/ma16072629 .

[62] N. Zhu, B. Shi, Y. Guo, B. Han, and Y.-n. Zhang, "Polydimethylsiloxane self-assembled whispering gallery mode microbottle resonator for ethanol sensing," *Opt. Mater.*, vol. 107, p. 110024, Sep. 2020. doi: 10.1016/j.optmat.2020.110024 .

[63] N. L. Kazanskiy, M. A. Butt, and S. N. Khonina, "Carbon dioxide gas sensor based on polyhexamethylene biguanide polymer deposited on silicon nano-cylinders metasurface," *Sensors-basel.*, vol. 21, no. 2, p. 378, Jan. 2021. doi: 10.3390/s21020378 .

[64] G. Lu and J. T. Hupp, "Metal-organic frameworks as sensors: A ZIF-8 based Fabry-Pérot device as a selective sensor for chemical vapors and gases," *JACS*, vol. 132, no. 23, pp. 7832–7833, May 2010. doi: 10.1021/ja101415b .

[65] Y. Li, W. Shen, C. Zhao, B. Xu, D. Wang, and M. Yang, "Optical hydrogen sensor based on PDMS-formed double-C type cavities with embedded pt-loaded WO_3/SiO_2," *Sens. Actuators, B*, vol. 276, pp. 23–30, Dec. 2018. doi: 10.1016/j.snb.2018.08.019 .

[66] M. F. S. Ferreira *et al.*, "Roadmap on optical sensors," *J. Opt.*, vol. 19, no. 8, p. 083001, Jul. 2017. doi: 10.1088/2040-8986/aa7419 .

[67] P. Lu, N. Lalam, M. Badar, B. Liu, B. T. Chorpening, M. P. Buric, and P. R. Ohodnicki, "Distributed optical fiber sensing: Review and perspective," *Appl. Phys. Rev.*, vol. 6, no. 4, Oct. 2019. doi: 10.1063/1.5113955 .

[68] A. Tripathy, S. Pramanik, J. Cho, J. Santhosh, and N. A. Osman, "Role of morphological structure, doping, and coating of different materials in the sensing characteristics of humidity sensors," *Sensors-basel.*, vol. 14, no. 9, pp. 16 343–16 422, Sep. 2014. doi: 10.3390/s140916343 .

[69] M. Wusiman and F. Taghipour, "Methods and mechanisms of gas sensor selectivity," *Crit. Rev. Solid State*, vol. 47, no. 3, pp. 416–435, Sep. 2021. doi: 10.1080/10408436.2021.1941752 .

[70] L. Ge, X. Ye, Z. Yu, B. Chen, C. Liu, H. Guo, S. Zhang, F. Sassa, and K. Hayashi, "A fully inkjet-printed disposable gas sensor matrix with molecularly imprinted gas-selective materials," *npj Flexible Electronics*, vol. 6, no. 1, pp. 1–10, Jun. 2022. doi: 10.1038/s41528-022-00168-6 .

[71] L. Hu, Q. Zhang, X. Li, and M. J. Serpe, "Stimuli-responsive polymers for sensing and actuation," *Mater. Horiz.*, vol. 6, no. 9, pp. 1774–1793, 2019. doi: 10.1039/c9mh00490d .

[72] M. M. Kiaee, T. Maeder, and J. Brugger, "Film morphology effect on voc sensor performance fabricated by drop-on-demand inkjet-printing," in *Proc. Actuators and Microsystems Eurosensors XXXIII (TRANSDUCERS EUROSENSORS XXXIII) 2019 20th Int. Conf. Solid-State Sensors*, Jun. 2019, pp. 1361–1364. doi: 10.1109/TRANSDUCERS.2019.8808652 .

[73] N. Saha, G. Brunetti, M. N. Armenise, and C. Ciminelli, "A compact, highly sensitive pH sensor based on polymer waveguide Bragg grating," *IEEE Photonics J.*, vol. 15, no. 2, pp. 1–7, Apr. 2023. doi: 10.1109/JPHOT.2023.3242820 .

[74] C.-L. Lee, C.-T. Ma, K.-C. Yeh, and Y.-M. Chen, "A dual-cavity fiber Fabry–Pérot interferometer for simultaneous measurement of thermo-optic and thermal expansion coefficients of a polymer," *Polymers*, vol. 14, no. 22, p. 4966, Jan. 2022. doi: 10.3390/polym14224966 .

[75] Y. Chen, Y. Zheng, D. Liang, Y. Zhang, J. Guo, S. Lian, Y. Yu, C. Du, and S. Ruan, "Fiber-tip Fabry–Perot cavity pressure sensor with UV-curable polymer film based on suspension curing method," *IEEE Sensors J.*, vol. 22, no. 7, pp. 6651–6660, Apr. 2022. doi: 10.1109/JSEN.2022.3153993 .

[76] H.-C. Li, M.-Y. Wang, B. Liu, J. Liu, Q. Wang, X.-D. He, H. Ping Chan, D. Wang, J. Yuan, and Q. Wu, "Temperature-independent relative humidity sensing properties of polymer micro-bottle resonators coated with graphene oxide," *Measurement*, vol. 196, p. 111199, Jun. 2022. doi: 10.1016/j.measurement.2022.111199 .

[77] J. Hu, Y. Chen, Z. Ma, L. Zeng, D. Zhou, Z. Peng, W. Sun, and Y. Liu, "Temperature-compensated optical fiber sensor for volatile organic compound gas detection based on cholesteric liquid crystal," *Opt. Lett.*, vol. 46, no. 14, p. 3324, Jul. 2021. doi: 10.1364/ol.427606 .

[78] M. Han and A. Wang, "Temperature compensation of optical microresonators using a surface layer with negative thermo-optic coefficient," *Opt. Lett.*, vol. 32, no. 13, p. 1800, Jun. 2007. doi: 10.1364/ol.32.001800 .

[79] Y. Hirata and V. Ducruet, "Effect of temperature on the solubility of aroma compounds in polyethylene film," *Polym. Test.*, vol. 25, no. 5, pp. 690–696, Aug. 2006. doi: 10.1016/j.polymertesting.2006.03.006 .

[80] J. H. Hildebrand and R. L. Scott, "Solutions of nonelectrolytes," *Annu. Rev. Phys. Chem.*, vol. 1, no. 1, pp. 75–92, Oct. 1950. doi: 10.1146/annurev.pc.01.100150.000451 .

[81] C. Hansen, *Hansen solubility parameters : a user's handbook*. Boca Raton: CRC Press, 2007.

[82] J. E. Saunders, H. Chen, C. Brauer, M. Clayton, and H.-P. Loock, "Two distinct mechanisms upon absorption of volatile organic compounds into siloxane polymers," *Soft Matter*, vol. 14, no. 12, pp. 2206–2218, 2018. doi: 10.1039/c7sm02234d .

[83] L. Laplatine, M. Fournier, N. Gaignebet, Y. Hou, R. Mathey, C. Herrier, J. Liu, D. Descloux, B. Gautheron, and T. Livache, "Silicon photonic olfactory sensor based on an array of 64 biofunctionalized Mach-Zehnder interferometers," *Opt. Express*, vol. 30, no. 19, p. 33955, Sep. 2022. doi: 10.1364/oe.461858 .

[84] J. R. Askim, M. Mahmoudi, and K. S. Suslick, "Optical sensor arrays for chemical sensing: The optoelectronic nose," *Chem. Soc. Rev.*, vol. 42, no. 22, p. 8649, 2013. doi: 10.1039/c3cs60179j .

[85] U. Lange, N. V. Roznyatovskaya, and V. M. Mirsky, "Conducting polymers in chemical sensors and arrays," *Anal. Chim. Acta*, vol. 614, no. 1, pp. 1–26, Apr. 2008. doi: 10.1016/j.aca.2008.02.068 .

[86] N. Bavili, T. Balkan, B. Morova, M. Eryürek, Y. Uysallı, S. Kaya, and A. Kiraz, "Highly sensitive optical sensor for hydrogen gas based on a polymer microcylinder ring resonator," *Sens. Actuators, B*, vol. 310, p. 127806, May 2020. doi: 10.1016/j.snb.2020.127806 .

[87] U. Yaqoob and M. I. Younis, "Chemical gas sensors: Recent developments, challenges, and the potential of machine learning—A review," *Sensors-basel.*, vol. 21, no. 8, p. 2877, Apr. 2021. doi: 10.3390/s21082877 .

[88] X. Liu, S. Cheng, H. Liu, S. Hu, D. Zhang, and H. Ning, "A survey on gas sensing technology," *Sensors-basel.*, vol. 12, no. 7, pp. 9635–9665, Jul. 2012. doi: 10.3390/s120709635 .

[89] H. Liu, L. Zhang, K. H. H. Li, and O. K. Tan, "Microhotplates for metal oxide semiconductor gas sensor applications—Towards the CMOS-MEMS monolithic approach," *Micromachines*, vol. 9, no. 11, p. 557, Oct. 2018. doi: 10.3390/mi9110557 .

[90] C. Fabry and A. Pérot, "Théorie et applications d'une nouvelle méthode de spectroscopie interférentielle," *Ann. de Chim. et de Phys.*, 1899.

[91] C. Errando-Herranz, F. Niklaus, G. Stemme, and K. B. Gylfason, "Low-power microelectromechanically tunable silicon photonic ring resonator add-drop filter," *Opt. Lett.*, vol. 40, no. 15, p. 3556, Jul. 2015. doi: 10.1364/ol.40.003556 .

[92] G. Brunetti, F. Dell'Olio, D. Conteduca, M. N. Armenise, and C. Ciminelli, "Ultracompact tuneable notch filter using silicon photonic crystal ring resonator," *J. Lightwave Technol.*, vol. 37, no. 13, pp. 2970–2980, Jul. 2019. doi: 10.1109/jlt.2019.2908364 .

[93] I. Martincek, M. Goraus, and D. Kacik, "Optical measurement of the swelling behavior of PDMS in organic solvent vapors," *Polym. Test.*, vol. 121, p. 108001, Apr. 2023. doi: 10.1016/j.polymertesting.2023.108001 .

[94] L. Rayleigh, "CXII. the problem of the whispering gallery," *The London, Edinburgh, and Dublin Philosophical Magazine and Journal of Science*, vol. 20, no. 120, pp. 1001–1004, Dec. 1910. doi: 10.1080/14786441008636993 .

[95] K. J. Vahala, "Optical microcavities," *Nature*, vol. 424, no. 6950, pp. 839–846, Aug. 2003. doi: 10.1038/nature01939 .

[96] Y. Yang, F. Lei, S. Kasumie, L. Xu, J. M. Ward, L. Yang, and S. Nic Chormaic, "Tunable erbium-doped microbubble laser fabricated by sol-gel coating," *Opt. Express*, vol. 25, no. 2, p. 1308, Jan. 2017. doi: 10.1364/oe.25.001308 .

[97] P. Wang, W. Cheng, M. Lu, G. Hu, and B. Yun, "Investigating mode characteristics of an ultra-high Q silicon nitride micro-disk resonator and high resolution microwave photonic filtering," *J. Lightwave Technol.*, pp. 1–8, 2024. doi: 10.1109/jlt.2024.3438271 .

[98] C. Junge, S. Nickel, D. O'Shea, and A. Rauschenbeutel, "Bottle microresonator with actively stabilized evanescent coupling," *Opt. Lett.*, vol. 36, no. 17, p. 3488, Sep. 2011. doi: 10.1364/ol.36.003488 .

[99] Y.-Q. Hu, H. Yang, T. Wang, X. Mao, R.-R. Xie, J.-Y. Liang, G.-Q. Qin, M. Wang, and G.-L. Long, "A novel method to fabricate on-chip ultra-high-Q microtoroid resonators," *Opt. Commun.*, vol. 476, p. 126259, Dec. 2020. doi: 10.1016/j.optcom.2020.126259 .

[100] M. W. Puckett *et al.*, "422 million intrinsic quality factor planar integrated all-waveguide resonator with sub-MHz linewidth," *Nat. Commun.*, vol. 12, no. 1, Feb. 2021. doi: 10.1038/s41467-021-21205-4 .

[101] L. Wu, H. Wang, Q. Yang, Q.-x. Ji, B. Shen, C. Bao, M. Gao, and K. Vahala, "Greater than one billion Q factor for on-chip microresonators," *Opt. Lett.*, vol. 45, no. 18, p. 5129, Sep. 2020. doi: 10.1364/ol.394940 .

[102] A. A. Savchenkov, A. B. Matsko, V. S. Ilchenko, and L. Maleki, "Optical resonators with ten million finesse," *Opt. Express*, vol. 15, no. 11, p. 6768, 2007. doi: 10.1364/oe.15.006768 .

[103] Y. Zhan, F. Hou, S. Feng, X. Wang, W. Sun, J. Ye, and Y. Zhang, "The distribution and evolution of refractive index in a polystyrene whispering gallery microcavity during glass transition," *Adv. Opt. Mater.*, vol. 10, no. 17, p. 2102548, Jun. 2022. doi: 10.1002/adom.202102548 .

[104] M. de Goede, L. Chang, J. Mu, M. Dijkstra, R. Obregón, E. Martínez, L. Padilla, F. Mitjans, and S. M. Garcia-Blanco, "Al_2O_3:Yb^{3+} integrated microdisk laser label-free biosensor," *Opt. Lett.*, vol. 44, no. 24, p. 5937, Dec. 2019. doi: 10.1364/ol.44.005937 .

[105] T. Wienhold *et al.*, "All-polymer photonic sensing platform based on whispering-gallery mode microgoblet lasers," *Lab Chip*, vol. 15, no. 18, pp. 3800–3806, 2015. doi: 10.1039/c5lc00670h .

[106] J. Zhu, Ş. K. Özdemir, L. He, D.-R. Chen, and L. Yang, "Single virus and nanoparticle size spectrometry by whispering-gallery-mode microcavities," *Opt. Express*, vol. 19, no. 17, p. 16195, Aug. 2011. doi: 10.1364/oe.19.016195 .

[107] R. M. Graybill, C. S. Para, and R. C. Bailey, "PCR-free, multiplexed expression profiling of microRNAs using silicon photonic microring resonators," *Anal. Chem.*, vol. 88, no. 21, pp. 10 347–10 351, Oct. 2016. doi: 10.1021/acs.analchem.6b03350 .

[108] J. Zhu, G. Zhao, I. Savukov, and L. Yang, "Polymer encapsulated microcavity optomechanical magnetometer," *Sci. Rep.*, vol. 7, no. 1, Aug. 2017. doi: 10.1038/s41598-017-08875-1 .

[109] Y. Yang, S. Saurabh, J. M. Ward, and S. Nic Chormaic, "High-Q, ultrathin-walled microbubble resonator for aerostatic pressure sensing," *Opt. Express*, vol. 24, no. 1, p. 294, Jan. 2016. doi: 10.1364/oe.24.000294 .

[110] X. Ou, B. Tang, P. Zhang, B. Li, F. Sun, R. Liu, K. Huang, L. Xie, Z. Li, and Y. Yang, "Microring resonator based on polarization multiplexing for simultaneous sensing of refractive index and temperature on silicon platform," *Opt. Express*, vol. 30, no. 14, p. 25627, Jun. 2022. doi: 10.1364/oe.459743 .

[111] H. Li, B. Sun, Y. Yuan, and J. Yang, "Guanidine derivative polymer coated microbubble resonator for high sensitivity detection of CO_2 gas concentration," *Opt. Express*, vol. 27, no. 3, p. 1991, Jan. 2019. doi: 10.1364/oe.27.001991 .

[112] B. Han, F. Xia, Z.-w. Zhang, M. Wang, and Y.-n. Zhang, "Acetone gas sensor based on PVA self-assembled WGM microbottle resonator coated with PDMS," *Opt. Fiber Technol.*, vol. 80, p. 103383, Oct. 2023. doi: 10.1016/j.yofte.2023.103383 .

[113] B. Yao *et al.*, "Graphene-enhanced brillouin optomechanical microresonator for ultrasensitive gas detection," *Nano Lett.*, vol. 17, no. 8, pp. 4996–5002, Jul. 2017. doi: 10.1021/acs.nanolett.7b02176 .

[114] Y.-n. Zhang, M. Wang, N. Zhu, B. Han, and Y. Liu, "Optical fiber hydrogen sensor based on self-assembled PDMS/Pd-WO_3 microbottle resonator," *Sens. Actuators, B*, vol. 375, p. 132866, Jan. 2023. doi: 10.1016/j.snb.2022.132866 .

[115] M. A. M. Johari, R. Apsari, and M. Yasin, "Comparative study an effect of polymethyl methacrylate coating on optical microbottle resonator for enhancing sensing performance for ethanol liquid sensor," *Microw. Opt. Techn. Let.*, vol. 65, no. 2, pp. 690–696, Nov. 2022. doi: 10.1002/mop.33514 .

[116] Y. Kong *et al.*, "Integration of a metal–organic framework film with a tubular whispering-gallery-mode microcavity for effective CO_2 sensing," *ACS Appl. Mater. Interfaces*, vol. 13, no. 48, pp. 58 104–58 113, Nov. 2021. doi: 10.1021/acsami.1c16322 .

[117] Q.-L. Huang, H.-L. Xu, M.-T. Li, Z.-S. Hou, C. Lv, X.-P. Zhan, H.-L. Li, H. Xia, H.-Y. Wang, and H.-B. Sun, "Stretchable PEG-DA hydrogel-based whispering-gallery-mode microlaser with humidity responsiveness," *J. Lightwave Technol.*, vol. 36, no. 3, pp. 819–824, Feb. 2018. doi: 10.1109/jlt.2017.2762696 .

[118] C. Li, T. Lohrey, P.-D. Nguyen, Z. Min, Y. Tang, C. Ge, Z. P. Sercel, E. McLeod, B. M. Stoltz, and J. Su, "Part-per-trillion trace selective gas detection using frequency locked

whispering-gallery mode microtoroids," *ACS Appl. Mater. Interfaces*, vol. 14, no. 37, pp. 42 430–42 440, Sep. 2022. doi: 10.1021/acsami.2c11494 .

[119] Y. Xu, A. M. Stanko, C. S. Cerione, T. D. Lohrey, E. McLeod, B. M. Stoltz, and J. Su, "Low part-per-trillion, humidity resistant detection of nitric oxide using microtoroid optical resonators," *ACS Appl. Mater. Interfaces*, vol. 16, no. 4, pp. 5120–5128, Jan. 2024. doi: 10.1021/acsami.3c16012 .

[120] A. K. Mallik, G. Farrell, D. Liu, V. Kavungal, Q. Wu, and Y. Semenova, "Silica gel coated spherical micro resonator for ultra-high sensitivity detection of ammonia gas concentration in air," *Sci. Rep.*, vol. 8, no. 1, Jan. 2018. doi: 10.1038/s41598-018-20025-9 .

[121] J. Wang, J. Li, S. Sun, H. Dong, L. Wu, E. Zhao, F. He, X. Ma, and Y. S. Zhao, "Revealing molecular diffusion dynamics in polymer microspheres by optical resonances," *Sci. Adv.*, vol. 9, no. 19, May 2023. doi: 10.1126/sciadv.adf1725 .

[122] Y. Guo *et al.*, "A monolithic graphene-functionalized microlaser for multispecies gas detection," *Advanced Materials*, vol. 34, no. 51, Nov. 2022. doi: 10.1002/adma.202207777 .

[123] H. Hassanin, G. Sheikholeslami, P. Sareh, and R. B. Ishaq, "Microadditive manufacturing technologies of 3D microelectromechanical systems," *Adv. Eng. Mater.*, vol. 23, no. 12, Oct. 2021. doi: 10.1002/adem.202100422 .

[124] H. Klippstein, A. Diaz De Cerio Sanchez, H. Hassanin, Y. Zweiri, and L. Seneviratne, "Fused deposition modeling for unmanned aerial vehicles (UAVs): A review," *Adv. Eng. Mater.*, vol. 20, no. 2, Sep. 2017. doi: 10.1002/adem.201700552 .

[125] A. Awad, S. J. Trenfield, S. Gaisford, and A. W. Basit, "3D printed medicines: A new branch of digital healthcare," *Int. J. Pharmaceut.*, vol. 548, no. 1, pp. 586–596, Sep. 2018. doi: 10.1016/j.ijpharm.2018.07.024 .

[126] M. Gao, L. Li, and Y. Song, "Inkjet printing wearable electronic devices," *J. Mater. Chem. C*, vol. 5, no. 12, pp. 2971–2993, 2017. doi: 10.1039/c7tc00038c .

[127] J. Dai, O. Ogbeide, N. Macadam, Q. Sun, W. Yu, Y. Li, B.-L. Su, T. Hasan, X. Huang, and W. Huang, "Printed gas sensors," *Chem. Soc. Rev.*, vol. 49, no. 6, pp. 1756–1789, 2020. doi: 10.1039/C9CS00459A .

[128] A. Zolfaghari, T. Chen, and A. Y. Yi, "Additive manufacturing of precision optics at micro and nanoscale," *Int. J. Extrem. Manuf.*, vol. 1, no. 1, p. 012005, Apr. 2019. doi: 10.1088/2631-7990/ab0fa5 .

[129] J. Yang, Y. Li, Y. Zheng, Y. Xu, Z. Zheng, X. Chen, and W. Liu, "Versatile aerogels for sensors," *Small*, vol. 15, no. 41, Sep. 2019. doi: 10.1002/smll.201902826 .

[130] X. Sui, J. R. Downing, M. C. Hersam, and J. Chen, "Additive manufacturing and applications of nanomaterial-based sensors," *Mater. Today*, vol. 48, pp. 135–154, Sep. 2021. doi: 10.1016/j.mattod.2021.02.001 .

[131] P. Wei, H. Leng, Q. Chen, R. C. Advincula, and E. B. Pentzer, "Reprocessable 3D-printed conductive elastomeric composite foams for strain and gas sensing," *ACS Applied Polymer Materials*, vol. 1, no. 4, pp. 885–892, Mar. 2019. doi: 10.1021/acsapm.9b00118 .

[132] Y. Seekaew, S. Lokavee, D. Phokharatkul, A. Wisitsoraat, T. Kerdcharoen, and C. Wongchoosuk, "Low-cost and flexible printed graphene–PEDOT:PSS gas sensor for ammonia detection," *Org. Electron.*, vol. 15, no. 11, pp. 2971–2981, Nov. 2014. doi: 10.1016/j.orgel.2014.08.044 .

[133] A. Rivadeneyra and J. A. López-Villanueva, "Recent advances in printed capacitive sensors," *Micromachines*, vol. 11, no. 4, p. 367, Apr. 2020. doi: 10.3390/mi11040367 .

[134] N. Van Hieu, "Highly reproducible synthesis of very large-scale tin oxide nanowires used for screen-printed gas sensor," *Sens. Actuators, B*, vol. 144, no. 2, pp. 425–431, Feb. 2010. doi: 10.1016/j.snb.2009.02.043 .

[135] T. Syrový, P. Kuberský, I. Sapurina, S. Pretl, P. Bober, L. Syrová, A. Hamáček, and J. Stejskal, "Gravure-printed ammonia sensor based on organic polyaniline colloids," *Sens. Actuators, B*, vol. 225, pp. 510–516, Mar. 2016. doi: 10.1016/j.snb.2015.11.062 .

[136] S. Maruo and J. Fourkas, "Recent progress in multiphoton microfabrication," *Laser Photonics Rev.*, vol. 2, no. 1–2, pp. 100–111, Apr. 2008. doi: 10.1002/lpor.200710039 .

[137] H. H. Duc Nguyen, U. Hollenbach, U. Ostrzinski, K. Pfeiffer, S. Hengsbach, and J. Mohr, "Freeform three-dimensional embedded polymer waveguides enabled by external-diffusion assisted two-photon lithography," *Appl. Optics*, vol. 55, no. 8, p. 1906, Mar. 2016. doi: 10.1364/ao.55.001906 .

[138] S. Feng, Q. Liu, Y. Zhan, W. Sun, X. Wang, J.-S. Ye, S. Zhang, and Y. Zhang, "An 'optical tentacle' of suspended polymer micro-rings on a multicore fiber facet for vapor sensing," *Opt. Express*, Mar. 2020. doi: 10.1364/oe.390145 .

[139] J. Gawedzinski, M. E. Pawlowski, and T. S. Tkaczyk, "Quantitative evaluation of performance of three-dimensional printed lenses," *Opt. Eng.*, vol. 56, no. 08, p. 1, Aug. 2017. doi: 10.1117/1.oe.56.8.084110 .

[140] *Fundamentals of Inkjet Printing: The Science of Inkjet and Droplets.* Wiley, Jan. 2016. doi: 10.1002/9783527684724 .

[141] R. E. Saunders and B. Derby, "Inkjet printing biomaterials for tissue engineering: Bioprinting," *Int. Mater. Rev.*, vol. 59, no. 8, pp. 430–448, Jul. 2014. doi: 10.1179/1743280414y.0000000040 .

[142] A. C. Fischer, M. Mäntysalo, and F. Niklaus, "Inkjet printing, laser-based micromachining and micro 3D printing technologies for MEMS," in *Handbook of Silicon Based MEMS Materials and Technologies.* Elsevier, 2015, pp. 550–564. doi: 10.1016/b978-0-323-29965-7.00026-9 .

[143] Y. Liu and B. Derby, "Experimental study of the parameters for stable drop-on-demand inkjet performance," *Phys. Fluids*, vol. 31, no. 3, p. 032004, Mar. 2019. doi: 10.1063/1.5085868 .

[144] S.-H. Kang, S. Kim, D. K. Sohn, and H. S. Ko, "Analysis of drop-on-demand piezo inkjet performance," *Phys. Fluids*, vol. 32, no. 2, p. 022007, Feb. 2020. doi: 10.1063/1.5142023 .

[145] Z. Du, X. Yu, and Y. Han, "Inkjet printing of viscoelastic polymer inks," *Chinese Chem. Lett.*, vol. 29, no. 3, pp. 399–404, Mar. 2018. doi: 10.1016/j.cclet.2017.09.031 .

[146] D. Soltman and V. Subramanian, "Inkjet-printed line morphologies and temperature control of the coffee ring effect," *Langmuir*, vol. 24, no. 5, pp. 2224–2231, Mar. 2008. doi: 10.1021/la7026847 .

[147] C. Trudeau, M. Bolduc, P. Beaupré, J. Benavides-Guerrero, B. Tremblay, and S. G. Cloutier, "Inkjet-printing of methylammonium lead trihalide perovskite as active layers for optoelectronic devices," *MRS Advances*, vol. 3, no. 32, pp. 1837–1842, 2018. doi: 10.1557/adv.2018.172 .

[148] F. Mathies, P. Brenner, G. Hernandez-Sosa, I. A. Howard, U. W. Paetzold, and U. Lemmer, "Inkjet-printed perovskite distributed feedback lasers," *Opt. Express*, vol. 26, no. 2, p. A144, Jan. 2018. doi: 10.1364/oe.26.00a144 .

[149] A. F. Sartori, P. Belardinelli, R. J. Dolleman, P. G. Steeneken, M. K. Ghatkesar, and J. G. Buijnsters, "Inkjet-printed high-Q nanocrystalline diamond resonators," *Small*, vol. 15, no. 4, p. 1803774, Dec. 2018. doi: 10.1002/smll.201803774 .

[150] H. C. Nallan, J. A. Sadie, R. Kitsomboonloha, S. K. Volkman, and V. Subramanian, "Systematic design of jettable nanoparticle-based inkjet inks: Rheology, acoustics, and jettability," *Langmuir*, vol. 30, no. 44, pp. 13 470–13 477, Oct. 2014. doi: 10.1021/la502903y .

[151] B. Derby, "Inkjet printing ceramics: From drops to solid," *J. Eur. Ceram. Soc.*, vol. 31, no. 14, pp. 2543–2550, Nov. 2011. doi: 10.1016/j.jeurceramsoc.2011.01.016 .

[152] J. Godleman, T. S. Babra, A. Afsar, A. Kyriacou, M. Thompson, J. L. Harries, H. M. Colquhoun, and W. Hayes, "Functionalised PEGs with photo-dimerisable, anthracenyl end-groups: New UV-curable materials for use in inkjet formulations," *Prog. Org. Coat.*, vol. 151, p. 106105, Feb. 2021. doi: 10.1016/j.porgcoat.2020.106105 .

[153] G. F. Acosta-Vélez, T. Z. Zhu, C. S. Linsley, and B. M. Wu, "Photocurable poly(ethylene glycol) as a bioink for the inkjet 3D pharming of hydrophobic drugs," *Int. J. Pharmaceut.*, vol. 546, no. 1-2, pp. 145–153, Jul. 2018. doi: 10.1016/j.ijpharm.2018.04.056 .

[154] Z. Tang, K. Fang, Y. Song, and F. Sun, "Jetting performance of polyethylene glycol and reactive dye solutions," *Polymers*, vol. 11, no. 4, p. 739, Apr. 2019. doi: 10.3390/polym11040739 .

[155] R. Mikkonen, P. Puistola, I. Jönkkäri, and M. Mäntysalo, "Inkjet printable polydimethylsiloxane for all-inkjet-printed multilayered soft electrical applications," *ACS Applied Materials & Interfaces*, vol. 12, no. 10, pp. 11 990–11 997, Feb. 2020. doi: 10.1021/acsami.9b19632 .

[156] C. Sturgess, C. J. Tuck, I. A. Ashcroft, and R. D. Wildman, "3D reactive inkjet printing of polydimethylsiloxane," *J. Mater. Chem. C*, vol. 5, no. 37, pp. 9733–9743, Aug. 2017. doi: 10.1039/c7tc02412f .

[157] R. Bernasconi, M. C. Angeli, F. Mantica, D. Carniani, and L. Magagnin, "SU-8 inkjet patterning for microfabrication," *Polymer*, vol. 185, p. 121933, Dec. 2019. doi: 10.1016/j.polymer.2019.121933 .

[158] P. Šuly, P. Krčmár, J. Mašlík, P. Urbánek, and I. Kuritka, "Poly(vinyl alcohol): Formulation of a polymer ink for the patterning of substrates with a drop-on-demand

inkjet printer," *Materiali in tehnologije*, vol. 51, no. 1, pp. 41–48, Feb. 2017. doi: 10.17222/mit.2015.180 .

[159] J. S. Wheeler and S. G. Yeates, "Polymers in inkjet printing," in *Fundamentals of Inkjet Printing*. Wiley-VCH Verlag GmbH & Co. KGaA, Dec. 2015, pp. 117–140. doi: 10.1002/9783527684724.ch5 .

[160] D. Xu, V. Sanchez-Romaguera, S. Barbosa, W. Travis, J. de Wit, P. Swan, and S. G. Yeates, "Inkjet printing of polymer solutions and the role of chain entanglement," *J. Mater. Chem.*, vol. 17, no. 46, p. 4902, 2007. doi: 10.1039/b710879f .

[161] S. D. Hoath, D. C. Vadillo, O. G. Harlen, C. McIlroy, N. F. Morrison, W.-K. Hsiao, T. R. Tuladhar, S. Jung, G. D. Martin, and I. M. Hutchings, "Inkjet printing of weakly elastic polymer solutions," *J. Non-Newtonian Fluid Mech.*, vol. 205, pp. 1–10, Mar. 2014. doi: 10.1016/j.jnnfm.2014.01.002 .

[162] C. McIlroy, O. G. Harlen, and N. F. Morrison, "Modelling the jetting of dilute polymer solutions in drop-on-demand inkjet printing," *J. Non-Newtonian Fluid Mech.*, vol. 201, pp. 17–28, Nov. 2013. doi: 10.1016/j.jnnfm.2013.05.007 .

[163] Y.-L. Sung, J. Jeang, C.-H. Lee, and W.-C. Shih, "Fabricating optical lenses by inkjet printing and heat-assistedin situcuring of polydimethylsiloxane for smartphone microscopy," *J. Biomed. Opt.*, vol. 20, no. 4, p. 047005, Apr. 2015. doi: 10.1117/1.jbo.20.4.047005 .

[164] C. M. Cole, S. V. Kunz, P. E. Shaw, N.-P. Thoebes, T. Baumann, E. Blasco, J. P. Blinco, P. Sonar, C. Barner-Kowollik, and S. D. Yambem, "A printable thermally activated delayed fluorescence polymer light emitting diode," *J. Mater. Chem. C*, vol. 8, no. 37, pp. 13 001–13 009, 2020. doi: 10.1039/d0tc02735a .

[165] M. Saito and K. Koyama, "Deformable microdroplet cavity fabricated by an inkjet method," *Jpn. J. Appl. Phys.*, vol. 49, no. 9, p. 092501, Sep. 2010. doi: 10.1143/jjap.49.092501 .

[166] Y. Mikami, S. Ryu, C. Chen, N. Nishimura, H. Yoshioka, and Y. Oki, "Water-like-refractive-index microdisk cavity by the ink-jet printing method," in *2017 Conference on Lasers and Electro-Optics Europe & European Quantum Electronics Conference (CLEO/Europe-EQEC)*. IEEE, Jun. 2017. doi: 10.1109/cleoe-eqec.2017.8086631 .

[167] L. Cai, J. Pan, and S. Hu, "Overview of the coupling methods used in whispering gallery mode resonator systems for sensing," *Opt. Laser. Eng.*, vol. 127, p. 105968, Apr. 2020. doi: 10.1016/j.optlaseng.2019.105968 .

[168] Y. Zhang, Q. Song, D. Zhao, X. Tang, Y. Zhang, Z. Liu, and L. Yuan, "Review of different coupling methods with whispering gallery mode resonator cavities for sensing," *Opt. Laser Technol.*, vol. 159, p. 108955, Apr. 2023. doi: 10.1016/j.optlastec.2022.108955 .

[169] A. Samusjew, M. Kratzer, A. Moser, C. Teichert, K. K. Krawczyk, and T. Griesser, "Inkjet printing of soft, stretchable optical waveguides through the photopolymerization of high-profile linear patterns," *ACS Applied Materials & Interfaces*, vol. 9, no. 5, pp. 4941–4947, Jan. 2017. doi: 10.1021/acsami.6b13272 .

[170] T. Wolfer, P. Bollgruen, D. Mager, L. Overmeyer, and J. G. Korvink, "Flexographic and inkjet printing of polymer optical waveguides for fully integrated sensor systems," *Procedia Technol.*, vol. 15, pp. 521–529, 2014. doi: 10.1016/j.protcy.2014.09.012 .

[171] F. van Schoonhoven, Y. Tomishige, A. Abazi, A. Sánchez-Postigo, J. Chen, Y. Mikami, N. Tate, Y. Oki, C. Schuck, and H. Yoshioka, "Inkjet-printed waveguide-coupled passive wedge-shaped microdisk resonator with refractive index tunability," *Opt. Mater. Express*, vol. 14, no. 7, p. 1767, Jun. 2024. doi: 10.1364/ome.528582 .

[172] S. Y. Siew *et al.*, "Review of silicon photonics technology and platform development," *J. Lightwave Technol.*, vol. 39, no. 13, pp. 4374–4389, Jul. 2021. doi: 10.1109/jlt.2021.3066203 .

[173] F. Gardes *et al.*, "A review of capabilities and scope for hybrid integration offered by silicon-nitride-based photonic integrated circuits," *Sensors-basel.*, vol. 22, no. 11, p. 4227, Jun. 2022. doi: 10.3390/s22114227 .

[174] C. Xiang, W. Jin, and J. E. Bowers, "Silicon nitride passive and active photonic integrated circuits: trends and prospects," *Photonics Res.*, vol. 10, no. 6, p. A82, May 2022. doi: 10.1364/prj.452936 .

[175] D. D. John, M. J. R. Heck, J. F. Bauters, R. Moreira, J. S. Barton, J. E. Bowers, and D. J. Blumenthal, "Multilayer platform for ultra-low-loss waveguide applications," *IEEE Photonics Technology Letters*, vol. 24, no. 11, pp. 876–878, Jun. 2012. doi: 10.1109/lpt.2012.2189762 .

[176] W. D. Sacher *et al.*, "Multilayer silicon nitride-on-silicon integrated photonic platform for 3D photonic circuits," in *Conference on Lasers and Electro-Optics*. OSA, 2016. doi: 10.1364/cleo_at.2016.jth4c.3 .

[177] K. Shang, S. Pathak, B. Guan, G. Liu, and S. J. B. Yoo, "Low-loss compact multilayer silicon nitride platform for 3D photonic integrated circuits," *Opt. Express*, vol. 23, no. 16, p. 21334, Aug. 2015. doi: 10.1364/oe.23.021334 .

[178] M. Ghulinyan, R. Guider, G. Pucker, and L. Pavesi, "Monolithic whispering-gallery mode resonators with vertically coupled integrated bus waveguides," *IEEE Photonics Technol. Lett.*, vol. 23, no. 16, pp. 1166–1168, Aug. 2011. doi: 10.1109/LPT.2011.2157487 .

[179] F. Ramiro-Manzano, N. Prtljaga, L. Pavesi, G. Pucker, and M. Ghulinyan, "A fully integrated high-Q whispering-gallery wedge resonator," *Opt. Express*, vol. 20, no. 20, p. 22934, Sep. 2012. doi: 10.1364/oe.20.022934 .

[180] M. Ghulinyan, F. Ramiro-Manzano, N. Prtljaga, R. Guider, I. Carusotto, A. Pitanti, G. Pucker, and L. Pavesi, "Oscillatory vertical coupling between a whispering-gallery resonator and a bus waveguide," *Phys. Rev. Lett.*, vol. 110, no. 16, p. 163901, Apr. 2013. doi: 10.1103/physrevlett.110.163901 .

[181] F. Turri, F. Ramiro-Manzano, I. Carusotto, M. Ghulinyan, G. Pucker, and L. Pavesi, "Wavelength dependence of a vertically coupled resonator-waveguide system," *J. Lightwave Technol.*, vol. 34, no. 23, pp. 5385–5390, Dec. 2016. doi: 10.1109/jlt.2016.2615331 .

[182] M.-A. Bianki, C. Lemieux-Leduc, R. Guertin, and Y.-A. Peter, "Mutlilayer wedge disks CROW for an optical delay line," *J. Lightwave Technol.*, vol. 40, no. 3, pp. 770–775, Feb. 2022. doi: 10.1109/jlt.2022.3142161 .

[183] D. Gandolfi, F. Ramiro-Manzano, F. A. Rebollo, M. Ghulinyan, G. Pucker, and L. Pavesi, "Role of edge inclination in an optical microdisk resonator for label-free sensing," *Sensors-basel.*, vol. 15, no. 3, pp. 4796–4809, Feb. 2015. doi: 10.3390/s150304796 .

[184] J. Bures, "Optique guidée : fibres optiques et composants passifs tout-fibre," *Presses interPolytechnique*, 2009.

[185] M. Borselli, T. J. Johnson, and O. Painter, "Beyond the Rayleigh scattering limit in high-Q silicon microdisks: Theory and experiment," *Opt. Express*, vol. 13, no. 5, p. 1515, 2005. doi: 10.1364/opex.13.001515 .

[186] A. Ramier, "Intégration de guides d'onde et microrésonateurs à modes de galerie par assemblage à puce retournée," Master's thesis, École Polytechnique de Montréal, août 2014.

[187] H. Haus and W. Huang, "Coupled-mode theory," *Proc. IEEE*, vol. 79, no. 10, pp. 1505–1518, Oct. 1991. doi: 10.1109/5.104225 .

[188] W.-P. Huang, "Coupled-mode theory for optical waveguides: An overview," *JOSA A*, vol. 11, no. 3, pp. 963–983, Mar. 1994. doi: 10.1364/JOSAA.11.000963 .

[189] G. Griffel, J. Connolly, N. Morris, S. Arnold, D. Taskent, and A. Serpengüzel, "Morphology-dependent resonances of a microsphere–optical fiber system," *Opt. Lett.*, vol. 21, no. 10, p. 695, May 1996. doi: 10.1364/ol.21.000695 .

[190] S. Arnold, M. Khoshsima, I. Teraoka, S. Holler, and F. Vollmer, "Shift of whispering-gallery modes in microspheres by protein adsorption," *Opt. Lett.*, vol. 28, no. 4, p. 272, Feb. 2003. doi: 10.1364/ol.28.000272 .

[191] J. T. Robinson, L. Chen, and M. Lipson, "On-chip gas detection in silicon optical microcavities," *Opt. Express*, vol. 16, no. 6, p. 4296, Mar. 2008. doi: 10.1364/oe.16.004296 .

[192] L. Shao, X.-F. Jiang, X.-C. Yu, B.-B. Li, W. R. Clements, F. Vollmer, W. Wang, Y.-F. Xiao, and Q. Gong, "Detection of single nanoparticles and lentiviruses using microcavity resonance broadening," *Adv. Mater.*, vol. 25, no. 39, pp. 5616–5620, Aug. 2013. doi: 10.1002/adma201302572 .

[193] J. Zhu, S. K. Ozdemir, Y.-F. Xiao, L. Li, L. He, D.-R. Chen, and L. Yang, "On-chip single nanoparticle detection and sizing by mode splitting in an ultrahigh-Q microresonator," *Nat. Photonics*, vol. 4, no. 1, pp. 46–49, Dec. 2009. doi: 10.1038/nphoton.2009.237 .

[194] T. J. Kippenberg, "Particle sizing by mode splitting," *Nat. Photonics*, vol. 4, no. 1, pp. 9–10, Jan. 2010. doi: 10.1038/nphoton.2009.246 .

[195] I. M. White and X. Fan, "On the performance quantification of resonant refractive index sensors," *Opt. Express*, vol. 16, no. 2, p. 1020, 2008. doi: 10.1364/oe.16.001020 .

[196] J. Crank, Ed., *Diffusion in polymers*, 3rd ed. London: Acad. Pr., 1977.

[197] C. Liu, Y. Liu, M. Sokuler, D. Fell, S. Keller, A. Boisen, H.-J. Butt, G. K. Auernhammer, and E. Bonaccurso, "Diffusion of water into SU-8 microcantilevers," *Phys. Chem. Chem. Phys.*, vol. 12, no. 35, p. 10577, 2010. doi: 10.1039/c002478c .

[198] H. Zhao and J. Bai, "Highly sensitive piezo-resistive graphite nanoplatelet–carbon nanotube hybrids/polydimethylsilicone composites with improved conductive network construction," *ACS Appl. Mater. Interfaces*, vol. 7, no. 18, pp. 9652–9659, Apr. 2015. doi: 10.1021/acsami.5b01413 .

[199] K. I. Arshak, D. McDonagh, and M. A. Durcan, "Development of new capacitive strain sensors based on thick film polymer and cermet technologies," *Sens. Actuators, A*, vol. 79, no. 2, pp. 102–114, Feb. 2000. doi: 10.1016/S0924-4247(99)00275-7 .

[200] L. Jiang, J. Wu, K. Chen, Y. Zheng, G. Deng, X. Zhang, Z. Li, and K. S. Chiang, "Polymer waveguide Mach-Zehnder interferometer coated with dipolar polycarbonate for on-chip nitroaromatics detection," *Sens. Actuators, B*, vol. 305, p. 127406, Feb. 2020. doi: 10.1016/j.snb.2019.127406 .

[201] K. D. Heylman, K. A. Knapper, E. H. Horak, M. T. Rea, S. K. Vanga, and R. H. Goldsmith, "Optical microresonators for sensing and transduction: A materials perspective," *Adv. Mater.*, vol. 29, no. 30, p. 1700037, Jun. 2017. doi: 10.1002/adma.201700037 .

[202] P. Ji *et al.*, "In-fiber polymer microdisk resonator and its sensing applications of temperature and humidity," *ACS Appl. Mater. Interfaces*, vol. 13, no. 40, pp. 48 119–48 126, Sep. 2021. doi: 10.1021/acsami.1c14499 .

[203] S. Cichosz, A. Masek, and M. Zaborski, "Polymer-based sensors: A review," *Polym. Test.*, vol. 67, pp. 342–348, May 2018. doi: 10.1016/j.polymertesting.2018.03.024 .

[204] S. Wang, Y. Yang, P. Niu, S. Wu, S. Liu, R.-B. Jin, P. Lu, X. Hu, and N. Dai, "Fiber tip Michelson interferometer for temperature sensing based on polymer-filled suspended core fiber," *Opt. Laser Technol.*, vol. 141, p. 107147, Sep. 2021. doi: 10.1016/j.optlastec.2021.107147 .

[205] S. Han, N. U. H. Alvi, L. Granlöf, H. Granberg, M. Berggren, S. Fabiano, and X. Crispin, "A multiparameter pressure–temperature–humidity sensor based on mixed ionic–electronic cellulose aerogels," *Adv. Sci.*, vol. 6, no. 8, p. 1802128, Feb. 2019. doi: 10.1002/advs.201802128 .

[206] V. Fakhfouri, N. Cantale, G. Mermoud, J. Kim, D. Boiko, E. Charbon, A. Martinoli, and J. Brugger, "Inkjet printing of SU-8 for polymer-based MEMS a case study for microlenses," in *2008 IEEE 21st International Conference on Micro Electro Mechanical Systems*. IEEE, Jan. 2008. doi: 10.1109/memsys.2008.4443679 .

[207] A. Voigt, U. Ostrzinski, K. Pfeiffer, J. Y. Kim, V. Fakhfouri, J. Brugger, and G. Gruetzner, "New inks for the direct drop-on-demand fabrication of polymer lenses," *Microelectron. Eng.*, vol. 88, no. 8, pp. 2174–2179, Aug. 2011. doi: 10.1016/j.mee.2010.12.004 .

[208] L. Jacot-Descombes, M. R. Gullo, M. Mastrangeli, V. J. Cadarso, and J. Brugger, "Inkjet printed SU-8 hemispherical microcapsules and silicon chip embedding," *Micro & Nano Letters*, vol. 8, no. 10, pp. 633–636, Oct. 2013. doi: 10.1049/mnl.2013.0241 .

[209] C. Chen *et al.*, "Effects of edge inclination angles on whispering-gallery modes in printable wedge microdisk lasers," *Opt. Express*, vol. 26, no. 1, p. 233, Jan. 2018. doi: 10.1364/oe.26.000233 .

[210] Z. Zhang, N. Yao, J. Pan, L. Zhang, W. Fang, and L. Tong, "A new route for fabricating polymer optical microcavities," *Nanoscale*, vol. 11, no. 12, pp. 5203–5208, 2019. doi: 10.1039/C8NR10007A .

[211] *SU-8 2000 Permanent Epoxy Negative Photoresist*, MicroChem, 2015.

[212] N. Xie, T. Hashimoto, and K. Utaka, "Very low power operation of compact MMI polymer thermooptic switch," *IEEE Photonics Technology Letters*, vol. 21, no. 18, pp. 1335–1337, Sep. 2009. doi: 10.1109/lpt.2009.2025967 .

[213] Y.-F. Yan, C.-T. Zheng, L. Liang, J. Meng, X.-Q. Sun, F. Wang, and D.-M. Zhang, "Response-time improvement of a 2×2 thermo-optic switch with polymer/silica hybrid waveguide," *Opt. Commun.*, vol. 285, no. 18, pp. 3758–3762, Aug. 2012. doi: 10.1016/j.optcom.2012.05.028 .

[214] Y.-F. Liu, X.-B. Wang, J. Sun, H.-J. Gu, X.-Q. Sun, C.-M. Chen, F. Wang, and D.-M. Zhang, "Thermal field analysis of polymer/silica hybrid waveguide thermo-optic switch," *Opt. Commun.*, vol. 356, pp. 79–83, Dec. 2015. doi: 10.1016/j.optcom.2015.07.057 .

[215] R. Feng and R. J. Farris, "Influence of processing conditions on the thermal and mechanical properties of SU8 negative photoresist coatings," *J. Micromech. Microeng.*, vol. 13, no. 1, pp. 80–88, Dec. 2002. doi: 10.1088/0960-1317/13/1/312 .

[216] M. K. Gunde, N. Hauptman, M. Maček, and M. Kunaver, "The influence of hard-baking temperature applied for SU8 sensor layer on the sensitivity of capacitive chemical sensor," *Appl. Phys. A*, vol. 95, no. 3, pp. 673–680, Nov. 2008. doi: 10.1007/s00339-008-4966-4 .

[217] Z. Zhang, P. Zhao, P. Lin, and F. Sun, "Thermo-optic coefficients of polymers for optical waveguide applications," *Polymer*, vol. 47, no. 14, pp. 4893–4896, Jun. 2006. doi: 10.1016/j.polymer.2006.05.035 .

[218] M. Szczerska, "Temperature sensors based on polymer fiber optic interferometer," *Chemosensors*, vol. 10, no. 6, p. 228, Jun. 2022. doi: 10.3390/chemosensors10060228 .

[219] L. Xu, X. Jiang, G. Zhao, D. Ma, H. Tao, Z. Liu, F. G. Omenetto, and L. Yang, "High-Q silk fibroin whispering gallery microresonator," *Opt. Express*, vol. 24, no. 18, p. 20825, Aug. 2016. doi: 10.1364/oe.24.020825 .

[220] J. Williams and A. Ringsdorf, "Human odour thresholds are tuned to atmospheric chemical lifetimes," *Philosophical Transactions of the Royal Society B: Biological Sciences*, vol. 375, no. 1800, p. 20190274, Jun. 2020. doi: 10.1098/rstb.2019.0274 .

[221] S. Khan, S. L. Calvé, and D. Newport, "A review of optical interferometry techniques for VOC detection," *Sens. Actuators, A*, p. 111782, Dec. 2019. doi: 10.1016/j.sna.2019.111782 .

[222] J. R. Fried, *Polymer science and technology*, 3rd ed. Upper Saddle River, NJ: Prentice Hall, 2014.

[223] R. Haddad, R. Khan, Y. K. Takahashi, K. Mori, D. Harel, and N. Sobel, "A metric for odorant comparison," *Nat. Methods*, vol. 5, no. 5, pp. 425–429, Mar. 2008. doi: 10.1038/nmeth.1197 .

[224] T. Takagishi, H. Yoshioka, Y. Mikami, and Y. Oki, "On-demand inkjet-printed microdisk laser with air cladding by liquid flow microetching," *Appl. Optics*, vol. 59, no. 21, p. 6340, Jul. 2020. doi: 10.1364/ao.396061 .

[225] M.-A. Bianki, R. Guertin, C. Lemieux-Leduc, and Y.-A. Peter, "Temperature sensitivity control of an inkjet-printed optical resonator on pillar," *ACS Appl. Mater. Interfaces*, Jan. 2024. doi: 10.1021/acsami.3c14406 .

[226] R. Guertin, M.-A. Bianki, and Y.-A. Peter, "Low-cost fabrication of an on-chip Fabry-Perot interferometer for dry environmental monitoring," in *2023 International Conference on Optical MEMS and Nanophotonics (OMN) and SBFoton International Optics and Photonics Conference (SBFoton IOPC)*, Jul. 2023, pp. 1–2. doi: 10.1109/OMN/SBFotonIOPC58971.2023.10230951 ., iSSN: 2160-5041.

[227] W. Ma, J. Xing, R. Wang, Q. Rong, W. Zhang, Y. Li, J. Zhang, and X. Qiao, "Optical fiber Fabry–Perot interferometric CO_2 gas sensor using guanidine derivative polymer functionalized layer," *IEEE Sensors J.*, vol. 18, no. 5, pp. 1924–1929, Mar. 2018. doi: 10.1109/JSEN.2018.2790973 .

[228] S. J. Patrash and E. T. Zellers, "Characterization of polymeric surface acoustic wave sensor coatings and semiempirical models of sensor responses to organic vapors," *Anal. Chem.*, vol. 65, no. 15, pp. 2055–2066, Aug. 1993. doi: 10.1021/ac00063a021 .

[229] J. E. Saunders, H. Chen, C. Brauer, M. Clayton, W. Chen, J. A. Barnes, and H.-P. Loock, "Quantitative diffusion and swelling kinetic measurements using large-angle interferometric refractometry," *Soft Matter*, vol. 11, no. 45, pp. 8746–8757, 2015. doi: 10.1039/c5sm02170g .

[230] W. Ogieglo, H. Wormeester, M. Wessling, and N. E. Benes, "Effective medium approximations for penetrant sorption in glassy polymers accounting for excess free volume," *Polymer*, vol. 55, no. 7, pp. 1737–1744, Apr. 2014. doi: 10.1016/j.polymer.2014.02.040 .

[231] A. C. Chinellato, S. E. Vidotti, M. B. Moraes, and L. A. Pessan, "Effects of plasma etching on surface modification and gas permeability of bisphenol-A polycarbonate films," *Journal of Macromolecular Science, Part B*, vol. 46, no. 6, pp. 1165–1177, Nov. 2007. doi: 10.1080/00222340701582928 .

[232] S. D. Hoath, O. G. Harlen, and I. M. Hutchings, "Jetting behavior of polymer solutions in drop-on-demand inkjet printing," *J. Rheol.*, vol. 56, no. 5, pp. 1109–1127, Sep. 2012. doi: 10.1122/1.4724331 .

[233] Y. Son, C. Kim, D. H. Yang, and D. J. Ahn, "Spreading of an inkjet droplet on a solid surface with a controlled contact angle at low Weber and Reynolds numbers," *Langmuir*, vol. 24, no. 6, pp. 2900–2907, Mar. 2008. doi: 10.1021/la702504v .

[234] F. Ramiro-Manzano, N. Prtljaga, L. Pavesi, G. Pucker, and M. Ghulinyan, "Monolithic integration of high-Q wedge resonators with vertically coupled waveguides," in *Integrated Photonics: Materials, Devices, and Applications II*, J.-M. Fédéli, L. Vivien, and M. K. Smit, Eds., vol. 8767, International Society for Optics and Photonics. SPIE, May 2013, p. 876704. doi: 10.1117/12.2017400 .

[235] J. E. Mark, *Physical Properties of Polymers Handbook*. Springer-Verlag GmbH, 2007.

[236] D. T. Pierce and W. E. Spicer, "Electronic structure of amorphous Si from photoemission and optical studies," *Phys. Rev. B*, vol. 5, no. 8, pp. 3017–3029, Apr. 1972. doi: 10.1103/physrevb.5.3017 .

[237] L. Y. Beliaev, E. Shkondin, A. V. Lavrinenko, and O. Takayama, "Optical, structural and composition properties of silicon nitride films deposited by reactive radio-frequency sputtering, low pressure and plasma-enhanced chemical vapor deposition," *Thin Solid Films*, vol. 763, p. 139568, Dec. 2022. doi: 10.1016/j.tsf.2022.139568 .

[238] J. Kischkat *et al.*, "Mid-infrared optical properties of thin films of aluminum oxide, titanium dioxide, silicon dioxide, aluminum nitride, and silicon nitride," *Appl. Optics*, vol. 51, no. 28, p. 6789, Sep. 2012. doi: 10.1364/ao.51.006789 .

[239] L. Gao, F. Lemarchand, and M. Lequime, "Exploitation of multiple incidences spectrometric measurements for thin film reverse engineering," *Opt. Express*, vol. 20, no. 14, p. 15734, Jun. 2012. doi: 10.1364/oe.20.015734 .

[240] H. H. Li, "Refractive index of alkaline earth halides and its wavelength and temperature derivatives," *J. Phys. Chem. Ref. Data*, vol. 9, no. 1, pp. 161–290, Jan. 1980. doi: 10.1063/1.555616 .

[241] L. V. Rodríguez-de Marcos, J. I. Larruquert, J. A. Méndez, and J. A. Aznárez, "Self-consistent optical constants of MgF_2, LaF_3, and CeF_3 films," *Opt. Mater. Express*, vol. 7, no. 3, p. 989, Feb. 2017. doi: 10.1364/ome.7.000989 .

[242] C. Juntunen, A. J. Rish, C. A. Anderson, and Y. Sung, "Refractive index measurement of pharmaceutical powders in the short-wave infrared range using index matching assisted with phase imaging," *Powder Technol.*, vol. 438, p. 119621, Apr. 2024. doi: 10.1016/j.powtec.2024.119621 .

[243] X. Zhang, J. Qiu, X. Li, J. Zhao, and L. Liu, "Complex refractive indices measurements of polymers in visible and near-infrared bands," *Appl. Optics*, vol. 59, no. 8, p. 2337, Mar. 2020. doi: 10.1364/ao.383831 .

[244] Y. Hanada, T. Ogawa, K. Koike, and K. Sugioka, "Making the invisible visible: A microfluidic chip using a low refractive index polymer," *Lab Chip*, vol. 16, no. 13, pp. 2481–2486, 2016. doi: 10.1039/c6lc00481d .

[245] W. Groh and A. Zimmermann, "What is the lowest refractive index of an organic polymer?" *Macromolecules*, vol. 24, no. 25, pp. 6660–6663, Dec. 1991. doi: 10.1021/ma00025a016 .

[246] M.-A. Aegerter, *Aerogels Handbook*, 1st ed., ser. SpringerLink, N. Leventis and M. M. Koebel, Eds. New York, NY: Springer New York, 2011.

[247] L. Canham, *Handbook of Porous Silicon*. Springer International Publishing, 2018. doi: 10.1007/978-3-319-71381-6 .

[248] C. Prokop, S. Schoenhardt, B. Laegel, S. Wolff, A. Mitchell, and C. Karnutsch, "Air-suspended SU-8 polymer waveguide grating couplers," *J. Lightwave Technol.*, vol. 34, no. 17, pp. 3966–3971, Sep. 2016. doi: 10.1109/jlt.2016.2593025 .

[249] J. M. Maia, V. A. Amorim, D. Viveiros, and P. V. S. Marques, "Femtosecond laser micromachining of an optofluidics-based monolithic whispering-gallery mode resonator coupled to a suspended waveguide," *Sci. Rep.*, vol. 11, no. 1, Apr. 2021. doi: 10.1038/s41598-021-88682-x .

[250] W. Zhou, Z. Cheng, X. Wu, X. Sun, and H. K. Tsang, "Fully suspended slot waveguide platform," *J. Appl. Phys.*, vol. 123, no. 6, Feb. 2018. doi: 10.1063/1.5017780 .

[251] H. Li, Y. Wang, Y. Sun, S. Zhang, Z. An, S. Zhang, C. Zhang, Z. Zhang, Q. Mao, and J. D. Prades García, "Design and fabrication of SU-8 polymer arrayed waveguide gratings based on flexible PDMS substrates," *Appl. Optics*, vol. 61, no. 9, p. 2213, Mar. 2022. doi: 10.1364/ao.447132 .

[252] K. Leosson and B. Agnarsson, "Integrated biophotonics with CYTOP," *Micromachines*, vol. 3, no. 1, pp. 114–125, Feb. 2012. doi: 10.3390/mi3010114 .

[253] P. Pirasteh, J. Charrier, Y. Dumeige, S. Haesaert, and P. Joubert, "Optical loss study of porous silicon and oxidized porous silicon planar waveguides," *J. Appl. Phys.*, vol. 101, no. 8, Apr. 2007. doi: 10.1063/1.2718886 .

[254] P. Girault, N. Lorrain, J. Lemaitre, L. Poffo, M. Guendouz, I. Hardy, M. Gadonna, A. Gutierrez, L. Bodiou, and J. Charrier, "Racetrack micro-resonators based on ridge waveguides made of porous silica," *Opt. Mater.*, vol. 50, pp. 167–174, Dec. 2015. doi: 10.1016/j.optmat.2015.10.017 .

[255] A. Jain, S. Rogojevic, S. Ponoth, N. Agarwal, I. Matthew, W. Gill, P. Persans, M. Tomozawa, J. Plawsky, and E. Simonyi, "Porous silica materials as low-k dielectrics for electronic and optical interconnects," *Thin Solid Films*, vol. 398–399, pp. 513–522, Nov. 2001. doi: 10.1016/s0040-6090(01)01311-6 .

[256] M. D. W. Grogan, S. G. Leon-Saval, R. England, and T. A. Birks, "Silica aerogel core waveguide," *Opt. Express*, vol. 18, no. 21, p. 22497, Oct. 2010. doi: 10.1364/oe.18.022497 .

[257] S. Santos, K. Paula, F. Couto, M. Facure, D. Correa, and C. Mendonca, "Femtosecond laser micromachining optical waveguides on transparent silica xerogels," *Opt. Mater.*, vol. 132, p. 112819, Oct. 2022. doi: 10.1016/j.optmat.2022.112819 .

[258] S. S. Ponoth, N. T. Agarwal, P. D. Persans, and J. L. Plawsky, "Plasma silicon oxide–silica xerogel based planar optical waveguides," *Journal of Vacuum Science & Technology B: Microelectronics and Nanometer Structures Processing, Measurement, and Phenomena*, vol. 22, no. 3, pp. 902–908, Apr. 2004. doi: 10.1116/1.1701847 .

[259] R. Yokokawa, J.-A. Paik, B. Dunn, N. Kitazawa, H. Kotera, and C.-J. Kim, "Mechanical properties of aerogel-like thin films used for MEMS," *J. Micromech. Microeng.*, vol. 14, no. 5, pp. 681–686, Mar. 2004. doi: 10.1088/0960-1317/14/5/004 .

[260] Y. M. Obeidat and K. L. Lear, "Mathematical modeling for losses in optical waveguides with porous silica cladding," *IEEE Sensors Journal*, vol. 21, no. 4, pp. 4747–4754, Feb. 2021. doi: 10.1109/jsen.2020.3035515 .

[261] O. Bliznyuk, H. P. Jansen, E. S. Kooij, H. J. W. Zandvliet, and B. Poelsema, "Smart design of stripe-patterned gradient surfaces to control droplet motion," *Langmuir*, vol. 27, no. 17, pp. 11 238–11 245, Sep. 2011. doi: 10.1021/la201671w .

[262] N. Moumen, R. S. Subramanian, and J. B. McLaughlin, "Experiments on the motion of drops on a horizontal solid surface due to a wettability gradient," *Langmuir*, vol. 22, no. 6, pp. 2682–2690, Mar. 2006. doi: 10.1021/la053060x .

[263] R. S. Subramanian, N. Moumen, and J. B. McLaughlin, "Motion of a drop on a solid surface due to a wettability gradient," *Langmuir*, vol. 21, no. 25, pp. 11 844–11 849, Dec. 2005. doi: 10.1021/la051943i .

[264] F. Brochard, "Motions of droplets on solid surfaces induced by chemical or thermal gradients," *Langmuir*, vol. 5, no. 2, pp. 432–438, Mar. 1989. doi: 10.1021/la00086a025 .

[265] K. Williams, K. Gupta, and M. Wasilik, "Etch rates for micromachining processing-part II," *J. Microelectromech. S.*, vol. 12, no. 6, pp. 761–778, Dec. 2003. doi: 10.1109/jmems.2003.820936 .

[266] F. D. Egitto, "Plasma etching and modification of organic polymers," *Pure Appl. Chem.*, vol. 62, no. 9, pp. 1699–1708, Jan. 1990. doi: 10.1351/pac199062091699 .

[267] J. Han, H. Xu, S. H. K. Paleti, A. Sharma, and D. Baran, "Understanding photochemical degradation mechanisms in photoactive layer materials for organic solar cells," *Chem. Soc. Rev.*, vol. 53, no. 14, pp. 7426–7454, 2024. doi: 10.1039/d4cs00132j .

[268] P. J. Rivero, J. Goicoechea, and F. J. Arregui, "Optical fiber sensors based on polymeric sensitive coatings," *Polymers*, vol. 10, no. 3, p. 280, Mar. 2018. doi: 10.3390/polym10030280 .

[269] D. P. Go, D. J. E. Harvie, N. Tirtaatmadja, S. L. Gras, and A. J. O'Connor, "A simple, scalable process for the production of porous polymer microspheres by inkjetting combined with thermally induced phase separation," *Part. Part. Syst. Char.*, vol. 31, no. 6, pp. 685–698, Jan. 2014. doi: 10.1002/ppsc.201300298 .

[270] S. Alsoy and J. L. Duda, "Influence of swelling and diffusion-induced convection on polymer sorption processes," *AIChE Journal*, vol. 48, no. 9, pp. 1849–1855, Sep. 2002. doi: 10.1002/aic.690480903 .

[271] O. Hölck, M. Böhning, M. Heuchel, M. R. Siegert, and D. Hofmann, "Gas sorption isotherms in swelling glassy polymers-detailed atomistic simulations," *J. Membrane Sci.*, vol. 428, pp. 523–532, Feb. 2013. doi: 10.1016/j.memsci.2012.10.023 .

[272] H. B. Park, J. Kamcev, L. M. Robeson, M. Elimelech, and B. D. Freeman, "Maximizing the right stuff: The trade-off between membrane permeability and selectivity," *Science*, vol. 356, no. 6343, p. eaab0530, Jun. 2017. doi: 10.1126/science.aab0530 .

[273] C. Loschen and A. Klamt, "Prediction of solubilities and partition coefficients in polymers using COSMO-RS," *Industrial & Engineering Chemistry Research*, vol. 53, no. 28, pp. 11 478–11 487, Jul. 2014. doi: 10.1021/ie501669z .

[274] H. Elbs and G. Krausch, "Ellipsometric determination of Flory-Huggins interaction parameters in solution," *Polymer*, vol. 45, no. 23, pp. 7935–7942, Oct. 2004. doi: 10.1016/j.polymer.2004.09.021 .

[275] W. Ogieglo, H. Wormeester, K.-J. Eichhorn, M. Wessling, and N. E. Benes, "In situ ellipsometry studies on swelling of thin polymer films: A review," *Prog. Polym. Sci.*, vol. 42, pp. 42–78, Mar. 2015. doi: 10.1016/j.progpolymsci.2014.09.004 .

[276] Innovation Canada, "Technology readiness levels," Jan. 2018. [Online]. Available: https://ised-isde.canada.ca/site/innovation-canada/en/technology-readiness-levels

[277] A. Leblanc-Hotte, G. Chabot-Roy, L. Odagiu, M. Richaud, S. Lesage, J.-S. Delisle, and Y.-A. Peter, "High-throughput refractive index-based microphotonic sensor for enhanced cellular discrimination," *Sens. Actuators, B*, vol. 266, pp. 255–262, Aug. 2018. doi: 10.1016/j.snb.2018.03.087 .

[278] H.-T. Kim and M. Yu, "High-speed optical sensor interrogator with a silicon-ring-resonator-based thermally tunable filter," *Opt. Lett.*, vol. 42, no. 7, p. 1305, Mar. 2017. doi: 10.1364/ol.42.001305 .

[279] J. Su, A. F. Goldberg, and B. M. Stoltz, "Label-free detection of single nanoparticles and biological molecules using microtoroid optical resonators," *Light Sci. Appl.*, vol. 5, no. 1, pp. e16 001–e16 001, Jan. 2016. doi: 10.1038/lsa.2016.1 .

[280] J. Liu, X. Zhou, Z. Qiao, J. Zhang, C. Zhang, T. Xiang, L. Shui, Y. Shi, and L. Liu, "Integrated optical chemical sensor based on an SOI ring resonator using phase-interrogation," *IEEE Photonics J.*, vol. 6, no. 5, pp. 1–7, Oct. 2014. doi: 10.1109/jphot.2014.2352973 .

APPENDIX A DIFFUSION OF A GAS IN A POLYMER SLAB FROM BOTH SIDES

The diffusion of a gas in a polymer slab from both sides is analogous to the linear flow of heat in a solid bounded by two parallel planes, as described in Chapter III of the book *Conduction of Heat in Solids* (1959) by H.S. Carslaw and J.C. Jaeger [196].

The diffusion problem for the concentration $C(y,t)$ is described by:

$$\begin{aligned} \frac{\partial C}{\partial t} &= D\frac{\partial^2 C}{\partial y^2} \ (0 < y < d) \\ C(0,t) &= \phi_1(t) \\ C(d,t) &= \phi_2(t) \\ C(y,0) &= f(y) \end{aligned}$$

with D is the diffusion coefficient, $\phi_1(t)$ and $\phi_2(t)$ are the concentrations at the slab interfaces, and $f(y)$ is the initial gas concentration distribution in the slab.

We put $C = U + W$. Then, we have: By decomposing C into U and W, we can solve the problem separately ($C = U + W$). U as the zero boundary conditions:

$$\begin{aligned} \frac{\partial U}{\partial t} &= D\frac{\partial^2 U}{\partial y^2} \ (0 < y < d) \\ U(0,t) &= 0 \\ U(d,t) &= 0 \\ U(y,0) &= f(y) \end{aligned}$$

and W as the null initial condition:

$$\begin{aligned} \frac{\partial W}{\partial t} &= D\frac{\partial^2 W}{\partial y^2} \ (0 < y < d) \\ W(0,t) &= \phi_1 \\ W(d,t) &= \phi_2 \\ W(y,0) &= 0 \end{aligned}$$

From section 3.3, U is solved with:

$$U = \frac{2}{d}\sum_{m=1}^{\infty} e^{-\frac{Dm^2\pi^2}{d^2}t}\sin\left(\frac{m\pi y}{d}\right)\int_0^d f(y')\sin\left(\frac{m\pi y'}{d}\right)dy'$$

We use the Duhamel's theorem (section 1.14) to solve for W:

$$\begin{aligned} W =&\phi_1(\lambda)\left[1-\frac{y}{d}-\frac{2}{\pi}\sum_{m=1}^{\infty}\frac{1}{m}e^{-\frac{Dm^2\pi^2}{d^2}(t-\lambda)}\sin\left(\frac{m\pi y}{d}\right)\right] \\ &+\phi_1(\lambda)\left[\frac{y}{d}+\frac{2}{\pi}\sum_{m=1}^{\infty}\frac{1}{m}\cos(m\pi)e^{-\frac{Dm^2\pi^2}{d^2}(t-\lambda)}\sin\left(\frac{m\pi y}{d}\right)\right] \end{aligned}$$

Hence, when the surface concentration are $\phi_1(t)$ and $\phi_2(t)$, we obtain

$$W = \int_0^t\left[\phi_1(\lambda)\frac{\partial}{\partial t}F_1(y,t-\lambda)+\phi_2(\lambda)\frac{\partial}{\partial t}F_2(y,t-\lambda)\right]d\lambda$$

where

$$\begin{aligned} F_1(y,t-\lambda) &= 1-\frac{y}{d}-\frac{2}{\pi}\sum_{m=1}^{\infty}\frac{1}{m}e^{-\frac{Dm^2\pi^2}{d^2}(t-\lambda)}\sin\left(\frac{m\pi y}{d}\right) \\ F_2(y,t-\lambda) &= \frac{y}{d}+\frac{2}{\pi}\sum_{m=1}^{\infty}\frac{1}{m}\cos(m\pi)e^{-\frac{Dm^2\pi^2}{d^2}(t-\lambda)}\sin\left(\frac{m\pi y}{d}\right) \end{aligned}$$

Thus,

$$W = \frac{2D\pi}{d^2}\sum_{m=1}^{\infty} m\ e^{-\frac{Dm^2\pi^2}{d^2}t}\sin\left(\frac{m\pi y}{d}\right)\int_0^t e^{\frac{Dm^2\pi^2}{d^2}\lambda}\left[\phi_1(\lambda)-(-1)^m\phi_2(\lambda)\right]d\lambda$$

Therefore,

$$C = \frac{2}{d}\sum_{m=1}^{\infty} e^{-\frac{Dm^2\pi^2}{d^2}t}\sin\left(\frac{m\pi y}{d}\right)\left[\int_0^d f(y')\sin\left(\frac{m\pi y'}{d}\right)dy'+\frac{mD\pi}{d}\int_0^t e^{\frac{Dm^2\pi^2}{d^2}\lambda}\left\{\phi_1(\lambda)-(-1)^m\phi_2(\lambda)\right\}d\lambda\right]$$

To simplify further, we choose $f(y') = C_0$ and $\phi(t) = \phi_1(t) = \phi_2(t)$:

$$C = \frac{2}{d}\sum_{m=1}^{\infty} e^{-\frac{Dm^2\pi^2}{d^2}t}\sin\left(\frac{m\pi y}{d}\right)\left[C_0\frac{d}{m\pi}\left(1-\cos(m\pi)\right)+\frac{mD\pi}{d}\int_0^t e^{\frac{Dm^2\pi^2}{d^2}\lambda}\phi(\lambda)\left\{1-(-1)^m\right\}d\lambda\right]$$

We change from $m \to (2m+1)$:

$$C = \frac{4}{d}\sum_{m=0}^{\infty} e^{-\frac{D(2m+1)^2\pi^2}{d^2}t}\sin\left(\frac{(2m+1)\pi y}{d}\right)\left[C_0\frac{d}{(2m+1)\pi} + \frac{(2m+1)D\pi}{d}\int_0^t e^{\frac{D(2m+1)^2\pi^2}{d^2}\lambda}\phi(\lambda)d\lambda\right]$$

The mean of C is:

$$\begin{aligned}
\overline{C} &= \frac{1}{d}\int_0^d X dy \\
&= \frac{1}{d}\int_0^d \frac{4}{d}\left\{\sum_{m=0}^{\infty} e^{-\frac{D(2m+1)^2\pi^2}{d^2}t}\sin\left(\frac{(2m+1)\pi y}{d}\right)\left[C_0\frac{d}{(2m+1)\pi} + \frac{(2m+1)D\pi}{d}\int_0^t e^{\frac{D(2m+1)^2\pi^2}{d^2}\lambda}\phi(\lambda)d\lambda\right]\right\} dy \\
&= \frac{4}{d^2}\sum_{m=0}^{\infty} e^{-\frac{D(2m+1)^2\pi^2}{d^2}t}\int_0^d \sin\left(\frac{(2m+1)\pi y}{d}\right)dy\left[C_0\frac{d}{(2m+1)\pi} + \frac{(2m+1)D\pi}{d}\int_0^t e^{\frac{D(2m+1)^2\pi^2}{d^2}\lambda}\phi(\lambda)d\lambda\right] \\
&= \frac{4}{d^2}\sum_{m=0}^{\infty} e^{-\frac{D(2m+1)^2\pi^2}{d^2}t} d\frac{1-\cos\left((2m+1)\pi\right)}{(2m+1)\pi}\left[C_0\frac{d}{(2m+1)\pi} + \frac{(2m+1)D\pi}{d}\int_0^t e^{\frac{D(2m+1)^2\pi^2}{d^2}\lambda}\phi(\lambda)d\lambda\right] \\
&= \frac{8}{d\pi}\sum_{m=0}^{\infty} e^{-\frac{D(2m+1)^2\pi^2}{d^2}t}\frac{1}{(2m+1)}\left[C_0\frac{d}{(2m+1)\pi} + \frac{(2m+1)D\pi}{d}\int_0^t e^{\frac{D(2m+1)^2\pi^2}{d^2}\lambda}\phi(\lambda)d\lambda\right] \\
&= 8\left[\frac{C_0}{\pi^2}\sum_{m=0}^{\infty}\frac{e^{-\frac{D(2m+1)^2\pi^2}{d^2}t}}{(2m+1)^2} + \frac{D}{d^2}\sum_{m=0}^{\infty} e^{-\frac{D(2m+1)^2\pi^2}{d^2}t}\int_0^t e^{\frac{D(2m+1)^2\pi^2}{d^2}\lambda}\phi(\lambda)d\lambda\right]
\end{aligned}$$

With $C_0 = 0$, it becomes:

$$\overline{C} = \frac{8D}{d^2}\sum_{m=0}^{\infty} e^{-\frac{D(2m+1)^2\pi^2}{d^2}t}\int_0^t e^{\frac{D(2m+1)^2\pi^2}{d^2}\lambda}\phi(\lambda)d\lambda$$

We can rewrite it:

$$\begin{aligned}
\overline{C} &= \frac{8D}{d^2}\sum_{m=0}^{\infty}\int_0^t e^{-\frac{D(2m+1)^2\pi^2}{d^2}(t-\lambda)}\phi(\lambda)d\lambda \\
&= \frac{8D}{d^2}\sum_{m=0}^{\infty}\int_0^t g_m(t-\lambda)\phi(\lambda)d\lambda \\
&= \frac{8D}{d^2}\sum_{m=0}^{\infty}\left(g_m * \phi\right)(t) \\
g_m(t) &= e^{-\frac{D(2m+1)^2\pi^2}{d^2}t}
\end{aligned}$$

With Laplace transform:

$$\begin{aligned}\mathcal{L}\left\{\left(g_m * \phi\right)(t)\right\} &= G_m(s)\Phi(s)\\ G_m(s) &= \mathcal{L}\left\{g_m(t)\right\}\\ \Phi(s) &= \mathcal{L}\left\{\phi(t)\right\}\end{aligned}$$

Therefore, we have

$$\mathcal{L}\left\{\overline{C}\right\} = \frac{8D}{d^2}\sum_{m=0}^{\infty} G_m(s)\Phi(s) \tag{A.1}$$

$$= \Phi(s)\frac{8D}{d^2}\sum_{m=0}^{\infty} G_m(s) \tag{A.2}$$

$$\Phi(s) = \frac{d^2}{8D}\mathcal{L}\left\{\overline{X}\right\}\left(\sum_{m=0}^{\infty} G_m(s)\right)^{-1} \tag{A.3}$$

$$\phi(t) = \mathcal{L}^{-1}\left\{\frac{d^2}{8D}\mathcal{L}\left\{\overline{X}\right\}\left(\sum_{m=0}^{\infty} G_m(s)\right)^{-1}\right\} \tag{A.4}$$

So we have to compute $\sum_{m=0}^{\infty} G_m(s)$.

$$\begin{aligned}G_m(s) &= \mathcal{L}\left\{e^{-\frac{D(2m+1)^2\pi^2}{d^2}(t)}\right\}\\ &= \int_0^{\infty} e^{-\frac{D(2m+1)^2\pi^2}{d^2}t}e^{-st}dt\\ &= \frac{1}{\frac{D(2m+1)^2\pi^2}{d^2}+s} \text{ for } \Re\left(\frac{D(2m+1)^2\pi^2}{d^2}+s\right) > 0\\ &= \frac{d^2}{D(2m+1)^2\pi^2 + d^2 s}\end{aligned}$$

It cannot be solved analytically. But if we know the diffusion coefficient and the thickness of the slab, it is possible to compute it numerically. Then, it is possible to get the instantaneous concentration $Y(s) = \mathcal{L}\left\{\phi(t)\right\}$ with the response of $X(s) = \mathcal{L}\left\{\overline{C}\right\}$. We only have to apply the transfer function $H(s)$ define by:

$$H(s) = \frac{Y(s)}{X(s)} = \frac{d^2}{8D}\left(\sum_{m=0}^{\infty} G_m(s)\right)^{-1}$$

APPENDIX B NUMERICAL COMPARISON OF THE EFFECTIVE REFRACTIVE INDEX AND TRANSMISSION PEAK HEIGHT OF WAVEGUIDES WITH DIFFERENT MATERIALS, CONFIGURATIONS AND DIMENSIONS.

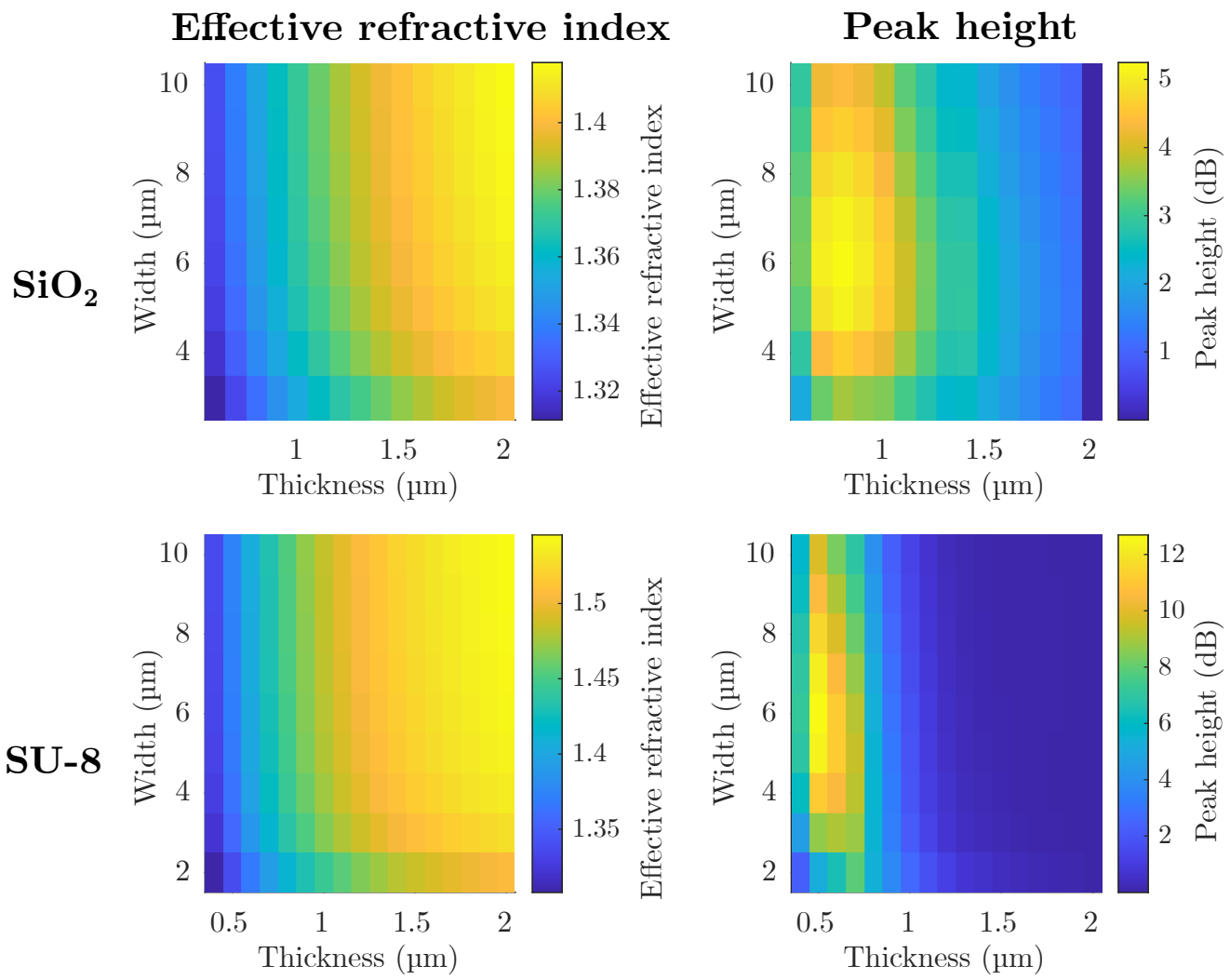

Figure B.1 Numerical calculation results of the effective refractive indices of rib waveguides as a function of their widths and thicknesses for different core materials (SiO_2 and SU-8) and the maximum peak heights of the transmission spectra of these waveguides coupled to a SU-8 microdrop resonator.

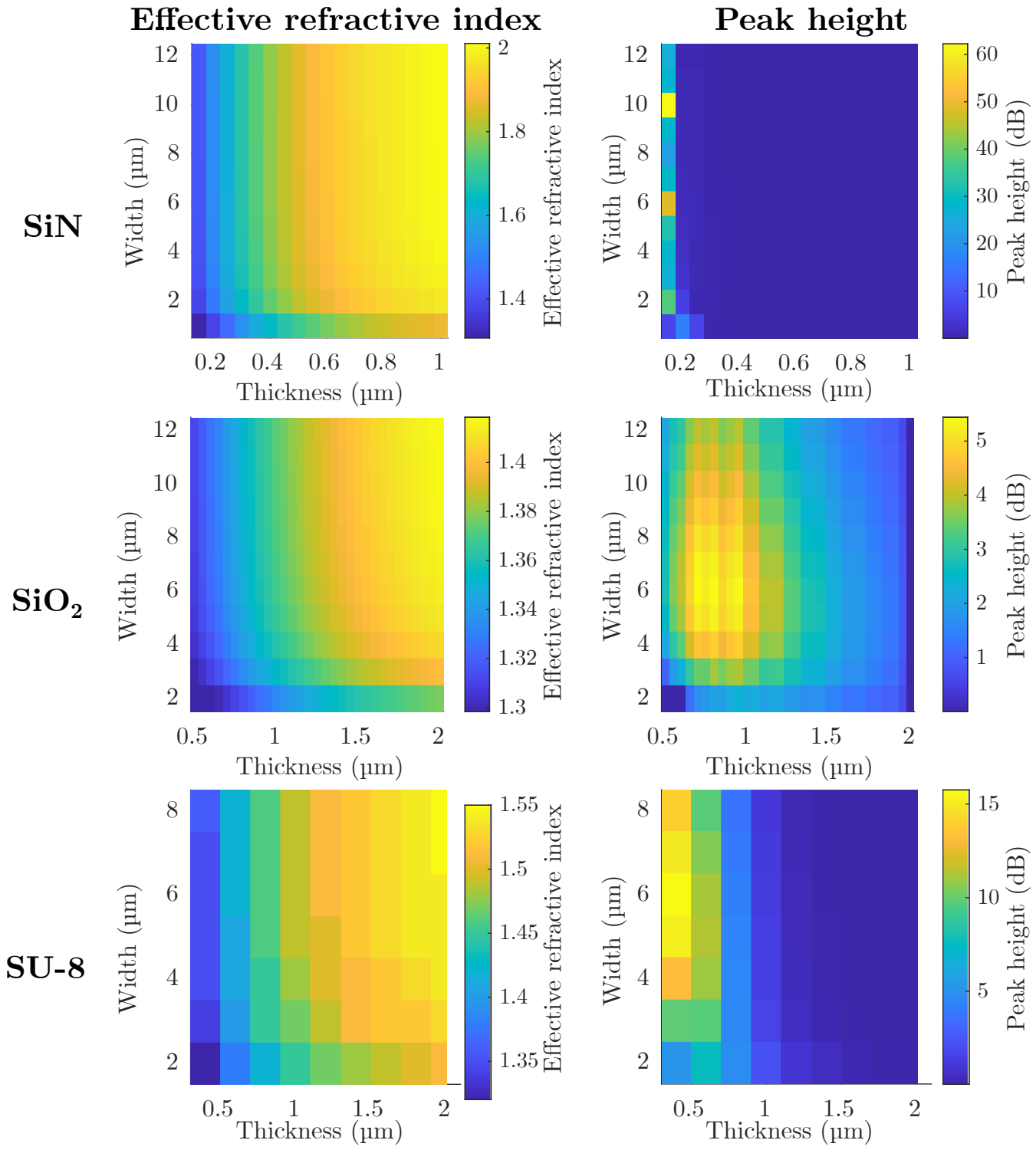

Figure B.2 Numerical calculation results of the effective refractive indices of ridge waveguides as a function of their widths and thicknesses for different core materials (SiN, SiO_2 and SU-8) and the maximum peak heights of the transmission spectra of these waveguides coupled to a SU-8 microdrop resonator.